

## ABSTRACT

Title of Thesis: A PLATFORM TOWARDS *IN SITU* STRESS/STRAIN  
MEASUREMENT IN LITHIUM ION BATTERY  
ELECTRODES.

Degree Candidate: Sergio D. Baron

Degree and Year: Masters of Science, 2012

Thesis Directed By: Dr. Reza Ghodssi, Electrical and Computer Engineering.

This thesis demonstrates the design, fabrication and testing of a platform for *in situ* stress/strain measurement in lithium ion battery electrodes. The platform – consisting of a Microelectromechanical System (MEMS) chip containing an electrochemical cavity and an optical sensing element, a custom electrochemical package and an experimental setup – was successfully developed. Silicon was used as an active electrode material, and a thin-film electrochemical stack was conceived and tested. Finally, multiple experiments showed correlation between the active material volume change inside the battery and a signal change in the optical sensing element. The experimental results, combined with the MEMS implementation of the sensing element provide a promising way to evaluate electrochemical reaction-induced stress monitoring in a simple and compact fashion, while experiments are carried out *in situ*.

A PLATFORM TOWARDS *IN SITU* STRESS/STRAIN  
MEASUREMENT IN LITHIUM ION BATTERY ELECTRODES.

By

Sergio D. Baron

Thesis submitted to the Faculty of the Graduate School of the University of  
Maryland, College Park, in partial fulfillment of the requirements for the  
degree of Master of Science

2012

Advisory Committee:

Professor Reza Ghodssi, Chair

Professor Martin Peckerar

Professor Chunsheng Wang

© Copyright by

Sergio D. Baron

2012



Dedication:

To my Mother.

## **Acknowledgements**

I would like to thank the thesis committee: Professor Reza Ghodssi, Professor Martin Peckerar and Professor Chunsheng Wang.

Tom Loughram, John Abrahams and Jonathan Hummel, for their help with fabrication, and the many hours of informative and indispensable discussions, assistance, and equipment access during the fabrication of the work presented here.

This work would have been impossible without the funding from: the U.S. Department of Estate Fulbright Commission, the Argentina Ministry of Education, the La Plata National University and the U.S. Department of Energy through the Energy Frontiers Research Center program.

## Table of contents

Acknowledgements .....	ii
Table of contents .....	iv
List of tables .....	vi
List of figures.....	vi
1.- Background and Motivation.....	1
1.1.- Introduction.....	1
1.2.- MEMS technologies.....	2
1.2.1.- Optical MEMS .....	3
1.3.- Optical Interferometry, the Fabry-Perot interferometer.....	7
1.4.- Lithium-ion batteries.....	12
1.4.1.- Introduction to the elements of a lithium-ion battery.....	12
1.4.2.- Factors limiting the lifecycle of a lithium-ion battery.....	13
1.4.3.- Silicon as a high capacity anode material.....	14
1.5.- Previous work on measurement of electrochemical reaction-induced stress measurement in electrode materials of lithium ion batteries.....	15
1.6.- Platform overview.....	19
2.- Design of the monitoring platform.....	20
2.1.- Design requirements and considerations.....	22
2.2.- The MEMS sensing chip.....	23
2.2.1.- Overview of the architecture and materials used.....	23
2.2.2.- Device dimensions.....	24
2.3.- The electrochemical package.....	26
2.3.1.- Technical and practical design considerations.....	26
2.3.2.- Design of the first generation package.....	27
2.3.3.- Design of the second generation package.....	29
2.3.4.- Design of the third generation package.....	31
2.4.- The testing setup.....	36
2.4.1.- Overview and design.....	36
2.4.2.- Inverted microscope and camera.....	37
2.4.3.- Laser light source.....	38
2.4.4.- Battery testing station.....	39
3.- MEMS Fabry-Perot chip Fabrication.....	40
3.1.- MEMS chip mask design.....	40
3.2.- Fabrication process flow.....	41
3.3.- Fabrication details.....	45
3.5.- Thin-film materials electrochemical stack.....	48
3.5.1.- Materials stack deposition using titanium nitride as a current collector.....	48
3.5.2.- Stack deposition using Cu as a current collector.....	49
3.5.3.- Electrochemical cavity underetching and thin-film conformal covering.....	51
4.- Experimental testing.....	52

4.1.- Pneumatic Testing and characterization of the MEMS Fabry-Perot chip.....	52
4.1.1.- Test setup and methodology.....	52
4.1.2.- Physical principles applied.....	53
4.1.3.- Pneumatic test results.....	54
4.2.- Electrochemical testing of the thin-film electrochemical stacks using dummy devices.....	55
4.2.1.- Silicon thin-film on stainless steel discs.....	55
4.2.2.- TiN-Si Stack in a standard coin cell.....	57
4.2.3.- TiN-Si Stack in first and second generation custom electrochemical package.....	58
4.2.4.- Ti-Cu-Ti-Si Stack in custom coin cell / third generation package.....	60
4.3.- <i>In situ</i> testing of electrochemically reaction-induced volume change in silicon.....	63
4.3.1.- Test using first and second generation package and TiN-Si thin film stack.....	63
4.3.1.1.- Experimental setup and parameters.....	63
4.3.2.- Test using custom coin cell / third generation package and Ti-Cu-Ti-Si thin film stack.....	64
4.3.2.1.- Experimental setup and parameters.....	64
4.3.2.2.- First experiment.....	66
4.3.2.3.- Second experiment.....	69
4.3.2.4.- Third experiment.....	71
5.- Data analysis and discussion.....	73
5.1.- Analysis of the electrochemical data.....	73
5.2.- Secondary effects considerations.....	75
5.3.- Analysis of correlated Fabry-Perot fringe changes and electrochemical data.....	76
5.3.1.- Computer analysis of Fabry-Perot fringe data.....	76
5.3.2.- Correspondence of electrochemical data.....	78
5.3.3.-Mechanical stress relaxation during discharge.....	79
5.3.4.-Mechanical stress accumulation from cycle to cycle.....	81
5.4.- Discussion.....	82
6.- Conclusions and future work.....	85
6.1.- Summary of results reported.....	85
6.2.- Future work.....	86
6.2.1.- Enhancement of the finesse of the Fabry-Perot interferometer.....	86
6.2.2.- Testing of different active materials, anodes and cathodes.....	87
6.2.3.- Designing a microscope-less testing setup.....	87
6.2.4.- Measurement of volume change / stress on active materials in Li-ion batteries.....	88
6.3.- Conclusion.....	88
Appendix A: Photolithography masks.....	90
Appendix B: Fabrication process details.....	91
Appendix C: Experiment videos.....	91
Appendix D: FP fringe images.....	92
Appendix E: Image analysis MatLab code.....	100
Bibliography.....	104



## List of tables

Table 2.1: Device dimensions.....	25
Table 2.2: Thickness of components inside the coin cell.....	34
Table 3.1: Detailed process flow.....	45

## List of figures

Figure 1.1: Steerable micromirror array in comparison to needle.....	4
Figure 1.2: Shutter optical switch.....	4
Figure 1.3: Microcantilever-based biosensor.....	5
Figure 1.4: schematic of MEMS membrane and microresonator sensor.....	6
Figure 1.5: Images of laser light reflected from a single sensor at several pressures.....	7
Figure 1.6: Schematic representation of Fabry-Perot interferometer operation.....	8
Figure 1.7: Finesse and the resolution of Fabry-Perot fringes.....	10
Figure 1.8: Commercial Fabry-Perot interferometer.....	11
Figure 1.9: Fabry-Perot fringe pattern.....	11
Figure 1.10: Schematic representation of the discharge and charge process in a Li-ion battery.....	13
Figure 1.11: Li-ion battery silicon electrode.....	14
Figure 1.12: Ex situ XRD patterns of crystalline silicon electrodes.....	16
Figure 1.13: SEM image of silicon microparticles after different numbers of cycles.....	17
Figure 1.14: Acoustic activity versus voltage during cycling.....	17
Figure 1.15: Schematic illustration of the electrochemical cell along with the setup to measure substrate curvature.....	18
Figure 1.16: Representative current density, potential, and stress transients obtained from the stress-potential experiment in a lithiated-silicon electrode.....	19
Figure 2.1: Schematic representation of the sensing principle of the MEMS chip platform.....	21
Figure 2.2: Schematic of the Fabry-Perot monitoring platform operation.....	22
Figure 2.3: Schematic representation of the suggested MEMS chip monitoring platform.....	23
Figure 2.4: MEMS chip device layout.....	24
Figure 2.5: Schematic of device dimensions.....	25
Figure 2.6: Commercial Li-ion battery packages.....	27
Figure 2.7: Argon-filled glove box for Li-ion battery assembly.....	27
Figure 2.8: Schematic of first generation experimental package.....	28
Figure 2.9: First generation package parts.....	28
Figure 2.10: Second-generation package schematic.....	30
Figure 2.11: Second-generation package with chip-holding part fabricated on polycarbonate.....	30
Figure 2.12: Thin film coating schematic and picture.....	33
Figure 2.13: Third generation package based on a modified coin cell: assembly.....	34
Figure 2.14: Pierced coin cell can . Assembled and taped cell.....	35

Figure 2.15: Simplified schematic of measurement setup.....	36
Figure 2.16: Schematic of the measurement platform setup. ....	37
Figure 2.17: Complete experimental setup.....	38
Figure 2.18: De-speckled laser light source. ....	39
Figure 2.19: Arbin Instruments Battery testing system.....	40
Figure 3.1: First mask (first DRIE). ....	41
Figure 3.2: Schematic of MEMS chip process flow.....	42
Figure 3.3: SEM image of the Fabry-Perot cavity sidewall. ....	46
Figure 3.4: SEM image of the silicon nitride membrane. ....	47
Figure 3.5: Cross-section SEM image of the MEMS chip.....	47
Figure 3.6: MEMS chip with titanium nitride and silicon layers deposited.....	49
Figure 3.7: Ti-Cu-Ti-Si on bulk Silicon electrochemical stack. ....	50
Figure 3.8: Schematic of materials thin-film stack. ....	51
Figure 3.9: SEM images of different DRIE etchings.. ....	51
Figure 4.1: Pneumatic test setup.....	53
Figure 4.2: Fabry-Perot fringe change at three different pressures. ....	54
Figure 4.3: Electrochemical performance of 200nm silicon thin-film on stainless steel disc .....	56
Figure 4.4 : Electrochemical performance of 1 $\mu$ m silicon thin-film silicon chip with a titanium nitride current collector on a coin cell.....	57
Figure 4.5: Electrochemical performance of 1 $\mu$ m silicon thin-film on a silicon chip with a titanium nitride current collector on custom first generation package .....	59
Figure 4.6: Electrochemical performance of 1 $\mu$ m silicon thin-film silicon chip with a Ti- Cu-Ti current collector on custom-modified coin cell. ....	61
Figure 4.7: Ti-Cu-Ti-Si thin-film stack tested on custom modified coin cell. ....	61
Figure 4.8: Optical microscope images of Ti-Cu-Ti-Si thin-film stack. ....	62
Figure 4.9: Experimental setup using first generation package. TiN-Si MEMS chip is inside the package. ....	64
Figure 4.10: complete experimental setup with third generation package and battery holder. .....	65
Figure 4.11: Fringe expansion in Fabry-Perot device. ....	66
Figure 4.12: First discharge/charge cycle of the first experiment battery made using a 200 $\mu$ m diameter membrane MEMS chip. ....	68
Figure 4.13: Third discharge/charge cycle of the second battery made using a 150 $\mu$ m diameter membrane MEMS chip.....	70
Figure 4.14: Fourteenth discharge/charge cycle of the third battery made using a 150 $\mu$ m diameter membrane MEMS chip.....	72
Figure 4.15: Fabry-Perot fringe photograph of third battery made using a 150 $\mu$ m diameter membrane MEMS chip.....	73
Figure 5.1: SEI formation zone during first discharge cycle, plateau at around 0.2V .....	74
Figure 5.2: Cartesian to polar transform of Fabry-Perot fringe images.. ....	77
Figure 5.3: Intensity trace plot of 4 Fabry-Perot fringe images. ....	77
Figure 5.4: Electrochemical data of: MEMS chip on custom package .....	79
Figure 5.5: Discharge/charge curve, mechanical stress curve on silicon thin-film.....	80
Figure 5.6: Fabry-Perot fringe images from the discharge cycle of the first experiment. ...	81



# **1.- Background and Motivation.**

## **1.1.- Introduction.**

The use of stored electrical energy has become increasingly important during the past years. From portable consumer electronics and cellphones to implanted medical devices and networks of sensors, they all use some kind of battery to store energy. Lithium-ion (Li-ion) technology became the most popular battery technology due to its high energy density compared to other technologies [1]. The materials used for cathode and anode determine the energy density of the battery. The research community worldwide is actively seeking new materials [2, 3] with ever higher energy densities in order to improve these figures of merit.

The discharge-charge process in a Li-ion battery involves the intercalation and extraction of lithium ions in the structure of the active anode and cathode materials [2]; this process induces volume expansion and contraction of such materials [4]. As the active anode and cathode materials swell and shrink, they may become delaminated from the underlying current collection material [5, 6] (normally copper or aluminum). When this happens, the capacity of the battery is diminished with each discharge-charge cycle [7], and eventually results in battery failure.

The objective of this work is to provide a monitoring platform that can observe, in real-time and in a de-coupled fashion, this mechanical expansion and contraction that limits the battery cycle life using Microelectromechanical Systems (MEMS) technologies [8]. The *in situ* and real-time capabilities of this platform allows to perform this monitoring in an

environment very close to the one of a real battery and can help battery scientists develop better materials for higher capacity and longer lasting Li-ion batteries.

## **1.2.- MEMS technologies.**

The use of MEMS for sensing and actuation applications in scientific and industrial environments is widespread and in constant development [9]. MEMS [8, 10] is a group of technologies that use microfabrication techniques and materials to build systems in which mechanical parts are the active component. Having the possibility of mechanical movement as result of electrical, thermal, chemical and other forces controlled by an external signal, MEMS are mostly used as sensors and actuators [11]. The miniaturization and batch fabrication capabilities, along with very precise structures that can be fabricated [8], make MEMS a very attractive technology to develop new projects.

Most MEMS are fabricated using what is known as top-down processes. A typical top-down process starts with a silicon wafer where structures are defined by photolithographic means and then etched using wet chemicals (such as hydrofluoric acid, potassium hydroxide, etc.) or dry etched using reactive ion etching (RIE), deep reactive ion etching (DRIE) and other techniques [10]. Materials may then be deposited by chemical vapor deposition (CVD), sputtering, or thermal evaporation, and etched subsequently in new patterns. Depending on the complexity of the MEMS device being fabricated, several of these process steps may be repeated as needed.

Conversely, bottom-up fabrication involves adding the structural parts of the device from the bottom up; this involves molecular-level control of the fabrication process, that can be chemically or physically driven. Being molecular self assembly one of the most used

bottom-up techniques [12], there are also other chemical self-assembly technologies [13] and assisted ones (atomic layer deposition [14], being one) that are part of the palette available for bottom-up fabrication.

As mentioned previously, MEMS devices can sense and actuate a diverse palette of signals, receiving a classification according to the characteristics of these signals. In the case of this work, the transducing mechanism is optical, hence classified as optical MEMS.

### **1.2.1.- Optical MEMS**

One of the revolutionary aspects of MEMS is its ability to miniaturize optical systems and devices in a way that were impossible before MEMS microfabrication techniques were developed [15-17]. Setups with dimensions of tens to hundreds of centimeters in size are reduced to tens of microns [18] and below. At these dimensions devices and waveguides [19] are on the size of optical wavelengths, capable of guiding light either in plane or out of plane; allowing the use of miniaturized optical systems in novel applications.

Optical actuators arranged to create an array of electrically steerable micro mirrors are used in Lucent's lambda router [20] (figure 1.1) that can route optical signals in a free path, shutter-type optical switch (figure 1.2), and popular designs like Texas Instruments DMD MEMS chips [21] are used in digital video projectors [22].

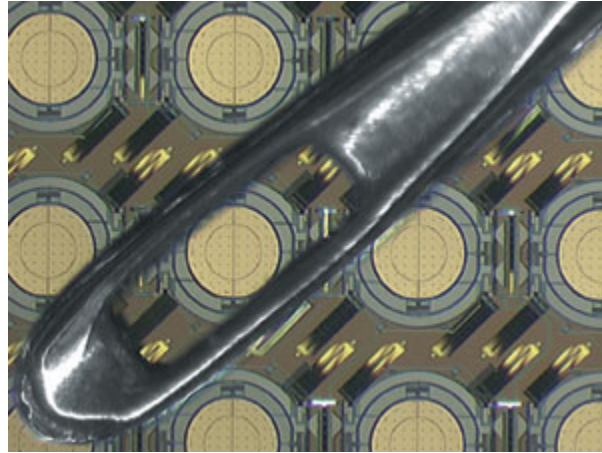


Figure 1.1: Steerable micromirror array in comparison to needle. [20]

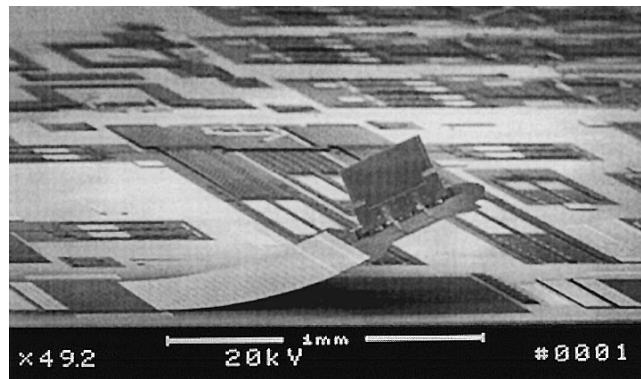


Figure 1.2: Shutter optical switch [23]

Optical sensors are transducers that can detect a chemical, mechanical or electrical phenomenon and produce an optical signal corresponding to it. For example, the change in resonance frequency of functionalized single anchored microstructured beams, known as micro cantilevers, [24] can be optically detected using laser light illumination and a photodiode to measure the binding of a biological molecule to it (figure 1.3)[25].

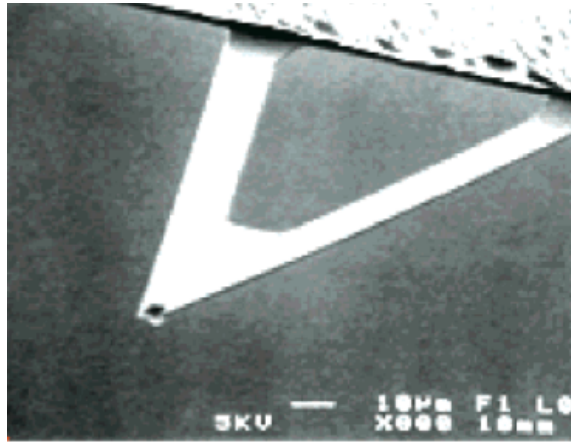


Figure 1.3: Microcantilever-based biosensor [25].

Suspended membranes are also used as sensors, where a parameter like gas pressure [26] can be determined by an optical readout.

The work of Pattnaik et al [27] uses a 1mm radius, 55µm thick silicon membrane to measure gas pressure. The transducing mechanism is based on an oxinitride optical ring resonator that lies on the edge of the membrane and as the membrane deflects, the stress induced on the ring resonator changes its refractive index. This change in the refractive index is read through external means as a frequency shift in the resonance, using a waveguide that couples optical energy in and out of the chip. The dimensions of the waveguides and resonator determine an operation using a light source of 1.55µm in wavelength, making it possible to be integrated monolithically into the chip. Figure 1.4 shows a schematic of the design.



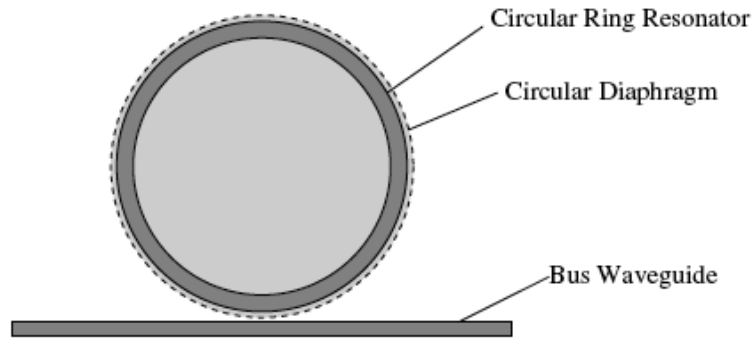


Figure 1.4: schematic of MEMS membrane and microresonator sensor. [27]

The authors report a MEMS pressure sensor that is able to measure pressures of up to 300KPa, but it needs a physical optical connection to function.

It is of particular interest for this thesis the work done by M.A. Schmidt et al [28] where an array of pressure sensors to do real-time measuring of fluid dynamics in a surface is made using micro machined silicon. The pressure sensors are based on a 1000 $\mu\text{m}$  by 1000 $\mu\text{m}$  square membrane of 55 $\mu\text{m}$  of thickness; these membranes deflect with the pressure change and modify its distance to an anchored parallel reflecting surface forming a Fabry-Perot interferometer (Fabry-Perot interferometry is covered in the next section). The array is illuminated using infrared laser light, to which the interferometers have been tuned, and a camera captures the readout. Figure 1.5 shows one of the sensors when applied with different pressures and how the Fabry-Perot interferometer provides an optical output in response.

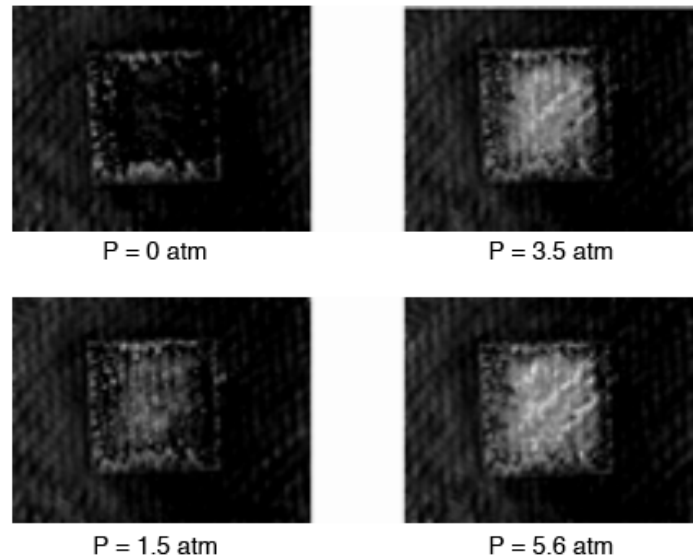


Figure 1.5: Images of laser light reflected from a single sensor at several pressures.

This work successfully demonstrates the implementation of a de-coupled readout of a mechanical parameter using microfabricated MEMS sensors based on a Fabry-Perot interferometer. This design does not need a physical connection to the transducing element, which is the case used in this work.

### **1.3.- Optical Interferometry, the Fabry-Perot interferometer.**

Optical interferometry is a powerful tool for spatial measurements. Based on the interference produced by illuminating and reflected light waves, optical interferometers produce patterns and intensity changes that can be interpreted to obtain the desired measured quantity. For instance white light interferometry [29] allows a user to obtain three-dimensional topographical maps of samples without the need of a physical contact [30].

The Fabry-Perot interferometer is an optical instrument, which is named after Charles Fabry and Alfred Perot, two French physicists that invented this instrument at the beginning of the 20<sup>th</sup> century. It is capable of measuring distances with great precision when the wavelength of the light used is known, or it can be used to measure the wavelength of light when precise mechanical parameters are known.

The Fabry-Perot interferometer consists of two semi-reflective parallel plates (*etalon* in French) in which the light bounces back and forth several times as shown in figure 1.6. It is desired that incident light have a uniform intensity and phase, so a diffused light source is normally used. Always taking into account that the minute phase changes that might be introduced by the diffuser are smaller than the change in the interference pattern that is to be measured.

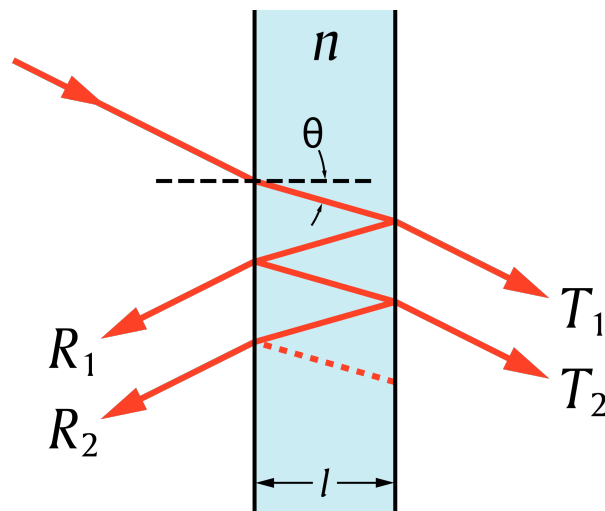


Figure 1.6: Schematic representation of Fabry-Perot interferometer operation [31].

The transmitted light  $T$  is a function of the wavelength of the light, and exhibits peaks of transmission that are a function of the resonances of the *etalon*. These peaks result in an interference pattern like the one seen in figure 1.9.

As seen in figure 1.6, the Fabry-Perot interferometer working principle is based on the multiple internal reflections inside two semi-reflecting surfaces. The governing equation for each constructive interference fringe  $T$  is given by the following equations [31]. The phase difference between each succeeding reflection is given by  $\delta$ ,

$$\delta = \left(\frac{2\pi}{\lambda}\right) 2n\ell \cos \theta. \quad (1.1) [31]$$

and,

$$T_e = \frac{(1 - R)^2}{1 + R^2 - 2R \cos \delta} = \frac{1}{1 + F \sin^2(\delta/2)}, \quad (1.2) [31]$$

where  $R$  is reflectance and  $F$  is finesse, which is given by:

$$F = \frac{4R}{(1 - R)^2} \quad (1.3) [31]$$

Finesse translates into more defined fringes; the higher is  $F$  the better the resolution of the interferometer. The finesse  $F$  depends proportionally on reflectance  $R$ , giving the most important parameter to consider when designing a Fabry-Perot interferometer: the better the reflectance of the surfaces, the better the resolution. Figure 1.7 shows how as reflectivity increases the peaks get narrower.

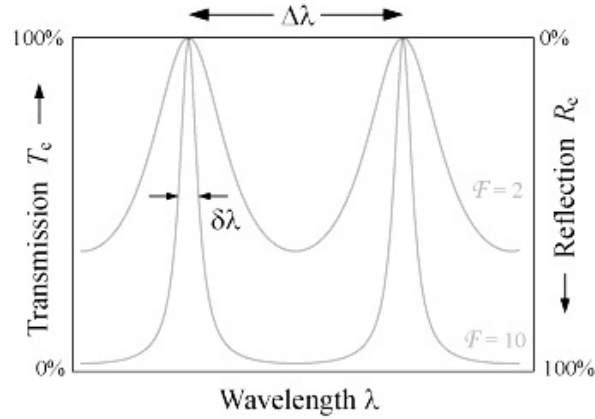


Figure 1.7: Finesse and the resolution of Fabry-Perot fringes [31].

When there is an optical path difference  $2nl \cos \theta$  a maximum in transmission occurs. This happens periodically in an integer multiple of wavelength  $\lambda$ . This same effect can be interpreted from the spectral point of view, saying that the wavelength ( $\lambda$ ) separation between two transmission maxima is defined by:

$$\Delta\lambda = \frac{\lambda_0^2}{2nl \cos \theta + \lambda_0} \approx \frac{\lambda_0^2}{2nl \cos \theta} \quad (1.4) [31]$$

This is called free spectral range (FSR), where  $\lambda_0$  is the central wavelength.

When we consider a  $90^\circ$  incidence of light, the formula for the location of Fabry-Perot maxima is  $2l = (m \cdot \lambda) / n$  (1.5) where  $l$  is the distance between surfaces,  $m$  is the fringe order,  $\lambda$  is the wavelength of light, and  $n$  is the refractive index. For a fixed  $l$  counting the number of fringes ( $m$ ) will produce the distance  $d$ . Since the wavelength  $\lambda$  is on the scale of nanometers, this enables the instrument to resolve distances with  $\lambda/2$  precision.

A physical implementation of this instrument can be built at the macro-scale, as is the case of commercial Fabry-Perot interferometers (figure 1.8). Figure 1.9 show a typical interference pattern.



Figure 1.8: Commercial Fabry-Perot interferometer.

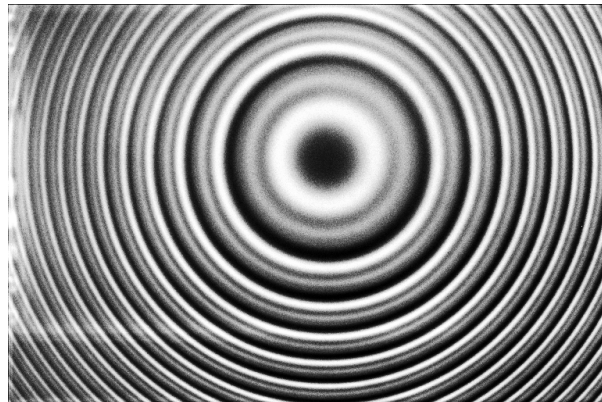


Figure 1.9: Fabry-Perot fringe pattern [31].

For this work a micro-scale Fabry-Perot interferometer with 90°-incidence monochromatic illumination was used. This simple but effective method is governed by what is stated in equation 1.5.

## **1.4.- Lithium-ion batteries.**

### **1.4.1.- Introduction to the elements of a lithium-ion battery.**

The main components are: anode, where current flows into the battery; cathode, in charge of extracting current out of the battery; electrolyte, is a medium that conducts the ions involved on the electrochemical process; and conductive materials are attached to the anode and cathode to collect the electron current. To avoid a short circuit between anode and cathode, a porous electrical insulation material known as separator is placed in the middle. The separator is an electrical insulator soaked with electrolyte that lets the lithium ions pass through [6].

During the discharge-charge process in a lithium-ion battery [32] (see figure 1.10), there is a movement of lithium ions inside the battery electrodes and through the electrolyte (diffusive process) [33] and an electrical current through the current collectors and the load that is connected to the battery.

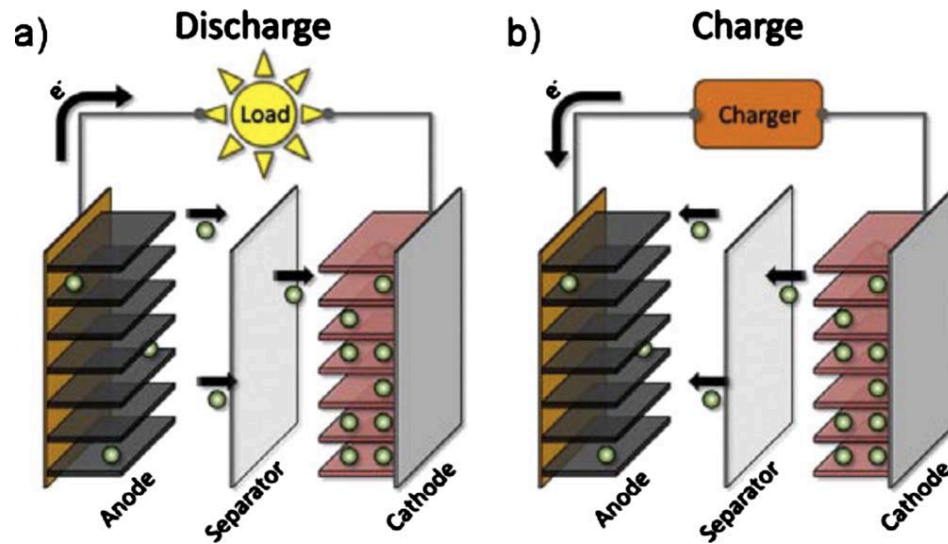


Figure 1.10: Schematic representation of the discharge and charge process in a Li-ion battery [4].

#### 1.4.2.- Factors limiting the lifecycle of a lithium-ion battery.

During the lifetime of the battery, the capacity diminishes until it does not hold enough energy for the purpose of its use. Very good Li-ion batteries have a discharge-charge life of about 1000 cycles. The higher the discharge/charge current the shorter the life of the battery.

One of the main mechanisms underlying this capacity loss process is the mechanical expansion and contraction of active battery materials that happens on anode and cathode materials while discharging and charging, respectively [34]. During the discharge phase, lithium ions are inserted into the crystalline matrix of the cathode and the charge process extracts those ions from the cathode material. On the anode the process is reversed. This intercalation and de-intercalation is associated with a mechanical expansion and contraction on the active materials that is not fully accommodated by the metallic current collection



materials underneath them. This mismatched mechanical stress produces delamination of the anode and cathode active materials from the current collectors [7].

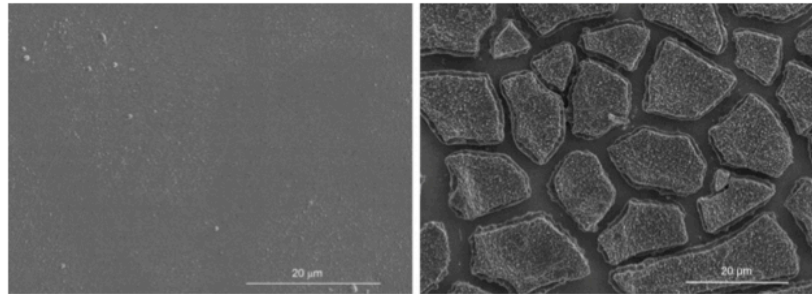


Figure 1.11: Li-ion battery silicon electrode before cycling (left) and after cycling (right) [35].

As seen in figure 1.11 in were the active anode material is amorphous sputtered silicon, as the battery goes through more cycles, the material becomes more cracked, and will eventually delaminate from the current collector underneath losing electrical connection and capacity.

To achieve a higher capacity Li-ion battery, higher specific capacity materials that suffer higher expansion and contraction need to be used, but the problem of the shortening of the life of the battery due to delamination of active materials must be solved first.

#### **1.4.3.- Silicon as a high capacity anode material.**

Energy density is one of the most important parameters of battery performance, since it measures the amount of energy stored per weight. Carbon, a conventionally used material in modern commercial Li-ion batteries has a specific capacity of 372mAh/g, on the other hand the theoretical specific capacity of silicon is 4212mAh/g [36]. This is more than 10 times the energy stored in the state-of-the-art commercial Li-ion batteries today.

Although exceptional in its capacity, silicon also suffers from extremely large volume change (300 – 400%) with the insertion/extraction of lithium in its structure [37]. During the lithium insertion into silicon a lithium-silicon alloy is formed, when this process is completed it is thought that  $\text{Li}_{22}\text{Si}_5$  is formed, where each atom of silicon accommodates 4.4 atoms of lithium, this explains the extreme volume expansion [38].

Having this extreme expansion while being inserted with lithium, silicon makes a very difficult material to be used, since the process described in section 1.4.2 diminishes the capacity of the battery in a few cycles. In order to improve mechanical properties of silicon and battery life, it is important to understand how material changes in each battery cycle, and how they degrade over time. Therefore, *in situ* techniques to monitor active battery material's volume change during cycling are needed.

### **1.5.- Previous work on measurement of electrochemical reaction-induced stress measurement in electrode materials of lithium ion batteries.**

As a conclusion from section 1.4 it is clear that the study of the mechanical expansion/contraction that active materials suffer in a Li-ion battery is very important. There are many efforts in the field to measure and quantify these effects and we can classify them into post-cycling studies and *in situ* experiments.

The post-cycling studies consist of assembling a battery with the desired active materials, cycling it for a determined number of times, disassembling the battery (destructive process) and then performing different studies, such as optical microscopy, scanning electron microscopy, or x-ray diffraction (XRD). In this field Obrovac [39] has assembled batteries with a nickel-silicon slurry as active anode material, then run those

batteries for different cycles and performed comparative XRD studies (figure 1.12) obtaining signatures that go from crystalline silicon to amorphous silicon and silicon-lithium alloys. The results obtained in this work are correlated with the expansion and contraction in active materials that also motivate the development of the *in situ* platform presented in this work.

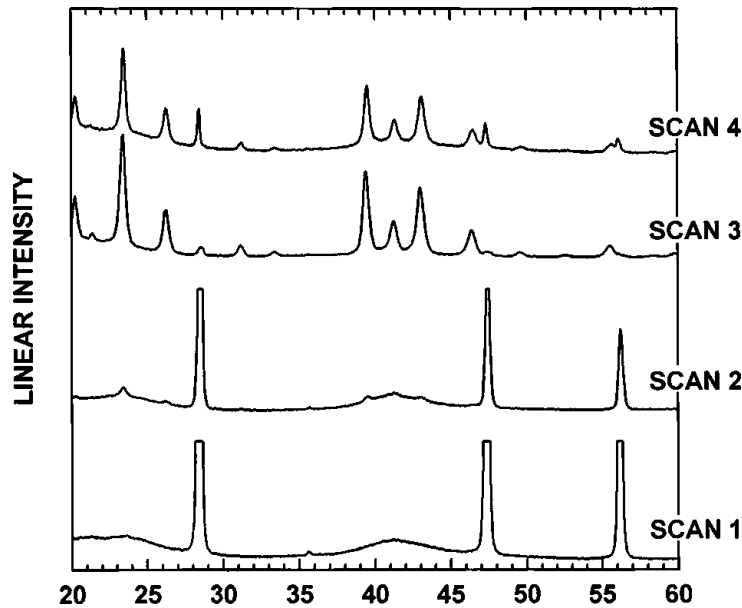


Figure 1.12: Ex situ XRD patterns of crystalline silicon electrodes [39].

The *in situ* works consist of methods that allow monitoring of the expansion and contraction of a Li-ion battery's active material while it is being lithiated and de-lithiated in real time and without the need to disassemble the battery. Destructive battery disassembly prevents multiple experiments on a single battery making impossible for example perform experiments at different current rates and voltages and compare them on a single battery . For example, acoustic monitoring of cracking events in microparticles of crystalline silicon in a Li-ion battery by Rhodes, Daniel *et al* [4] consisted of assembling a cell that uses crystalline microparticles of silicon in a slurry [40] and cycling them. While the cycling

was performed, acoustic data captured with a contact microphone is correlated with the discharge/charge data to obtain information on how and when the silicon microparticles crack. This unveiled important mechanisms behind intercalation of lithium into silicon that are very important for later works on this matter. Subsequent disassembly of the cell and SEM imaging was used to confirm the studies as seen in figure 1.13 and figure 1.14.

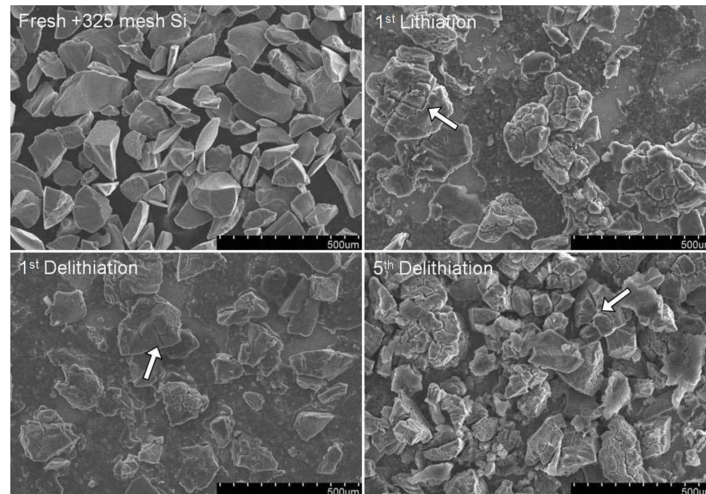


Figure 1.13: SEM image of silicon microparticles after different numbers of cycles [4].

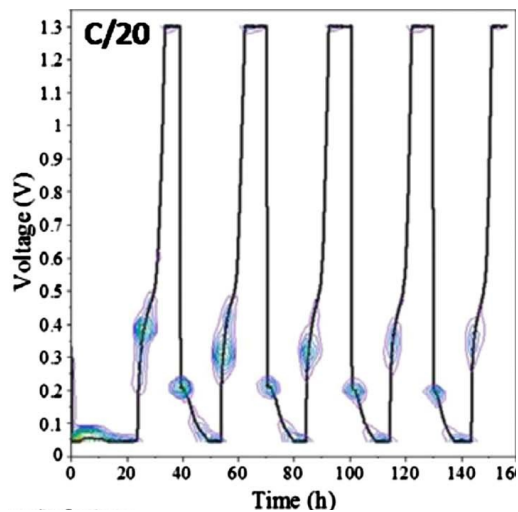


Figure 1.14: Acoustic activity (colored areas) versus voltage during cycling [4].

Another work in the *in-situ* field used a silicon wafer (3 inches in diameter) as a substrate for a silicon thin-film that served as the active electrode material (Sethuraman *et al* [41]). Silicon oxide ( $\text{SiO}_2$ ) was used as a chemical barrier and electrical insulator, and copper was used as a current collector. The assembled wafer created a custom electrochemical cell, which was cycled while performing measurements of the curvature of the wafer. The curvature was then related to surface stress via Stoney's equation. The curvature measurement was made by means of laser light and a charge-coupled device (CCD) camera. The experimental setup is depicted in figure 1.15. Some of the mechanical stress results from discharge/charge cycles are shown in figure 1.16. It should be noted that this setup uses a non-standard battery form factor and the entire bench top setup must be run inside an argon-filled hermetically sealed box.

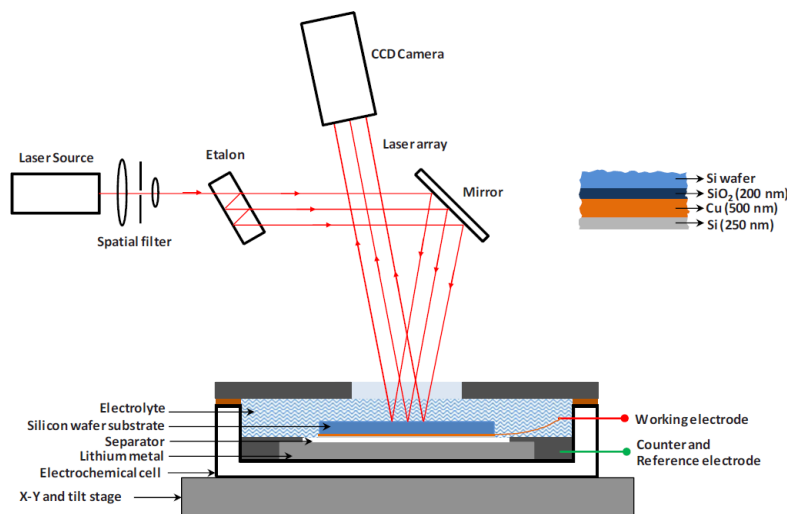


Figure 1.15: Schematic illustration of the electrochemical cell along with the setup to measure substrate curvature. [41].

The results of this work correlate stress on a thin-film silicon electrode while it is being cycled in a custom electrochemical cell. The authors obtained multiple results like the ones shown in figure 1.16, and measured stress/strain behavior on thin-film silicon electrodes, this is further discussed in chapter 5.

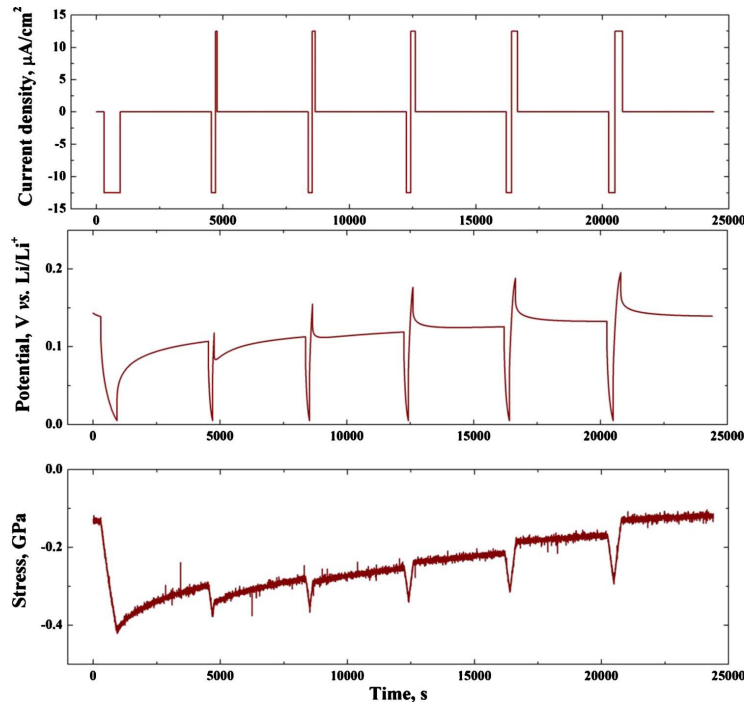


Figure 1.16: Representative current density, potential, and stress transients obtained from the stress-potential experiment in a lithiated-silicon electrode [41].

## 1.6.- Platform overview.

In the previous sections the Li-ion battery technology has been presented, along with its limitations. The problem of volume expansion and stress in active materials was discussed and some of the efforts to study this effect were described. For this work, MEMS technology has been chosen to build a measurement platform of the stress in the active material in a Li-ion battery.

The platform consist of a MEMS sensing chip, a battery package, a battery testing machine and an optical microscope with image capturing capabilities. The detailed description of these elements is on chapter 2.

The principle of operation is based on a custom made battery with the sensing element inside that is cycled while the volume expansion/contraction is measured. The MEMS sensing chip measures the active material expansion/contraction using a thin membrane that deflects with this effect, and a readout of the fringe changes of a Fabry-Perot interferometer as proposed by Koev in [42].

Among the advantages of using MEMS is the unique possibility to miniaturize the sensing element and include it in a battery package very similar to a commercial battery. Having the sensing element inside a package that is mostly similar to the standard packages used for electrochemical experiments is very important; reliable battery assembling and testing can only be performed having this capability.

This high level of integration of the sensing element in a trustworthy electrochemical platform is unparalleled among other *in situ* measurement works.

## **2.- Design of the monitoring platform.**

The platform is based on a custom modified Li-ion coin cell battery that contains the MEMS sensing chip inside. The sensing mechanism relies on an interferometric measurement technique. The sensor itself consist of a singular Fabry-Perot cavity interrogated by single-wavelength illumination [43]. The MEMS chip enable monitoring the expansion and contraction of the battery active material. To do this, the MEMS chip has an electrochemical micro-cavity that ends in a thin membrane which will bend as the active

electrode material expands and shrinks. This membrane comprises one of the mirrors of a Fabry-Perot interferometer, and when flexed due to expansion or contraction will produce an optical output that can be used to monitor the active battery material volume change. Figure 2.1 shows the basic functioning scheme of the MEMS chip in the platform. The chain of events that lead to the active electrode material stress monitoring is exposed in figure 2.2.

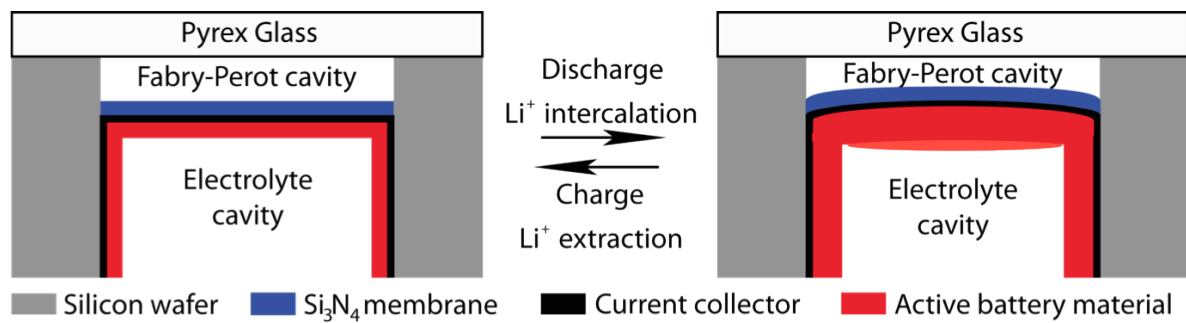


Figure 2.1: Schematic representation of the sensing principle of the MEMS chip platform.



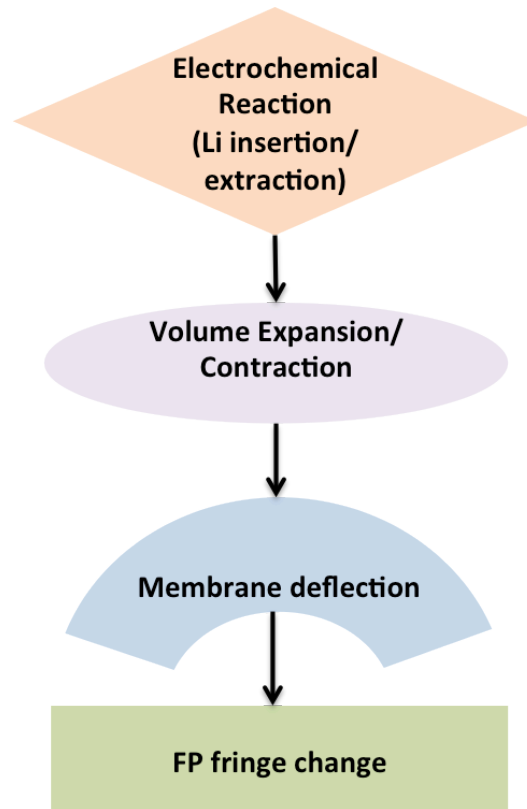


Figure 2.2: Schematic of the Fabry-Perot monitoring platform operation.

### 2.1.- Design requirements and considerations.

As it was discussed in section 1.4.2, the mechanical expansion-contraction of active electrode materials is a very important factor limiting the lifetime of a Li-ion battery; hence, monitoring it is very important. A MEMS-based design capable of measuring the mechanical activity at the micro-scale is proposed.

The monitoring platform elements and requirements:

- A MEMS chip containing micro-cavities ending in a thin membrane that forms a Fabry-Perot interferometer at the bottom. The chip should be capable of being coated with the desired active material, and the flexible membrane should be able to bend under the stress of the battery material that is being tested. Figure 2.3 shows the cross section of the initial design.

- An electrochemical package with a window (to optically interrogate the Fabry-Perot interferometer), where the chip is inserted. This package should be completely sealed due to the high reactivity of lithium with air [44]. It also must provide good electrical connections, and finally it should be able to be assembled inside an argon-filled glove box (see figure 2.8).
- A microscope to capture the images of the Fabry-Perot interferometer as the battery is being cycled. The light source should be of a known wavelength and in the range of red light (660nm). Also a camera and a capturing system are needed to record the Fabry-Perot fringe changes as the experiment is performed. See figure 2.18.

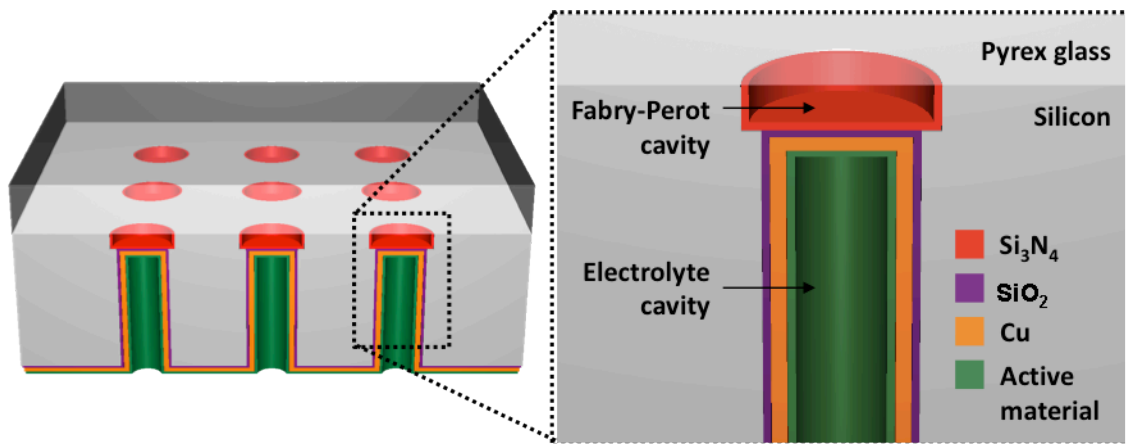


Figure 2.3: Schematic representation of the suggested MEMS chip monitoring platform.

## 2.2.- The MEMS sensing chip.

### 2.2.1.- Overview of the architecture and materials used.

The MEMS chip serves two purposes:

- To hold the active electrode material to be measured.
- To monitor the stress using the Fabry-Perot device.

With these requirements an architecture consisting of a double-sided polished silicon wafer and a Pyrex borosilicate glass wafer was established. Figure 2.3 shows such architecture, and how the Fabry-Perot cavity is formed by the silicon nitride ( $\text{Si}_3\text{N}_4$ ) membrane and the Pyrex glass. The chip was originally designed as a 2 cm by 2 cm square chip containing 36 microcavities with their respective Fabry-Perot interferometers (in figure 2.4 the layout of the chip is shown). This design was chosen to increase the yield of fabrication. Due to the fragile nature of the sensing membranes [45] some are expected not to survive the entire fabrication process, hence the need to have multiple devices per chip.

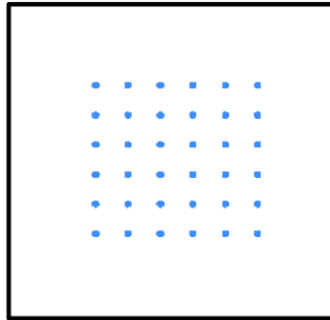


Figure 2.4: MEMS chip device layout.

### 2.2.2.- Device dimensions.

The dimensions of the Fabry-Perot interferometric cavities were governed by the 660nm wavelength of light to be used in the experiments and the equations of section 1.3. The measuring membranes and electrochemical cavities were chosen empirically based on standard capabilities in normal practices in MEMS fabrication techniques [10]. Although a design and simulation methodology would have produced data on the structures to be fabricated, microfabrication is far from ideal. Finally the decisions made on the general dimensions of the devices proved to produce working devices with a yield of over 50%.

Table 2.1 shows the chosen dimensions. Figure 2.5 maps the device to the mentioned dimensions.

Device Dimension	Value
Membrane diameter	150 $\mu\text{m}$ , 200 $\mu\text{m}$ , 250 $\mu\text{m}$ and 300 $\mu\text{m}$ .
Membrane thickness	700nm
Electrochemical cavity depth	488 $\mu\text{m}$
Fabry-Perot length	12 $\mu\text{m}$

Table 2.1: MEMS chip design dimensions.

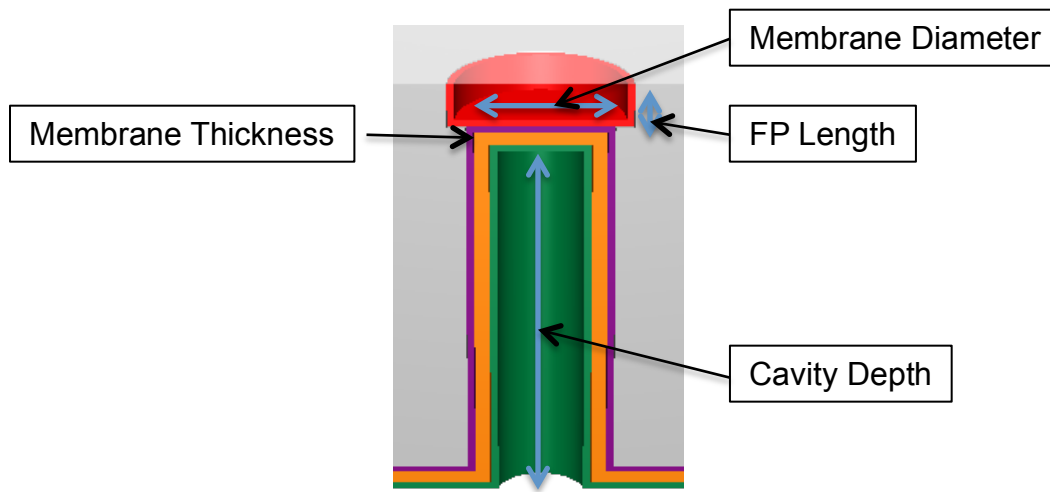


Figure 2.5: Schematic of device dimensions.

The different diameter membranes correspond to different chips that are co-fabricated on a single 4" wafer. This design decision was made to experiment with different membranes and their chip yield, being of a uniform thickness, larger membranes are more fragile.

Regarding the length of the Fabry-Perot interferometer, in the special case considered in this work where the light comes at a right angle and the cavity is in vacuum (see chapter 3), the equation (1.1) require that the first order fringe needs a minimum

optical path length  $l$  of  $\lambda/2$ . A 10 $\mu\text{m}$  to 12 $\mu\text{m}$  length of the Fabry-Perot cavity will be producing several fringes at the wavelength of light (660nm), which is correct for the purpose of the experiment.

## **2.3.- The electrochemical package.**

### **2.3.1.- Technical and practical design considerations.**

As mentioned in section 2.1 the electrochemical package is a container that holds the MEMS chip and the rest of the elements of the battery: separator, liquid electrolyte and metallic lithium. This package should be equivalent to the package of a commercial Li-ion battery to enable correct battery performance [46] (figure 2.6). Additionally, the package must have an optical window, be hermetically sealed, resist dehydration at 100°C, and provide good electrical conductivity from the case to the chip.

A special consideration of the assembly of the package should be noted: since lithium is extremely reactive with air components, especially oxygen and moisture [45], the assembly of the battery package should be done inside an argon glove box (figure 2.7). In addition, all the battery package components and materials must be extremely dry, so dehydration in a vacuum oven at 100°C is needed.

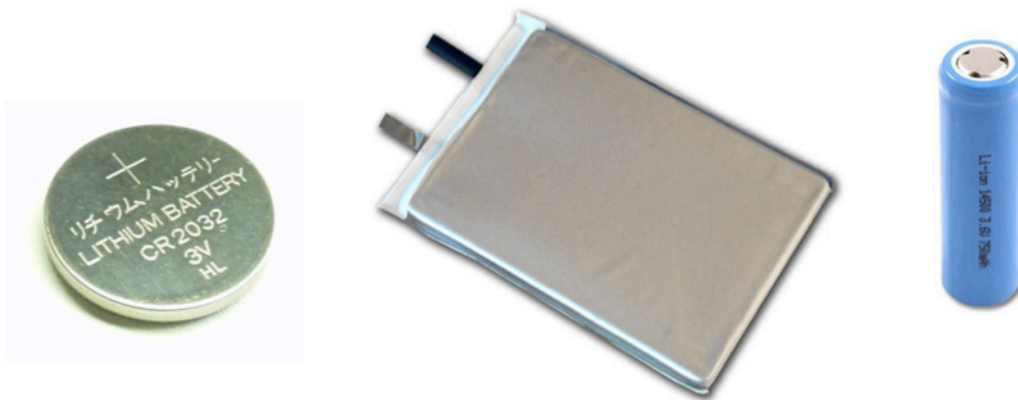


Figure 2.6: Commercial Li-ion battery packages. Coin cell (left), Pouch Cell (center), 18500 cylindrical cell (right).



Figure 2.7: Argon-filled glove box for Li-ion battery assembly.

### 2.3.2.- Design of the first generation package.

All the above considerations were taken with the first generation package, and a design that could accommodate the 2 cm by 2 cm MEMS chip was made. This first experimental package used exclusively commercially available off-the-shelf components. The schematic of the design can be seen in figure 2.8.

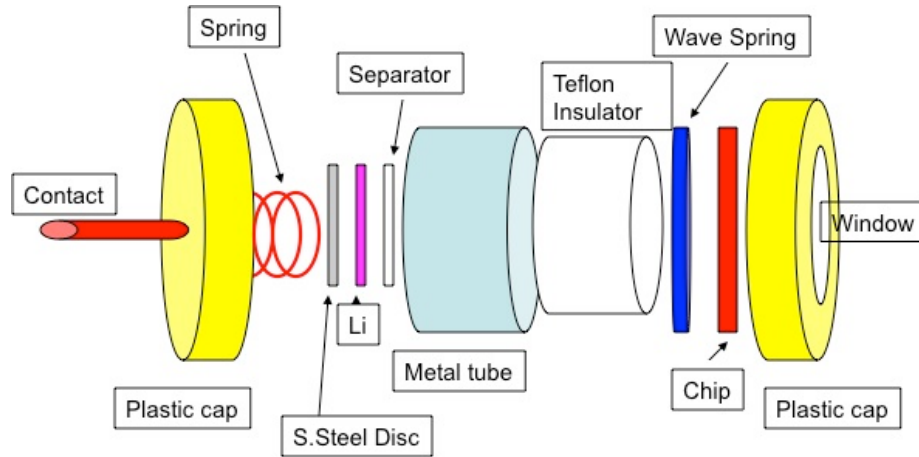


Figure 2.8: Schematic of first generation experimental package.

Nylon caps and 304 stainless steel threaded tube were used as the main package housing. The rest of the components are described in the above figure. Due to the coaxial connection nature of the MEMS chip, the electrical connection in this package is made between the upper contact and spring and the body of the stainless steel tube through a metal washer and spring. The package was built and assembled inside an inert argon environment provided by a glove box. Figure 2.9 shows the fabricated package.

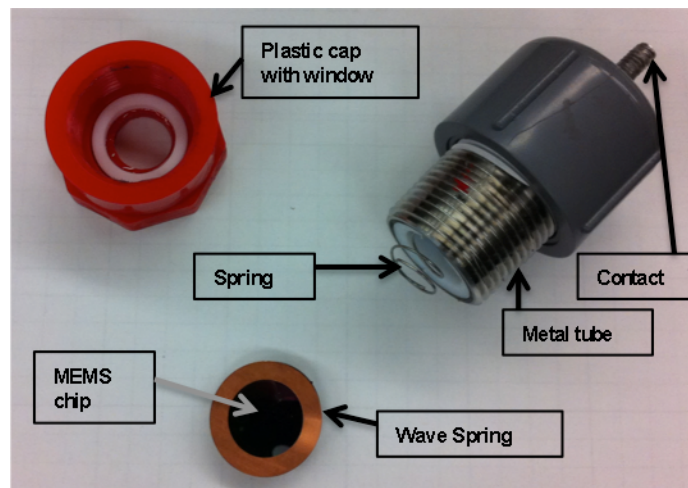


Figure 2.9: First generation package parts.

Due to the round shape of the plastic cap holding the MEMS chip, the assembly of this package proved to be very difficult. The adjustment of the upper part into the red cap proved to be critical: an under tightening produced a very bad electrical contact, but over tightening broke the MEMS chip.

### **2.3.3.- Design of the second generation package.**

For the second generation of the package a chip-holding part to replace the off-the-shelf plastic cap was needed. Ideally the part would have been made of stainless steel, but machining the needed thread on such a material proved to be very difficult. The purpose of this design was to overcome the assembly and chip breaking problems experienced on the previous generation package.

A custom-made part was designed including a square recess for the MEMS chip. This new end cap was fabricated in the University of Maryland Physics Department machine shop, first in polycarbonate and finally in copper. Figure 2.10 shows a schematic of the custom-made part; notice the square recess of 1mm deep to accommodate the MEMS chip. An O-ring performed the sealing between the chip and the custom-made part.



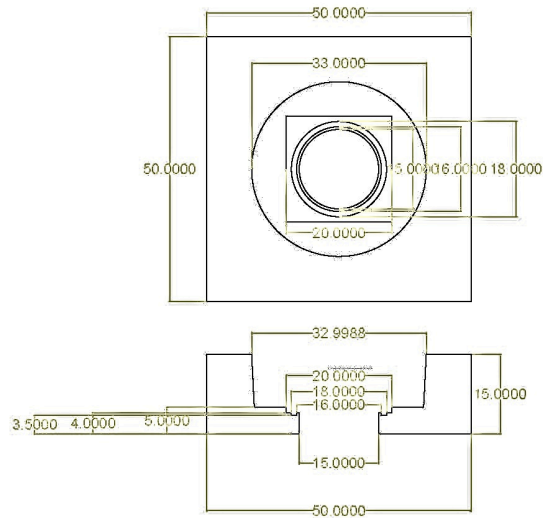


Figure 2.10: Second-generation package schematic.

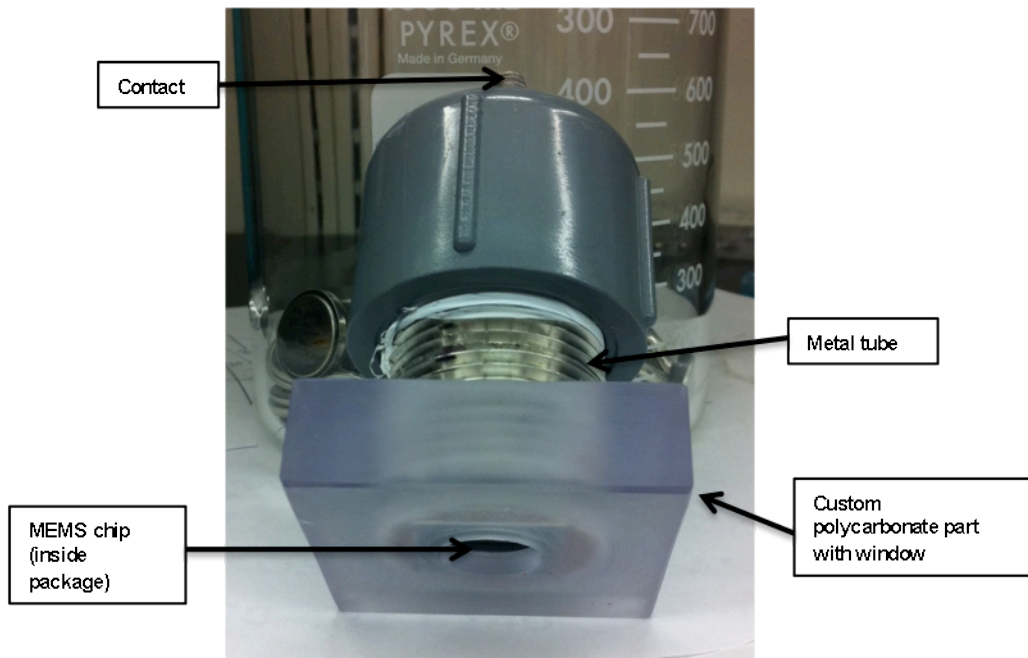


Figure 2.11: Second-generation package with chip-holding part fabricated on polycarbonate.

Figure 2.11 demonstrates the polycarbonate implementation of this design. The over tightening/under tightening problem was solved and very few MEMS chips were broken

when assembling this package inside the glove box. However, during electrochemical tests, this package revealed a leaking problem. Attempting to seal the threaded junction between the stainless-steel tubing and the custom-made part proved to be difficult. Several compounds, including Teflon tape, Loctite<sup>™</sup> 518 and Loctite<sup>™</sup> 55 , were used giving mixed results that created uncertainty in the experiments.

#### **2.3.4.- Design of the third generation package.**

Previous designs proved to be insufficient in isolating the battery components from the ambient environment. Since Li-ion battery electrodes must avoid any contact with air components, a different approach for the MEMS chip package was tried. A third generation package based on modified standard “coin cells” that are traditionally used for Li-ion testing in scientific laboratories was developed. Coin cells [47] are reliable, cheap and relatively easy to assemble in the glove box. Changing the package to this new format required the modification of the MEMS chip, which added in fabrication complexity, but resulted in increased reliability.

The coin cells used are 2032 type; they are 20 mm in diameter and 3.2 mm in height when assembled. This gives less than 2.8mm of internal vertical space. Given this constraint and the desire to have a method that produces predictable results, adhesive tapes were used to seal and to make electrical contact from the chip to the battery case. The use of adhesive tapes in contrast to paste or liquid adhesives assure consistent adhesive performance, and most importantly a thickness that does not vary from the manufacturer’s specifications.

To use the MEMS chip inside a 2032 coin cell two modifications of the chip were needed:

1. The original design was a 2cm x 2cm chip with 36 devices. To fit in the coin cell the chip was cut in 4 equal parts, giving a 1cm x 1cm chip containing 9 devices in each new MEMS chip.
2. The original MEMS chip had a coaxial electrical connection design. Since the coin cell has a sandwich structure from top to bottom, it was necessary to modify the electrical connection to the MEMS chip from its original configuration to a top to bottom path. The problem is that the bottom of the chip consists of the Pyrex optical window, which is an excellent insulator. This was solved using an extra step of metal sputtering and a new step for shadow masking. The picture and schematic of the new top-to-bottom design can be seen in figure 2.12, and the fabrication process details are exposed in section 3.5.2.

The assembly of the coin cell with a window requires only three steps, after custom-modifying the coin cell cases with precision-perforations. Figure 2.13 depicts the battery assembly process.

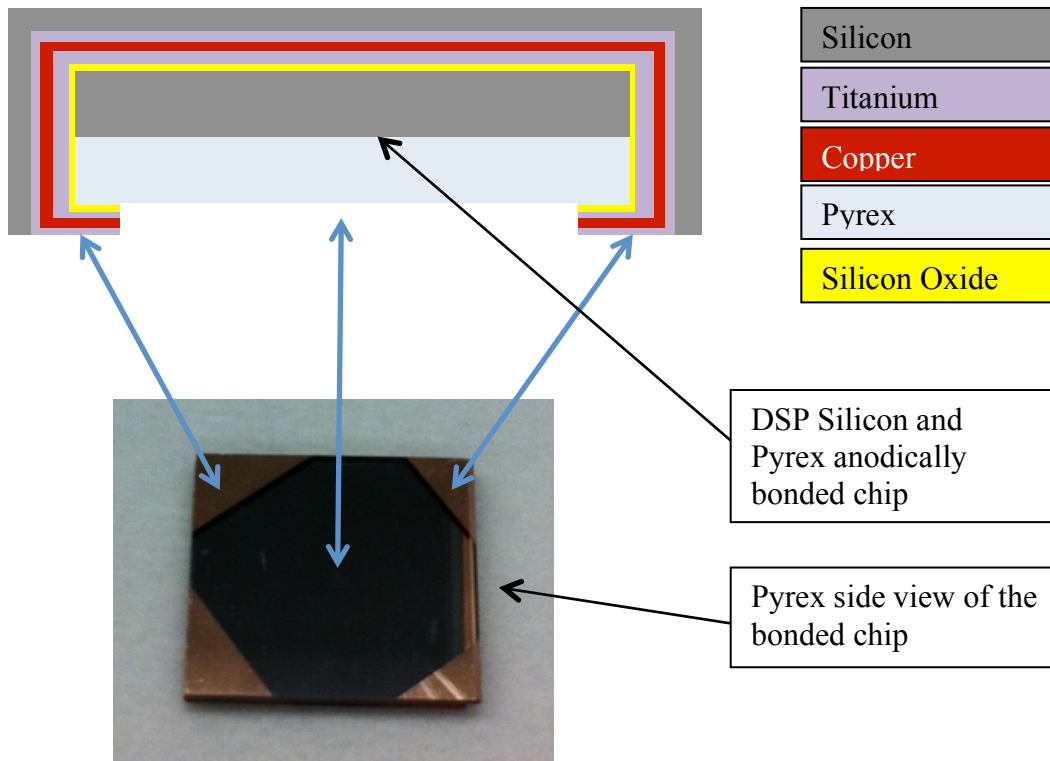


Figure 2.12: Thin film coating schematic and picture.

For the sealing and electrical contact 3M 1182 copper tape from Ted Pella Inc. was used. This self-adhesive and conductive tape is 90 microns thick and has less than 1 Ohm of resistance (measured using a 2-contact multimeter). The low resistance enable for a good chip-to-package connection that is crucial for any battery.

A critical aspect of this design is to fit all the components inside the coin cell battery case without applying too much pressure on the chip to avoid damaging it. The total available thickness inside the coin-cell is about 2.8 mm. The thicknesses of the components used are shown in table 2.2.




	<p>Step 1: custom-modified precision-perforated coin cell case.</p>
	<p>Step 2: double sided copper tape is applied, and the chip is prepared to be glued.</p>
	<p>Step 3: chip is flipped and glued to the tape. On the right we can see the same coin cell from the window side.</p>

Figure 2.13: Third generation package based on a modified coin cell: assembly.

<b>Component</b>	<b>Thickness</b>
3M 1182 Copper Tape	0.09mm
Fabry-Perot Chip	1mm
Separator	0.02mm
Lithium foil	0.5mm (specifications)
SS Disc	0.5mm
Wave Spring	1mm (uncompressed) to 0.5mm(compressed)
<b>TOTAL Thickness</b>	<b>2.61mm</b>

Table 2.2: Thickness of components inside the coin cell.

An undesired effect of the use of the coin cell casing became evident after assembling a coin cell with Fabry-Perot MEMS chip: the way the coin cell is closed the battery is by slightly deforming and reducing the size of the two halves of the can. This volume reduction results in increased hydraulic pressure of the electrolyte inside the coin cell and this broke the very thin silicon nitride Fabry-Perot membranes in two opportunities. To cope with this, pressure-release holes were made on the top half of the cell, and after the assembly of the cell the holes were closed using the same copper tape that was used to hold the Fabry-Perot chip inside the battery. Finally, this modified coin cell package was used with the MEMS chips and demonstrated no membrane destruction and good electrochemical performance. Figure 2.14 shows the pierced coin cell can and the tape-sealed assembled coin cell.



Figure 2.14: Pierced coin cell can (left). Assembled and taped cell (right).

In chapter 4.3, we will see that this package design delivered very reliable electrochemical results due to the correct sealing, the optimized electrical connection and the streamlined assembly process.

## 2.4.- The testing setup.

### 2.4.1.- Overview and design.

In order to obtain Fabry-Perot fringe images using the MEMS chip, a testing setup was built. The Fabry-Perot interferometer fringe pattern reading needs a light source and an image viewing system. Figure 2.15 shows a simplified schematic of this setup.

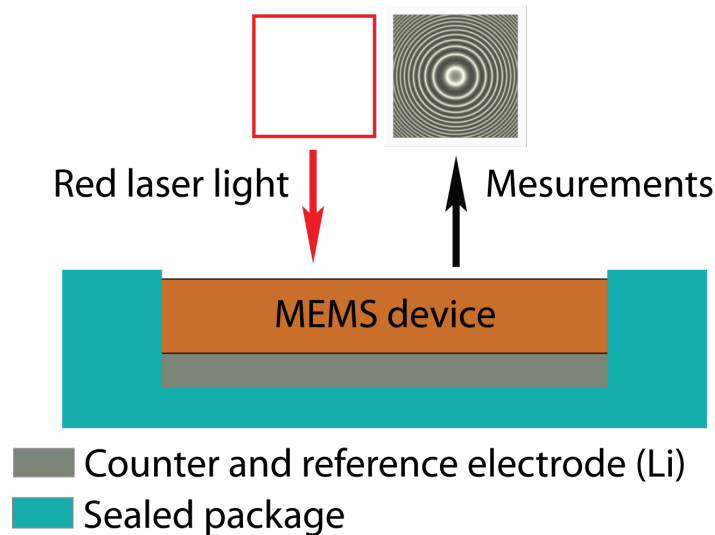


Figure 2.15: Simplified schematic of measurement setup.

Due to the small size of the Fabry-Perot interferometers, an optical microscope is needed in order to properly view and measure the fringes. As liquid electrolyte is used, empirical knowledge dictates that the MEMS chip Pyrex side must be kept facing downwards to make sure that the electrolyte is always in contact with the active materials, in which case the optical microscope should be looking upwards (inverted optical microscope). An Optixcam 5-megapixels USB-connected CMOS camera and a computer with the Optixcam software were used to capture the images in fixed time intervals. A de-

speckled 660 nm laser light source was used for a frequency-stable and diffused illumination.

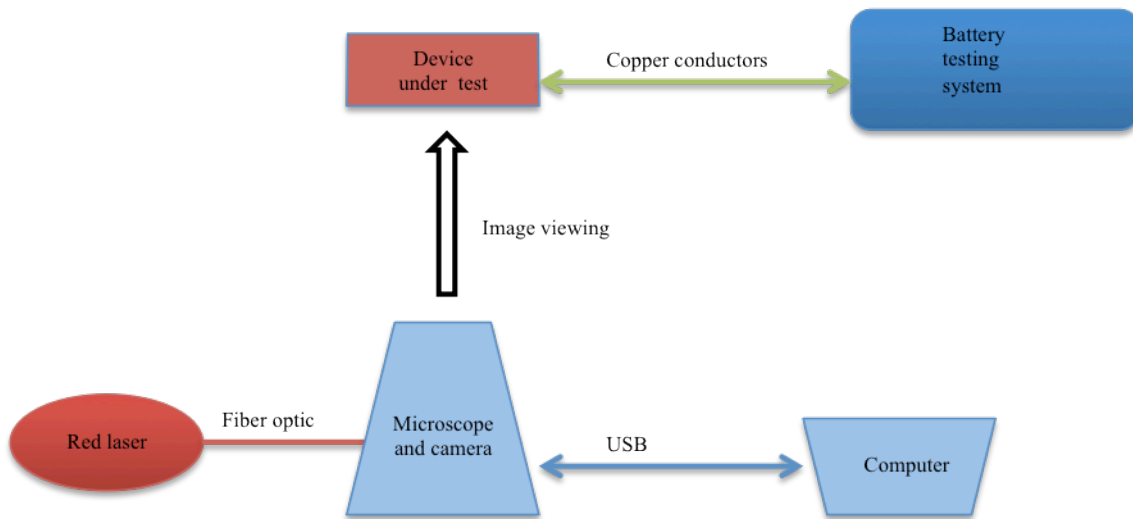


Figure 2.16: Schematic of the measurement platform setup.

In figure 2.16 the complete schematic for the setup is shown, including the battery testing system that is responsible for cycling the MEMS chip-based battery through a pre-programmed set of charge and discharge cycles.

#### 2.4.2.- Inverted microscope and camera.

In order to increase the flexibility of the setup, a Leica MZ12<sub>5</sub> stereo microscope with zoom lens was used. This microscope has about 20cm of working distance, allowing the placement of the device under test at a distance that permits to overcome the bulkiness of the electrochemical first and second generation package. The measurement setup structure was made on top of a floating optical table to obtain a stable inverted microscope (see figure 2.17).



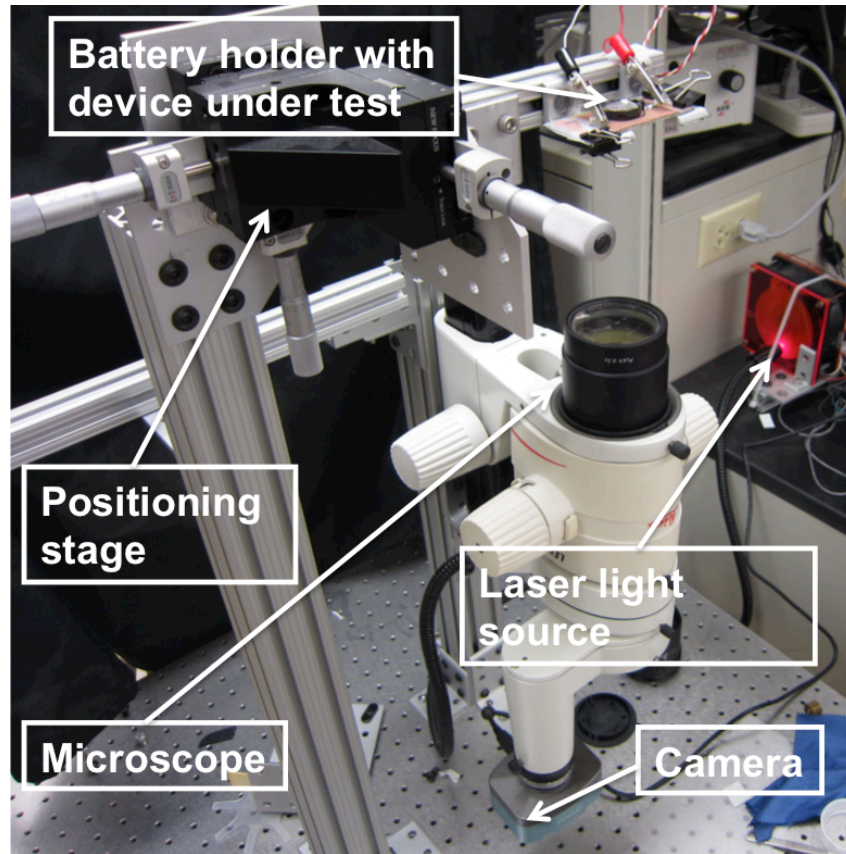


Figure 2.17: Complete experimental setup.

The camera used is an OptixCam OCS-5S CMOS 5-megapixel camera, with a 2592 pixel by 1944 pixel resolution. The entire camera controls is operated with a factory supplied software package. This software has the capability of time-lapse capturing of images, which is fundamental for this experiment. The camera can be seen on the lower part of figure 2.17.

#### 2.4.3.- Laser light source.

A monochromatic light source is needed to obtain the best resolution in the Fabry-Perot fringes. A red laser diode source with a wavelength of 660nm was chosen because of the very narrow bandwidth of the light produced by the laser diode. This wavelength is

appropriate for the Fabry-Perot interferometer dimensions chosen in the design of the chip. As discussed by Koev [42], the light of a laser diode is spatially and temporally coherent, so when it scatters at a surface, it produces a random interference called speckle [48]. To eliminate the speckle a rotating diffuser is used, which consists of a semi-transparent ground disc that rotates using a 2000rpm electric motor. The effect produced is a light that is randomly modulated spatially, hence eliminating the speckle. To make sure that this modulation does not affect the image capture; the approximate modulation time is 1 microsecond while the camera capture time is tens of milliseconds. In figure 2.18 the diffused laser light can be seen coming through the rotating disc.

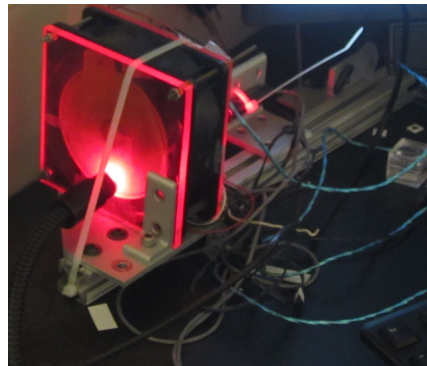


Figure 2.18: De-speckled laser light source.

#### **2.4.4.- Battery testing station.**

A 20-channel Arbin Instruments battery testing system was used for the experiments. This system is capable of multiple testing schemes, but for our purposes we used a constant-current programmed testing. A single channel of the machine was used, while the rest of the channels would perform complementary testing on other devices. During the test, the system logs the voltage and current data in a computer file, which was later, used for the experimental analysis.

All the components designed, assembled and built described in this chapter constitute all what it is necessary to perform the experiments to measure mechanical expansion/contraction on li-ion battery electrodes. The fabrication of the MEMS chip is presented in the next chapter.



Figure 2.19: Arbin Instruments Battery testing system.

### **3.- MEMS Fabry-Perot chip Fabrication.**

#### **3.1.- MEMS chip mask design.**

In chapter 2 the basic MEMS chip design was presented, and a 36 device per chip architecture was established. Due to the relatively large size of each chip, only 9 can be fabricated on a standard 4inch wafer. As it was mentioned before, there are several sizes of devices ranging from 150 $\mu$ m to 300 $\mu$ m in diameter.

The process requires three masks for photolithography defining the Fabry-Perot cavities, the membranes and the electrochemical cavities. The contact lithography [10] masks were designed using Autocad software and fabricated by Photosciences Inc. on chrome on quartz glass with a 0.5 $\mu$ m precision. Figure 3.1 depicts the first mask that

defines the Fabry-Perot cavities and the architecture of the whole chip (notice the left and right alignment marks that will be used to align the posterior photolithography steps).

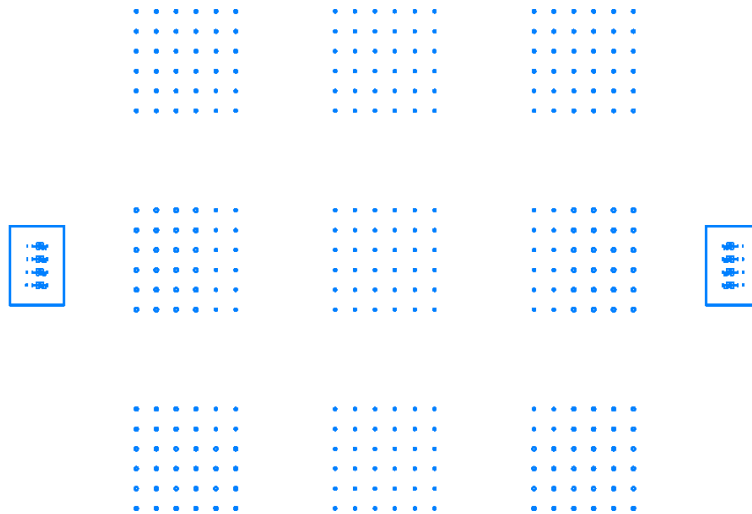


Figure 3.1: First mask (first DRIE).

The second mask, which defines the silicon nitride ( $\text{Si}_3\text{N}_4$ ) membranes, and the third mask, which defines the deep electrochemical cavities, are shown in Appendix A.

### 3.2.- Fabrication process flow.

All the processes involved in the fabrication of the MEMS chip were done in the clean room of the MEMS Sensors and Actuators Laboratory and the clean room of the University of Maryland's nanofabrication facility called the FabLab. The silicon wafers were double side polished, 100mm in diameter with a thickness of  $495\mu\text{m}$ - $505\mu\text{m}$ , p-doped ( $10\Omega/\text{cm}$ ) and orientation  $\langle 100 \rangle$ . The Pyrex wafers were borosilicate glass, 100mm of diameter with a thickness of  $475\mu\text{m}$ - $525\mu\text{m}$ , double side polished with a RMS roughness less than 1.5nm.

The MEMS chip fabrication process flow is shown in figure 3.2. Steps (a) to (c) define the Fabry-Perot cavity, steps (d) to (g) define the membrane, steps (h) to (k) define the electrochemical cavity, step (l) defines the Fabry-Perot interferometer and on step (m) the electrochemical cavities are passivized.

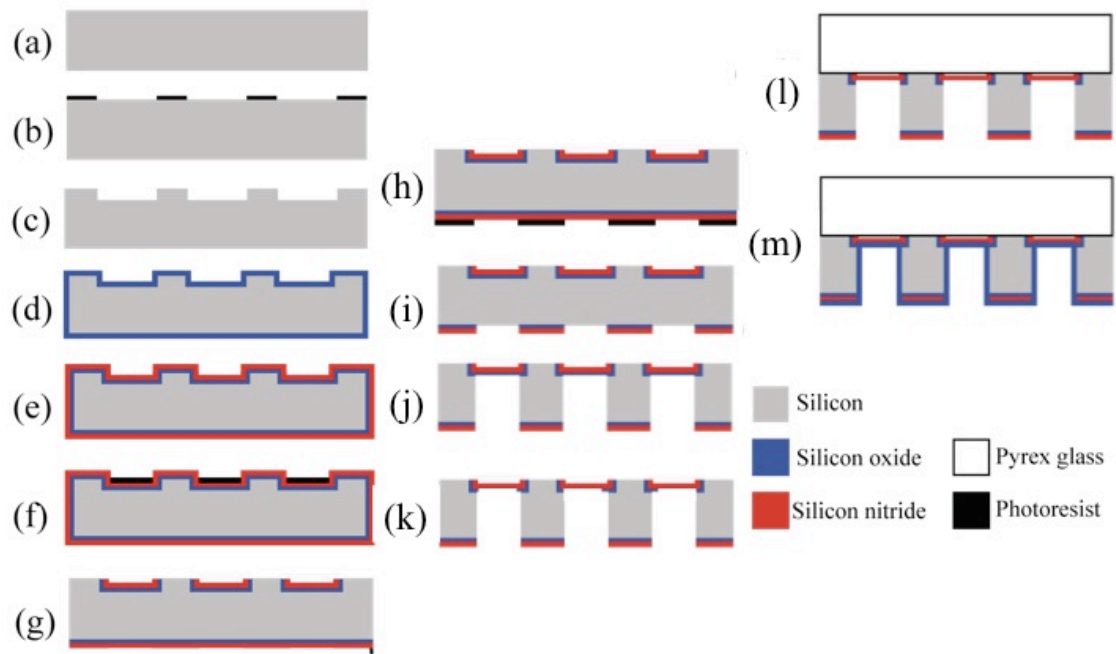


Figure 3.2: Schematic of MEMS chip process flow.

Fabrication details of the process flow are given in table 3.1, for further information on the DRIE, reactive ion etching (RIE) and anodic bonding parameters, please refer to Appendix B.

Process Step	Mask	Photoresist	Tool	Step purpose	Details
a- Process begins.					A double side polished wafer is used to begin.
b- Lithography using shipley positive resist.	First DRIE	Shipley 1813	P-6708D Precision Spin Coating System. Spinner.  Quintel Q4000 mask aligner.	The Fabry-Perot cavities are defined.	<ol style="list-style-type: none"> <li>1. Wafer dehydration at 110°C for 5 min.</li> <li>2. HMDS spin at 3000rpm for 30 sec</li> <li>3. Shipley 1813 spin at 3000rpm for 30sec.</li> <li>4. Soft bake at 110°C for 1min.</li> <li>5. Exposure : 180mJ</li> <li>6. Develop: 40sec on 352. Rinse and dry.</li> </ol>
c- 12µm deep DRIE and photoresist strip			STS Deep Reaction Ion Etcher.  Veeco Dektak Surface profilometer.	Fabry-Perot cavities are etched.	<ol style="list-style-type: none"> <li>1. On STS etcher etch for 14 cycles using Bob3dss recipe.</li> <li>2. Strip photoresist using organic solvent procedure.</li> <li>3. Confirm etch depth on contact profilometer: should be 12µm</li> </ol>
d- 300nm thermal SiO2			CVD systems LPCVD furnace.	DRIE etch-stop is deposited.	
e- 700nm LPCVD Si <sub>3</sub> N <sub>4</sub>			CVD systems LPCVD furnace.	Sensing membrane material is deposited	
f- Lithography for membrane definition.	Second Mask	AZ9260	P-6708D Precision Spin Coating System. Spinner.  Quintel Q4000 mask aligner.	Photoresist is applied to protect the future sensing membrane from the RIE of step g.	<ol style="list-style-type: none"> <li>1. Wafer dehydration at 110°C for 5 min.</li> <li>2. HMDS spin at 3000rpm for 30 sec</li> <li>3. AZ9260 spin 500rpm for 15 sec, 1500 rpm for 45 sec.</li> <li>4. Soft bake at 100°C for 3min.</li> <li>5. Re-hydrate in 45% ambient humidity for 30min.</li> <li>6. Exposure : 300mJ</li> </ol>

					7. Develop: 6min on az400k. Rinse and dry
g- RIE to remove Si <sub>3</sub> N <sub>4</sub> and SiO <sub>2</sub> from top side			Oxford Plasmalab 100 fluorine etcher.	Si <sub>3</sub> N <sub>4</sub> and SiO <sub>2</sub> are removed so anodic bonding will be possible.	<ol style="list-style-type: none"> <li>1. On Oxford Fluorine etcher etch for 3:30 minutes using SergioSiN recipe.</li> <li>2. Confirm oxide elimination through hydrophobicity.</li> <li>3. Strip photoresist using acetone, methanol and isopropanol.</li> </ol>
h-Lithography for electrochemical cavity definition.	Back side DRIE	AZ9260	Headway EC-101 spin coater.  EVG 620 mask aligner.	The electrochemical cavities are defined and aligned with the previous structures.	<ol style="list-style-type: none"> <li>1. Wafer dehydration at 110°C for 5 min.</li> <li>2. HMDS spin at 3000rpm for 30 sec</li> <li>3. AZ9260 spin 500rpm for 15 sec, 1000 rpm for 45 sec.</li> <li>4. Soft bake at 100°C for 3 min.</li> <li>5. Re-hydrate in 45% ambient humidity for 30min.</li> <li>6. Exposure : 300mJ</li> <li>7. Develop: 6min on az400k. Rinse and dry.</li> </ol>
i- RIE to begin cavity etch.			Oxford Plasmalab 100 fluorine etcher.	Si <sub>3</sub> N <sub>4</sub> and SiO <sub>2</sub> are removed from cavities previous to DRIE.	<ol style="list-style-type: none"> <li>1. On Oxford Fluorine etcher etch for 3:30 minutes using SergioSiN recipe.</li> </ol>
j- Electrochemical cavity etch.			STS Deep Reaction Ion Etcher.	Electrochemical cavities are etched.	<ol style="list-style-type: none"> <li>1. STS etcher etch for 220mins using Bob3dss recipe.</li> <li>2. Confirm etch visually inspecting 300μm membrane side. If open: cover 300μm pits with kapton tape to avoid further etching.</li> <li>3. STS etcher etch</li> </ol>

					<p>for 25mins using Bob3dss recipe.</p> <ol style="list-style-type: none"> <li>Confirm etch visually inspecting 250<math>\mu</math>m and 200<math>\mu</math>m membrane side. If open: cover pits with kapton tape to avoid further etching.</li> <li>STS etcher etch for 22min using Bob3dss recipe.</li> <li>All membranes should be open.</li> </ol>
k- SiO <sub>2</sub> elimination for smooth membranes surface.				SiO <sub>2</sub> is removed from the bottom of sensing membranes.	<ol style="list-style-type: none"> <li>Dip in 5:1 BOE for 3min.</li> <li>Rinse thoroughly with deionized water.</li> </ol>
l- Anodic bonding to Pyrex wafer.			EVG 501 bonder.	The Pyrex glass is bonded forming the Fabry-Perot interferometer.	<ol style="list-style-type: none"> <li>Clean both wafers on Piranha at 80°C for 2 min.</li> <li>Rinse and dry on rinsing machine.</li> <li>Use EVG bonder follow the standard anodic bonding procedure but applying 1000V.</li> </ol>
m- SiO <sub>2</sub> Passivation.			Oxford Plamalab 100 PECVD.	Electrochemical cavities are passivized.	

Table 3.1: Detailed process flow.

After the fabrication was completed, individual 2cm x 2cm chips were diced using a MicroAutomation Industries model 1006 dicing saw.

### 3.3.- Fabrication details.

During the fabrication process, scanning electron microscope (SEM) images were taken to confirm and correct different process methods and recipes. In order to take these



images, MEMS chips had to be cleaved through the electrochemical cavity axis, resulting in some imperfect surfaces that are revealed on the SEM imaging.

After performing step (c) an SEM image was taken to verify the sidewall quality and the bottom part (to later become a membrane) flatness of the Fabry-Perot cavity. Figure 3.3 shows the SEM image and the location on the device schematic. Typical scalloping due to the DRIE process [10] is found, this does not negatively affected the performance of the MEMS chip, since the surface of interest is the bottom. Also a cavity length of  $10.7\mu\text{m}$  is observed; as seen in section 2.2.2 a length of  $10\mu\text{m}$  to  $12\mu\text{m}$  is acceptable for this dimension.

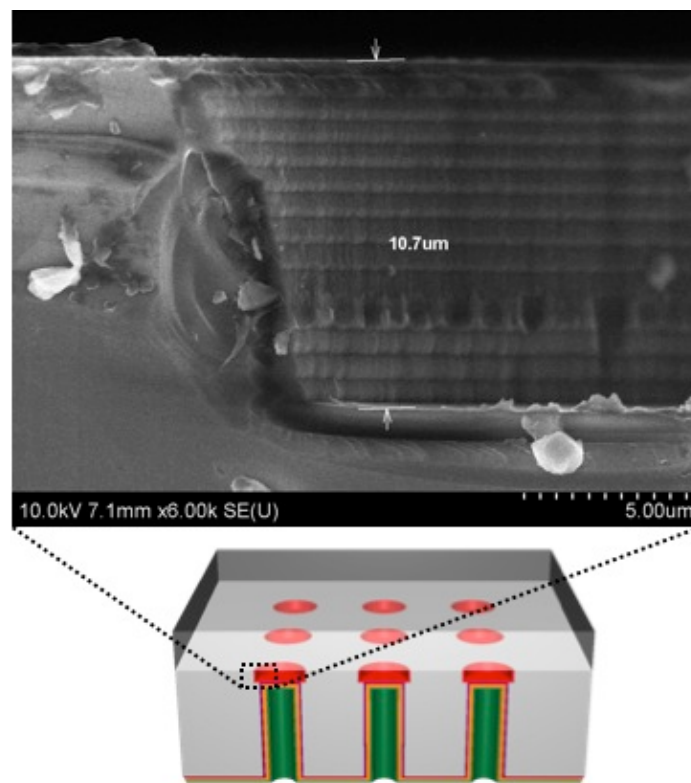


Figure 3.3: SEM image of the Fabry-Perot cavity sidewall.

Membrane flatness is very important (as discussed in section 2.2.3) so SEM imaging of the membrane to confirm flatness and thickness was done (figure 3.4). An

800nm thick membrane was fabricated in this case, which is very close to the 700nm originally specified, not affecting substantially the desired results.

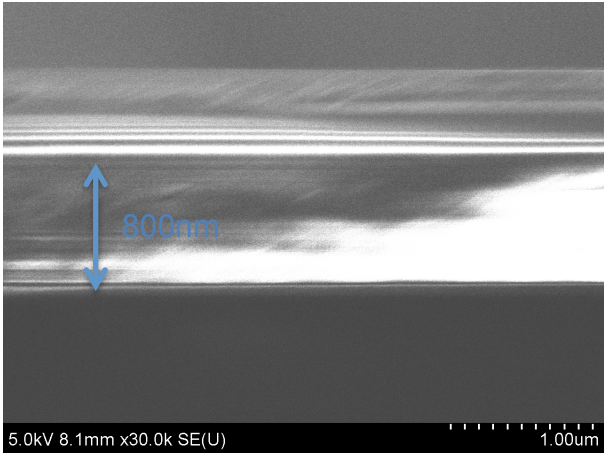


Figure 3.4: SEM image of the silicon nitride membrane.

The complete device can be seen in figure 3.5. The sample is placed with the Fabry-Perot cavity on the bottom.

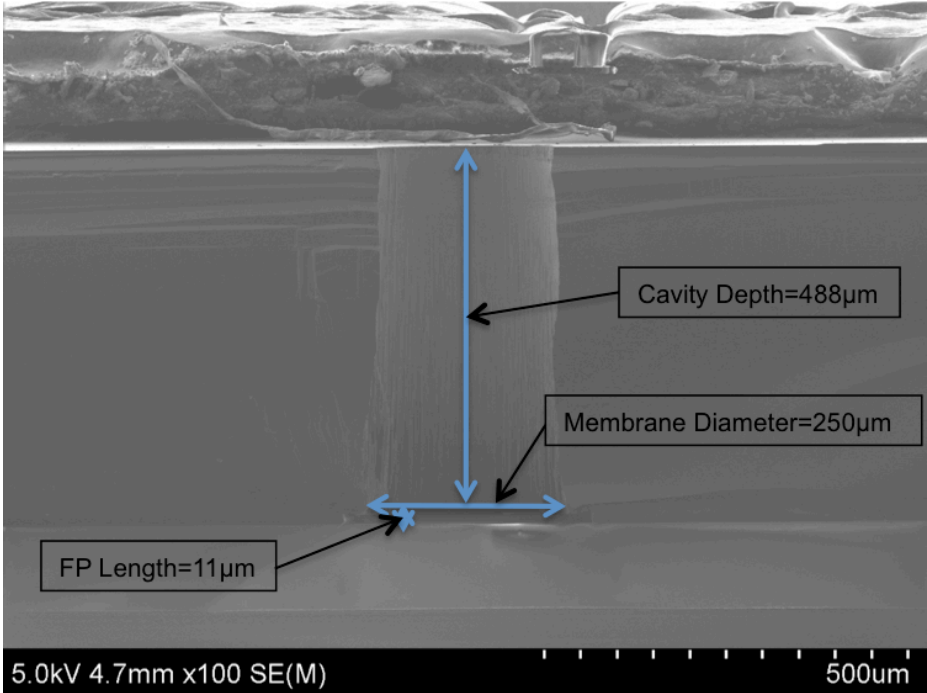


Figure 3.5: Cross-section SEM image of the MEMS chip. SEM holding carbon tape seen on top of the image.

### **3.5.- Thin-film materials electrochemical stack.**

#### **3.5.1.- Materials stack deposition using titanium nitride as a current collector.**

After the MEMS chip is finished, prior to its assembly into the battery package, an electrochemical stack should be deposited on it. This electrochemical stack consists of a current collector, to give a conduction path for the electrons, and an active material, that participates in the battery electrochemical reactions.

The first approach was to use atomic layer deposition (ALD) [49] to deposit titanium nitride (TiN) as a current collector and chemical barrier that avoids lithium insertion in the underlying silicon. ALD demonstrates near perfect conformability, fulfilling the need to reach the entire surface inside the electrochemical cavity of the MEMS chip. Using a Beneq TFS-500 ALD machine, a 100nm layer of titanium nitride was deposited.

The deposited active material was silicon. Using an AJA ATC-series Sputtering unit, 1 $\mu$ m of silicon was sputtered [50] on top of titanium nitride using a 200W RF power source, at a rate of 60nm/min. After the silicon sputtering the resistance of the titanium nitride underneath it increased, giving an 80 $\Omega$  reading between the chip contacts. This was most probably due to an erosive effect of the argon plasma during the sputtering. On figure 3.6 the chip with the deposited current collector and active materials, along the resistance measuring points is shown.

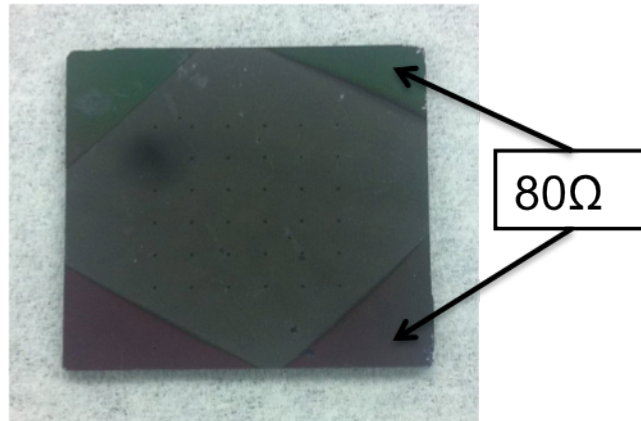


Figure 3.6: MEMS chip with titanium nitride (colored corners) and silicon layers deposited.

The arrows indicate the resistance measuring points.

The electrochemical test data from this stack (see chapter 4.1.1) did not give satisfactory results, as high contact resistance makes any electrochemical measurement inaccurate [1]. A new stack was designed and fabricated.

### **3.5.2.- Stack deposition using Cu as a current collector.**

Having had problems with the electrical conductivity of titanium nitride, copper [51] was the most promising alternative material to use. Most commercial Li-ion batteries [46] use copper as the anode current collector. Copper is an excellent conductor of electricity and it does not react with lithium in the desired voltage range of 0.01V to 3.5V [52]. So this choice was very appropriate for this work.

Before the stack deposition, and since copper does not prevent the bulk silicon of the chip of reacting with lithium, a 250nm layer of silicon oxide was deposited using plasma enhanced chemical vapor deposition technique (PECVD). This deposition was done using an Oxford Instruments Plasmalab 100 machine with a 70nm/min deposition rate. This corresponds to step (m) of the fabrication process flow.

For the current collector a sandwich structure of 20nm of titanium, 250nm of copper and 5nm of titanium was used. The first titanium layer serves as an adhesion promoter, for copper, the last titanium layer is used to passivize the copper [53] and avoid oxidation. The AJA Sputtering unit was used to deposit copper and titanium using a DC 200W power source and a rate of 16nm/min (copper) and 5nm/min (titanium). Available methods to deposit the above-mentioned metals are thermal evaporation and sputtering, but only sputtering provides the needed silicon thin-film, so sputtering was the chosen technique.

On top of these metals, 1 $\mu$ m of silicon was sputtered using the same process mentioned in section 3.5.1. A SEM picture of a process test sample stack with only 300 $\mu$ m of silicon, layer structure is shown in figure 3.7. A schematic of the actual thin-film stack is depicted in figure 3.8. Simple two-contact resistance measurements on the metal stack were performed using a multimeter, resulting in values below 0.1 $\Omega$ .

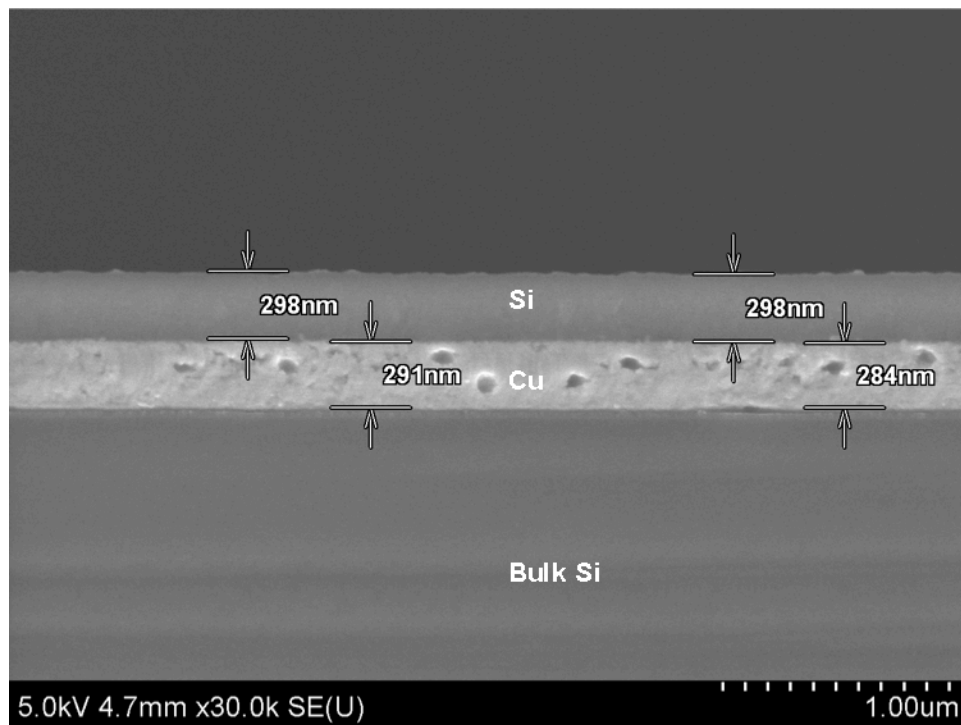


Figure 3.7: Ti-Cu-Ti-Si on bulk Silicon electrochemical stack.

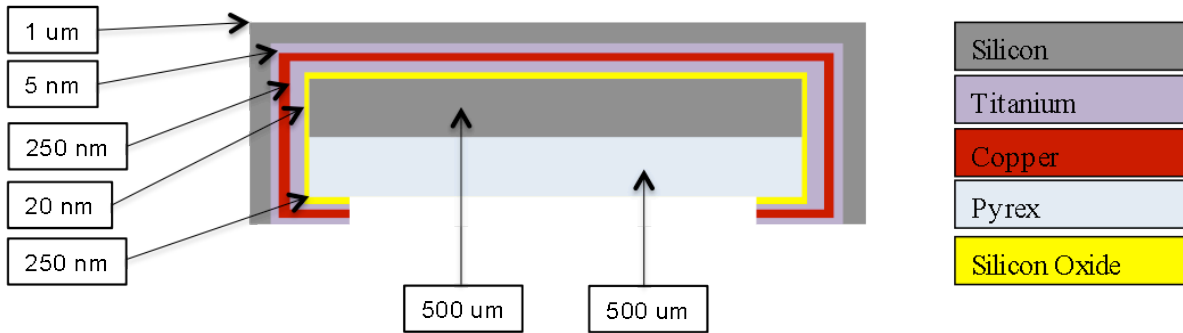


Figure 3.8: Schematic of materials thin-film stack.

### 3.5.3.- Electrochemical cavity underetching and thin-film conformal covering.

During the fabrication process, and due to the design of the process flow, during step (j) (see section 3.2) it was very difficult to obtain a perfectly straight sidewall from top to bottom, presumably because of the accumulation of passivation film in the bottom of the pit [54]. In most cases some over etching was observed, giving an electrochemical cavity to membrane interface that looks like the SEM image in figure 3.9a. This non-desired feature negatively affected the coverage of the thin-film materials deposited using sputtering techniques. On the other hand, when reducing the time of the DRIE process a cavity with incomplete etching was obtained.

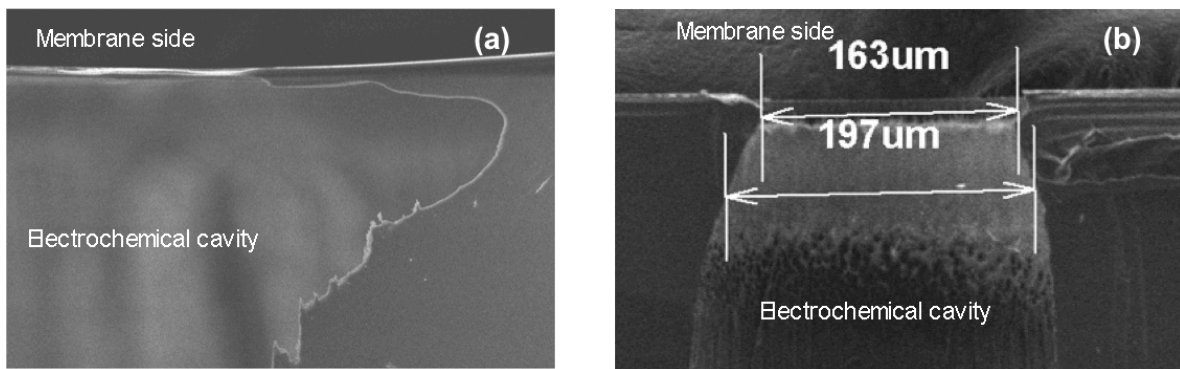


Figure 3.9: SEM images of different DRIE etchings. (a) over etched, (b) under etched.

The shape of the sidewall obtained with this under etching assisted in that the deposited materials reached all the desired surfaces to obtain a continuous thin-film and hence electrical conductivity and electrochemical activity on the intended membrane surfaces. Figure 3.9b shows an SEM image of the irregular shape obtained with under etching.

## **4.- Experimental testing.**

### **4.1.- Pneumatic Testing and characterization of the MEMS Fabry-Perot chip.**

#### **4.1.1.- Test setup and methodology.**

Once the MEMS chip was fabricated it was important to confirm the operation of the Fabry-Perot interferometer. In order to do that, a pneumatic test was conceived where pressurized air is introduced on the electrochemical cavity of the MEMS chip and the membrane is deflected. It is to be noted that this test was conceived to confirm the operation of the MEMS chip Fabry-Perot transducer, and precisely determining parameters of the design is beyond the scope of this experiment.

During the test varying air pressure was applied to the tested device, as the pressure was measured with a pressure sensor (Omega<sup>tm</sup> PX138 series pressure transducer), pictures of the changing fringes of the Fabry-Perot interferometer were taken. A comparative analysis of those pictures with the associated pressure data was used to obtain a confirmation of the operation of the device and the spring constant of the membrane. The experimental setup for this test is depicted in figure 4.1.

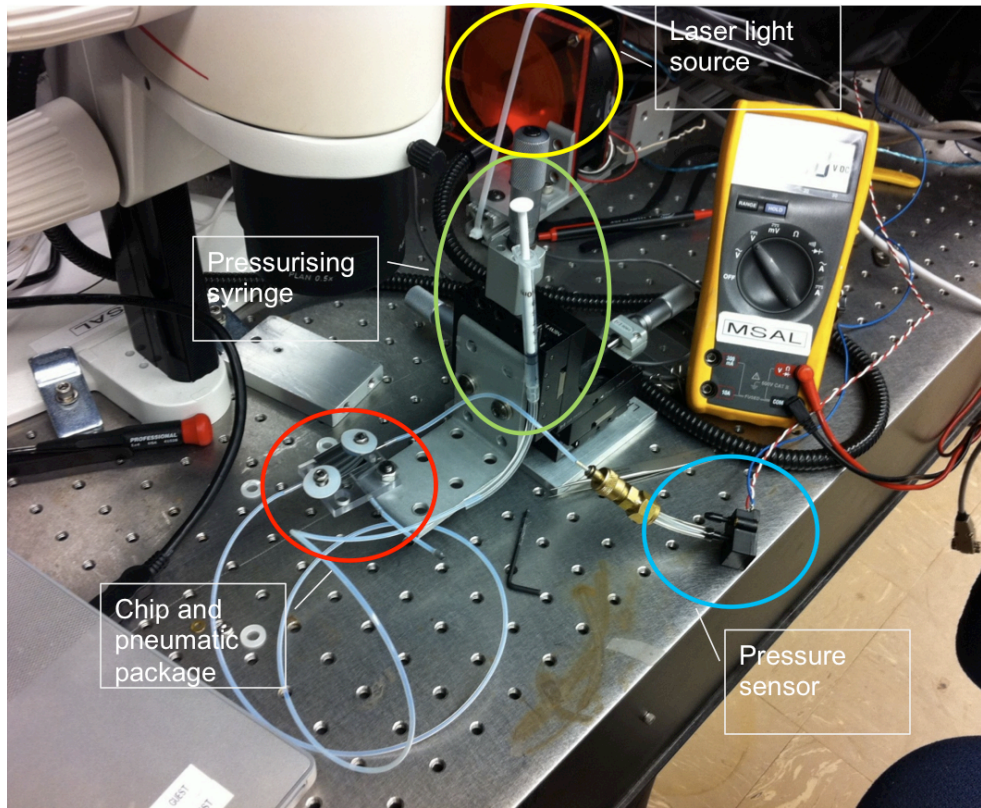


Figure 4.1: Pneumatic test setup.

With this setup it was possible to pneumatically characterize the spring constant of a 300 $\mu\text{m}$  membrane, and hence have a confirmation that the MEMS chip was able to monitor mechanical stress.

#### 4.1.2.- Physical principles applied.

Using the formula presented in equation (1.5), with  $n=1$  (due to the vacuum inside the Fabry-Perot cavity produced by the anodic bonding),  $\lambda=660$  nm (red laser) and measuring the new Fabry-Perot fringes that were created as pressure was applied (which is equivalent to an increasing  $m$ ) the distance between the membrane and Pyrex,  $l$  could be calculated. Knowing the air pressure that was measured using a pressure sensor and the



surface area of the membrane, the force  $F$  was obtained. Hooke's law states that  $F=kx$  (in this case  $x=l$ ), hence obtaining the spring constant  $k$ .

#### 4.1.3.- Pneumatic test results.

Using the setup shown in figure 4.1, increased pressure was applied on a 300 $\mu$ m diameter Fabry-Perot device.

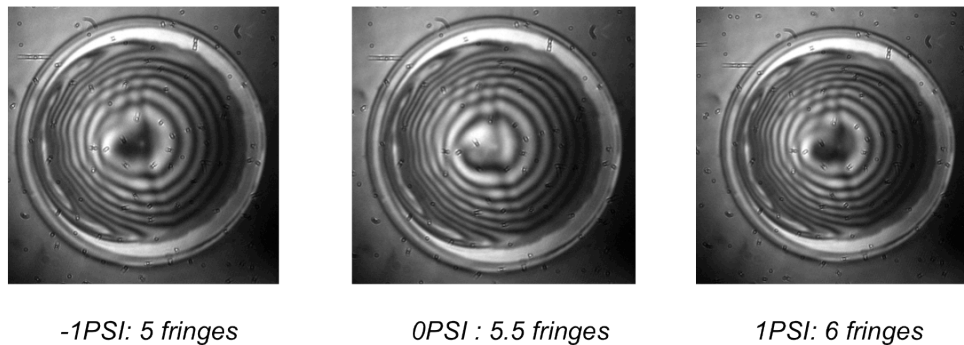


Figure 4.2: Fabry-Perot fringe change at three different pressures.

From figure 4.2, the net fringe change for a 2PSI pressure increase was of 1 fringe, which corresponds to 330nm change in the distance  $l$ . The 2PSI pressure corresponds to a force of 0.487mN on the 300 $\mu$ m diameter membrane, resulting in a spring constant of  $k=2951.5\text{N/m}$ . Although not fundamental for the rest of this work, this obtained parameter is important for future generations of the platform where quantitative data will be measured.

This test provided a confirmation of the Fabry-Perot interferometer operation and the capability of measuring air pressure. Although it is not the primary use of the MEMS chip, it provides with a confirmation of the operation of the device.

## **4.2.- Electrochemical testing of the thin-film electrochemical stacks using dummy devices.**

To obtain reference electrochemical data to which compare the experiments using the full platform including the MEMS chip, first some experiments using more reliable batteries based on stainless steel discs and dummy chips had to be performed.

Electrochemical performance of silicon electrodes was first evaluated using 200nm thick silicon thin-film deposited on stainless steel discs, and assembled into standard coin cells. Then to validate the results of a complete experiment using the MEMS chip, first the assessment of the thin film electrochemical stacks on chips was needed. To do this, dummy chips made with the same materials as the MEMS chips and having the same dimensions, but no cavities of any kind (planar configuration), were applied with the thin film stacks and assembled into standard and custom-modified coin cells as well as the first and second generation package.

### **4.2.1.- Silicon thin-film on stainless steel discs.**

For this experiment 200nm of silicon was sputtered on stainless steel discs, using the same technique described in section 3.5.2, and assembled into standard coin cells using metallic lithium as counter and reference electrodes, Celgard<sup>tm</sup> separator film and lithium hexafluorophosphate (LiPF<sub>6</sub>) in ethylene carbonate/diethyl carbonate electrolyte [55], which are the standard materials used in Li-ion battery experiments. The battery was cycled using the Arbin Instruments battery tester at a constant current density of 1A/g between 0.01V and 1.5V for 10 cycles. The results of this experiment show a shape of discharge/charge curves with plateaus at 0.2V indicating lithium insertion into silicon, that is in a good agreement with what is reported for silicon in the literature [56], the capacity of

the first discharge cycle is higher than the subsequent cycles due to the formation of solid-electrolyte interphase (SEI). Figure 4.3a depicts this. After the first discharge cycle the capacity of silicon stabilizes at around 2500mAh/g and doesn't show significant fading throughout the rest of the test (figure 4.3b). Since the purpose of this work was not necessarily to improve electrochemical performance of silicon electrodes, the test was stopped after 10 cycles. Since the capacity of the electrodes at a constant current rate is directly proportional to time required to finish a particular cycle, later in this work, specific capacity of the electrodes was not calculated, but evaluated by measuring the time of discharge/charge cycles.

This result provides a model to which further compare the electrochemical data obtained on the rest of the experiments in this work. As such it was repeated several times always obtaining congruent data.

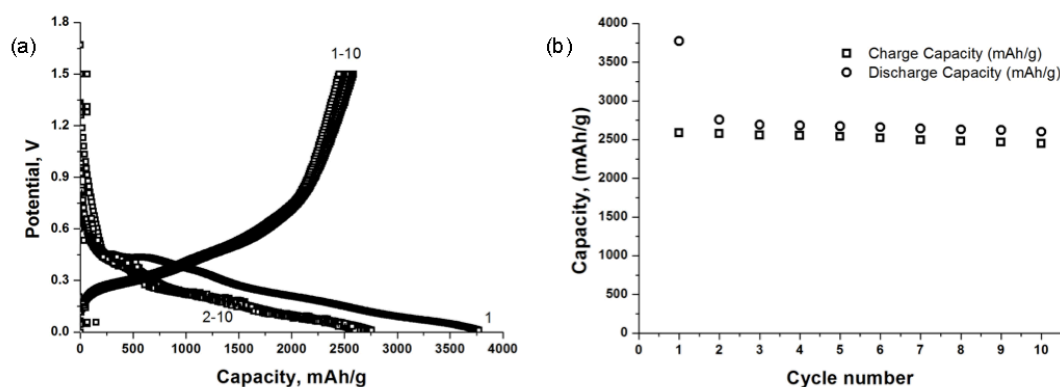


Figure 4.3: Electrochemical performance of 200nm silicon thin-film on stainless steel disc, (a) discharge/charge curves, (b) capacity versus cycle number.

#### 4.2.2.- TiN-Si Stack in a standard coin cell.

In a further step to generate electrochemical data with elements that resemble physically the ones used on the measurement platform, a new experience was performed. Electrodes for this experiment were prepared on 1 cm by 1 cm silicon chips. A thin-film stack was deposited on one side of the chip as described in section 3.5.1 with the addition of a second deposition of titanium nitride on the backside of the chip to make contact with the coin cell case.

The chip was assembled in a standard coin cell, using the same elements as in section 4.2.1. The battery was cycled using the Arbin Instruments battery tester at a constant current of  $40\mu\text{A}$  between 0.01V and 1.5V for 10 cycles. Electrochemical data of the results is shown in figure 4.4 where in less than 10 cycles the thin-film stack degraded giving an increased capacity [57] (figure 4.4b). This increased capacity is a sign of bad performance of the battery. Four experiments were conducted using this configuration and similar results were obtained.

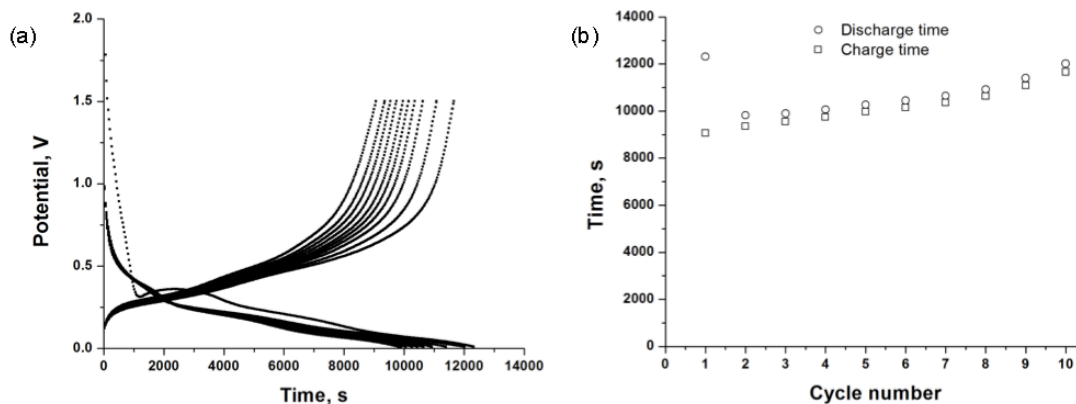


Figure 4.4 : Electrochemical performance of  $1\mu\text{m}$  silicon thin-film silicon chip with a titanium nitride current collector on a coin cell, (a) discharge/charge curves, (b) time versus cycle number.

The origin of this capacity increase seems to come from the poor mechanical stability of the titanium nitride and the possibility that the bulk silicon of the chip was lithiated as the titanium nitride deteriorated with cycling. When testing the capabilities of a certain electrode, the sputtered thin-film silicon in this case, it is important to assure that only the desired electrode material is participating in the electrochemical reaction to be characterized. This is not the case that was observed in this experiment.

#### **4.2.3.- TiN-Si Stack in first and second generation custom electrochemical package.**

The MEMS sensing chip measured originally 2cm by 2cm, hence experiments with the different thin-film electrochemical stacks using this format needed to be performed. The first and second-generation packages produced unsatisfying experimental results. During the development of these generations, the TiN-Si thin-film stack was used, so the experiment was done using a 2cm by 2cm dummy chip made with the same materials as the MEMS chip and deposited with a thin-film stack as described in section 3.5.1. This dummy chip was assembled into a first (or second) generation experimental package as shown in section 2.3.2. The same electrolyte, separator and metallic lithium as in section 4.2.1 were used.

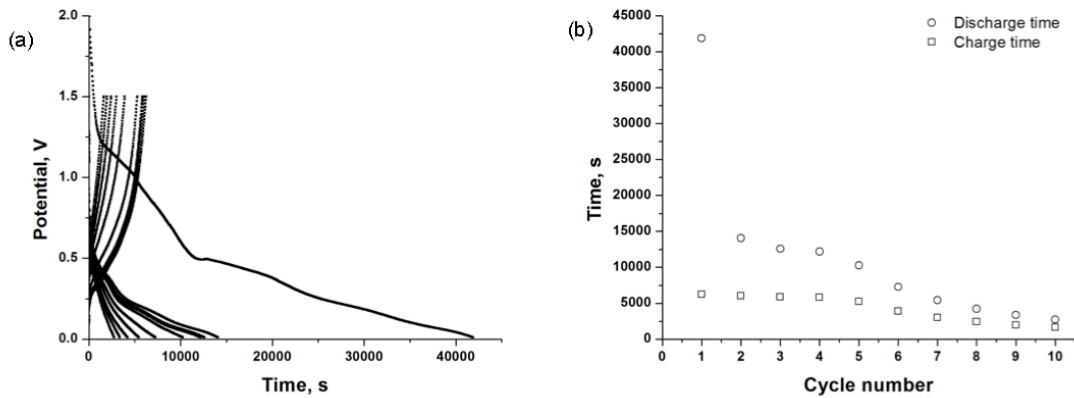


Figure 4.5: Electrochemical performance of 1µm silicon thin-film on a silicon chip with a titanium nitride current collector on custom first generation package, (a) discharge/charge curves, (b) time versus cycle number.

The Arbin Instruments battery tester was used to deliver a discharge/charge current of 31µA in a 0.01V to 1.5V voltage range, for 10 cycles. Figure 4.4 shows the electrochemical data of the test, where a rapid decrease in the capacity (depicted as time of cycle on figure 4.5b) of the battery is shown as it is cycled. Although decrease in capacity is unavoidable, the rapid decrease (one third of the original capacity in less than 10 cycles) observed in the experiment is a sign of bad performance. Also the first 6 cycles show a disparity between charge and discharge above of 50%, this means that a lot of energy injected onto the charge of the battery is not extracted back when discharging, this energy might have gone into undesired processes. This charge/discharge disparity is known as bad coulombic efficiency.

Many inconclusive results were obtained with six other experiments that used this thin-film stack and the first/second generation of package, prompting the decision to design

a new package, for a more streamlined and reliable assembly; and to use the Ti-Cu-Ti-Si thin-film stack, to avoid problems like the ones observed in section 4.2.2.

#### **4.2.4.- Ti-Cu-Ti-Si Stack in custom coin cell / third generation package.**

The third generation package is based on a custom-modified coin cell, where a chip with backside copper electrodes is bonded using a conductive-glue copper adhesive tape. The thin film stack deposition is presented in the section 3.5.2 and the package assembly in section 2.3.3. The same electrolyte, separator and metallic lithium as in section 4.2.1 were used.

The assembled battery was tested for more than 40 cycles at a  $40\mu\text{A}$  discharge/charge current in a 0.1V to 1V range, maintaining its capacity almost unaltered. As fully explained later in this thesis, a lower voltage range provides a “safe” operation of the battery and also provides enough voltage swing to observe the desired electrochemical process. Figure 4.6 depicts good electrochemical performance during 3 cycles. In figure 4.7 the cycling data shows similar results to those obtained in the literature [58], where a longer first discharge is due to the solid-electrolyte interface (SEI) formation [59], the plateaus formed at 0.2V show lithium intercalation into the silicon, and the same size charge and discharge areas mean that a good coulombic efficiency [57] is obtained. Although this experiment was run for a longer cycle period, only 3 cycles are shown in figures 4.6 and 4.7 to allow the observation of the electrochemical processes cited above and to later compare the reference battery results with the complete platform results.

Having repeated this experiment more than 10 times, always obtaining very similar results as the ones shown on figure 4.7, it was decided that this thin-film stack and packaging scheme a good candidate to be used with the MEMS chip experiments.

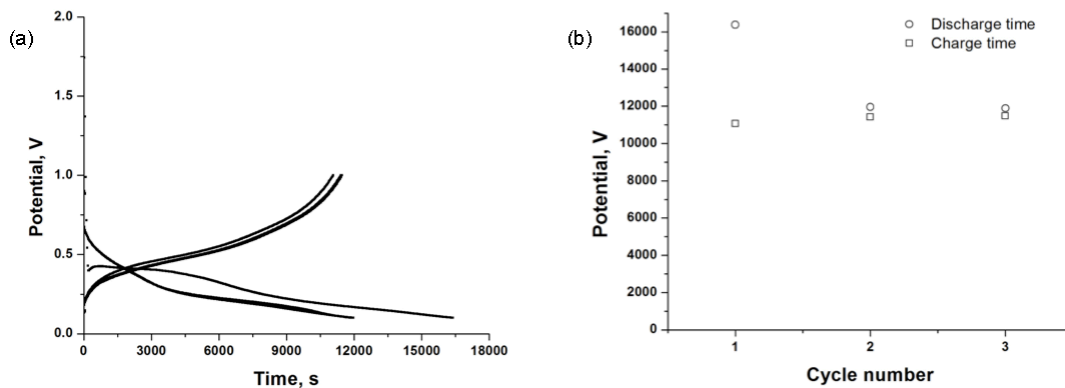


Figure 4.6: Electrochemical performance of 1  $\mu\text{m}$  silicon thin-film silicon chip with a Ti-Cu-Ti current collector on custom-modified coin cell, (a) discharge/charge curves, (b) time versus cycle number. Only first three cycles are shown.

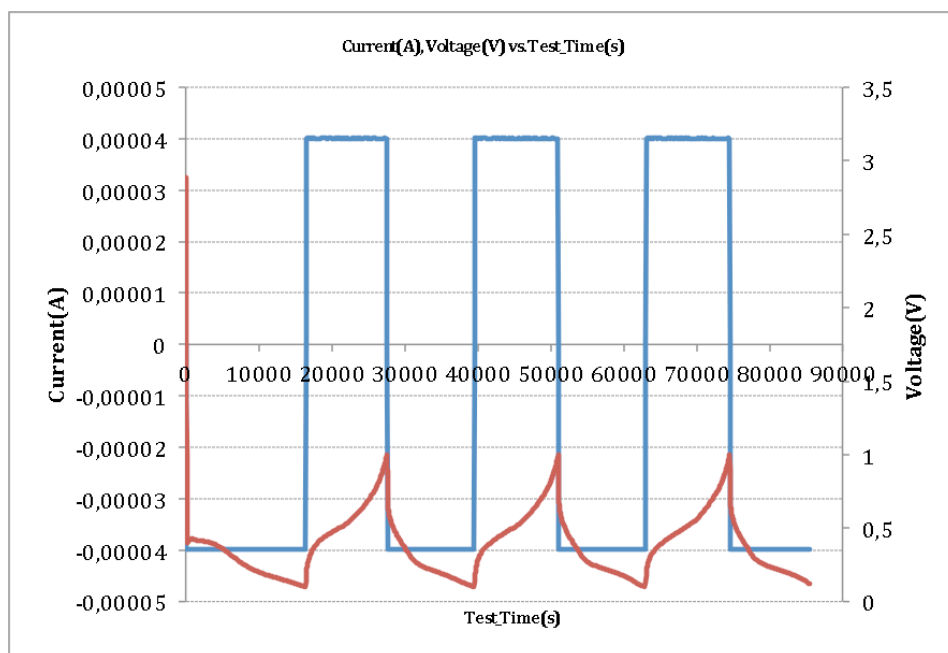


Figure 4.7: Ti-Cu-Ti-Si thin-film stack tested on custom modified coin cell. Only 3 of more than 40 cycles are shown for simplicity. Blue line is current, red is voltage.



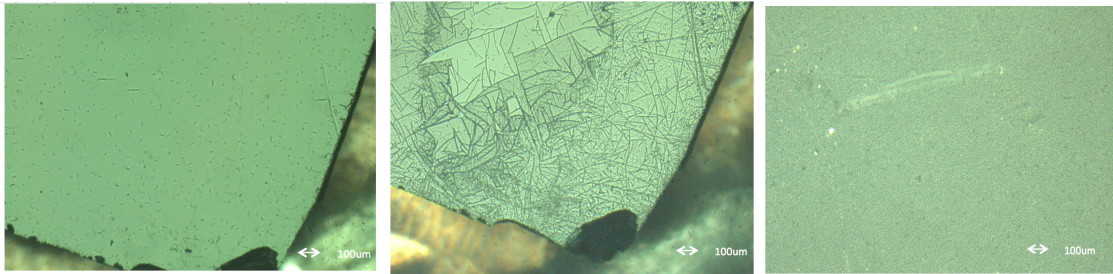


Figure 4.8: Optical microscope images of Ti-Cu-Ti-Si thin-film stack. On the left a pristine electrode with no cycling, center: the same electrode after 1 cycle, right: an electrode cycled 3 times.

Post-cycling analysis was performed on several of these experiments to observe the effect of the lithium insertion/extraction on the sputtered silicon thin film. The images taken using an optical microscope can be seen in figure 4.8. This image study served to confirm that although cracking is seen on the silicon thin-film, no delamination occurs in the 1V to 0.1V voltage range. This is confirmed by electrochemical data that show no significant variation (figure 4.7).

### **4.3.- *In situ* testing of electrochemically reaction-induced volume change in silicon.**

#### **4.3.1.- Test using first and second generation package and TiN-Si thin film stack.**

As seen in chapter 2 and at the beginning of chapter 4, there has been an evolution in the experimental package and the thin-film stack. Presented here are the experiments involving a first generation package and TiN-Si thin-film stack.

##### **4.3.1.1.- Experimental setup and parameters.**

Using a MEMS chip with the TiN-Si thin-film stack and a first generation package, a complete experimental setup was assembled with the elements introduced in section 2.4. Such setup, minus the battery testing machine and image capturing computer, can be seen in figure 4.9.

The test was done at a constant current of  $80\mu\text{A}$ , with a voltage range of 0.01V to 1.5V . Simultaneously the fringe images of the Fabry-Perot device were captured at a rate of 1 image per minute. This experiment did not provide reversible correlated fringe change with the charge discharge cycles and it only worked for a single discharge, making the obtained data unreliable. Although there was some reaction of the Fabry-Perot device to the electrochemical process inside the battery, it was not possible to validate this experiment due to the failure of the battery after the first discharge.

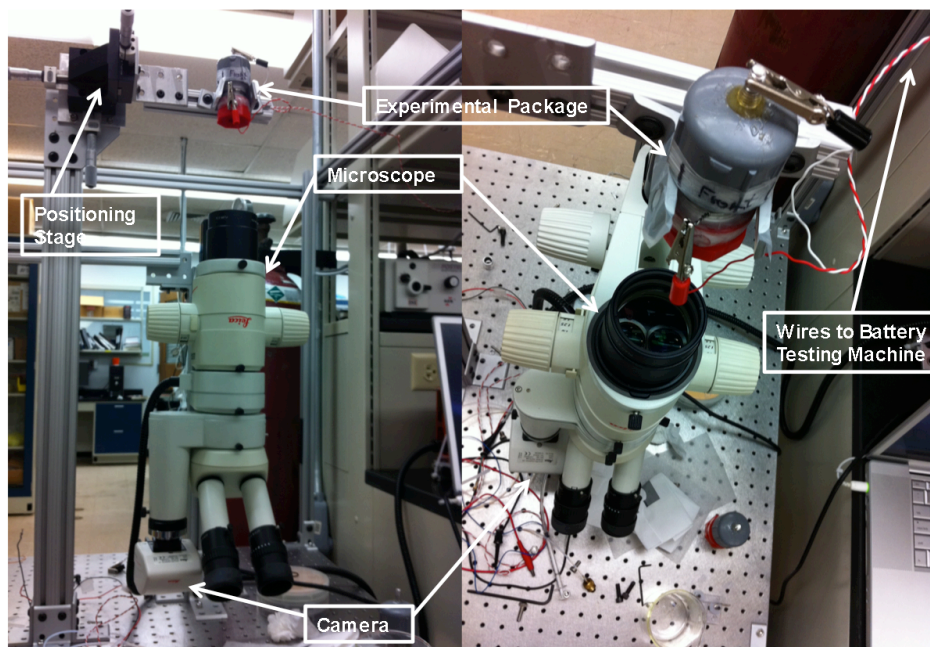


Figure 4.9: Experimental setup using first generation package. TiN-Si MEMS chip is inside the package.

Experiments using the second generation package were analogous to the ones using the first generation package and proved unsuccessful due to the impossibility to solve the sealing problems that the design presented.

#### **4.3.2.- Test using custom coin cell / third generation package and Ti-Cu-Ti-Si thin film stack.**

Having obtained very reliable electrochemical results using the customized coin cell (third generation package) and the Ti-Cu-Ti-Si thin-film stack, several experiments using these elements were done.

##### **4.3.2.1.- Experimental setup and parameters.**

These experiments used the experimental setup defined in section 2.4, the third generation experimental package and the thin-film stack presented in section 3.5.2. In order

to accommodate the custom-modified coin cell, a battery holder was added to the setup. The setup, minus the Arbin Instruments battery-testing machine, is depicted in figure 4.10.

Unless otherwise indicated, all experiments in this section were performed using a “safe” discharge/charge scheme of 40uA with a voltage range of 0.1V to 1V. This voltage range of 0.1V to 1V is considered safe because to fully insert lithium ions into silicon a 0.01V discharge voltage is needed, and to fully extract requires above 1.2V [41]. Hence this limited voltage range process results in a partial expansion/contraction of the active materials, which may prevent the experiment to fail prematurely.

Monochrome images of the fringe changes were captured and stored once per minute, which is fast enough for the purpose of this experiment, because each discharge or charge cycle may take from four to eight hours.

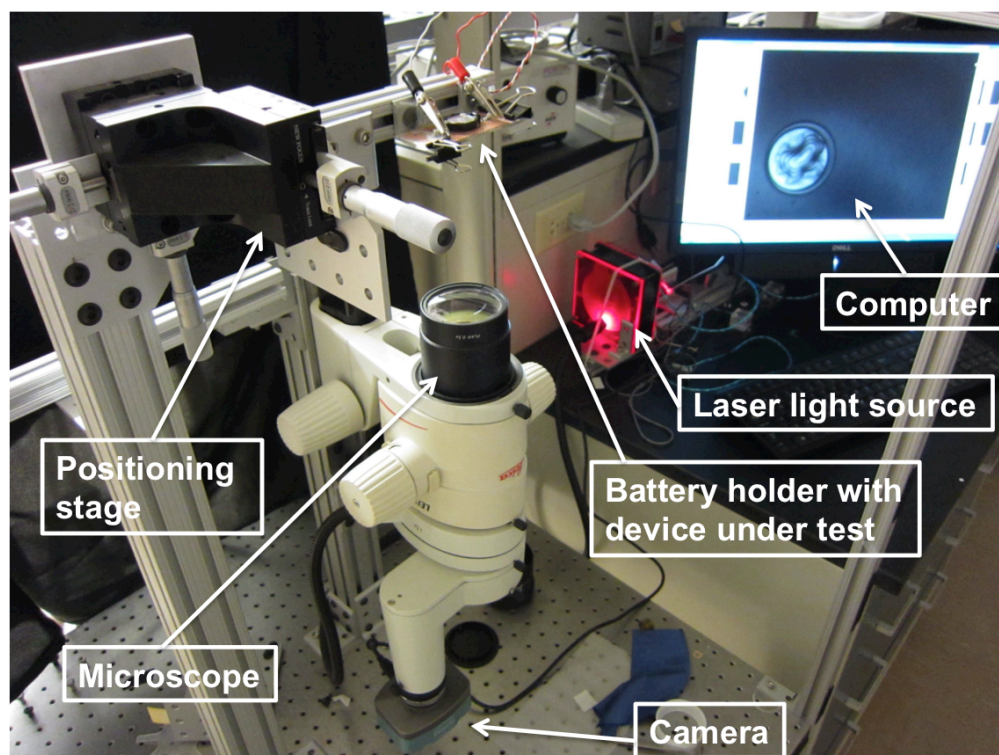


Figure 4.10: complete experimental setup with third generation package and battery holder.

#### 4.3.2.2.- First experiment.

A MEMS chip with 200 $\mu$ m diameter membranes was used for this experiment. The selection of the MEMS chip was done on the availability of fabricated chips and the optical microscope observation of the membrane quality. Using all the parameters defined in the previous section, the battery was cycled for 20 cycles obtaining reversible Fabry-Perot fringe changes as the active silicon thin film expanded and contracted while being discharged and charged respectively. The first fringe movement was observed at 0.4V that coincides to what Sethuraman's [41] work reports; figure 4.11 shows the fringe expansion.

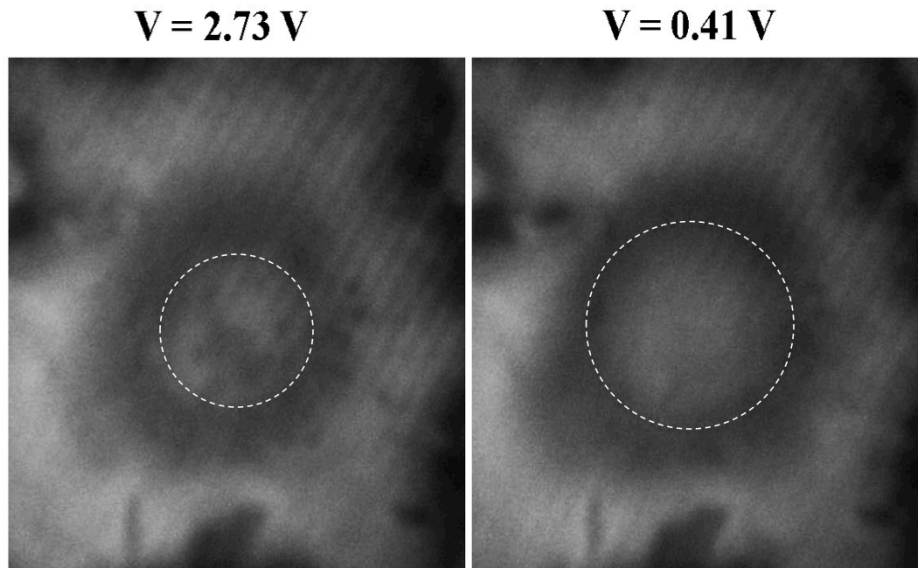


Figure 4.11: Fringe expansion in Fabry-Perot device. Voltages correspond to open circuit (2.73v) and 0.4V discharge point. White dotted lines inserted for better interpretation.

The discharge/charge electrochemical data of this experiment looks very similar to figure 4.7 but for a better representation, a graph that includes a single discharge and charge cycle superimposed and correlated with pictures showing the Fabry-Perot fringe change was made (see Figure 4.12). Due to a fabrication defect, this device suffered “cloudiness”

in the optical path. The cloudiness was possibly caused by the crack formation in the silicon nitride membranes, which allowed electrolyte leakage inside Fabry-Perot cavity. Evaporation of the electrolyte solvent results in solidification of the dissolved lithium salt, forming a white precipitate, which was observed in this experiment. Also, irregular shape of the membrane observed in figure 4.11 is due to the etching artifacts discussed in section 3.5.3. Although it is difficult to observe the fringe changes with a naked eye in the graph, time-lapse videos show this very clearly (for a video of this experiment refer to Appendix C).

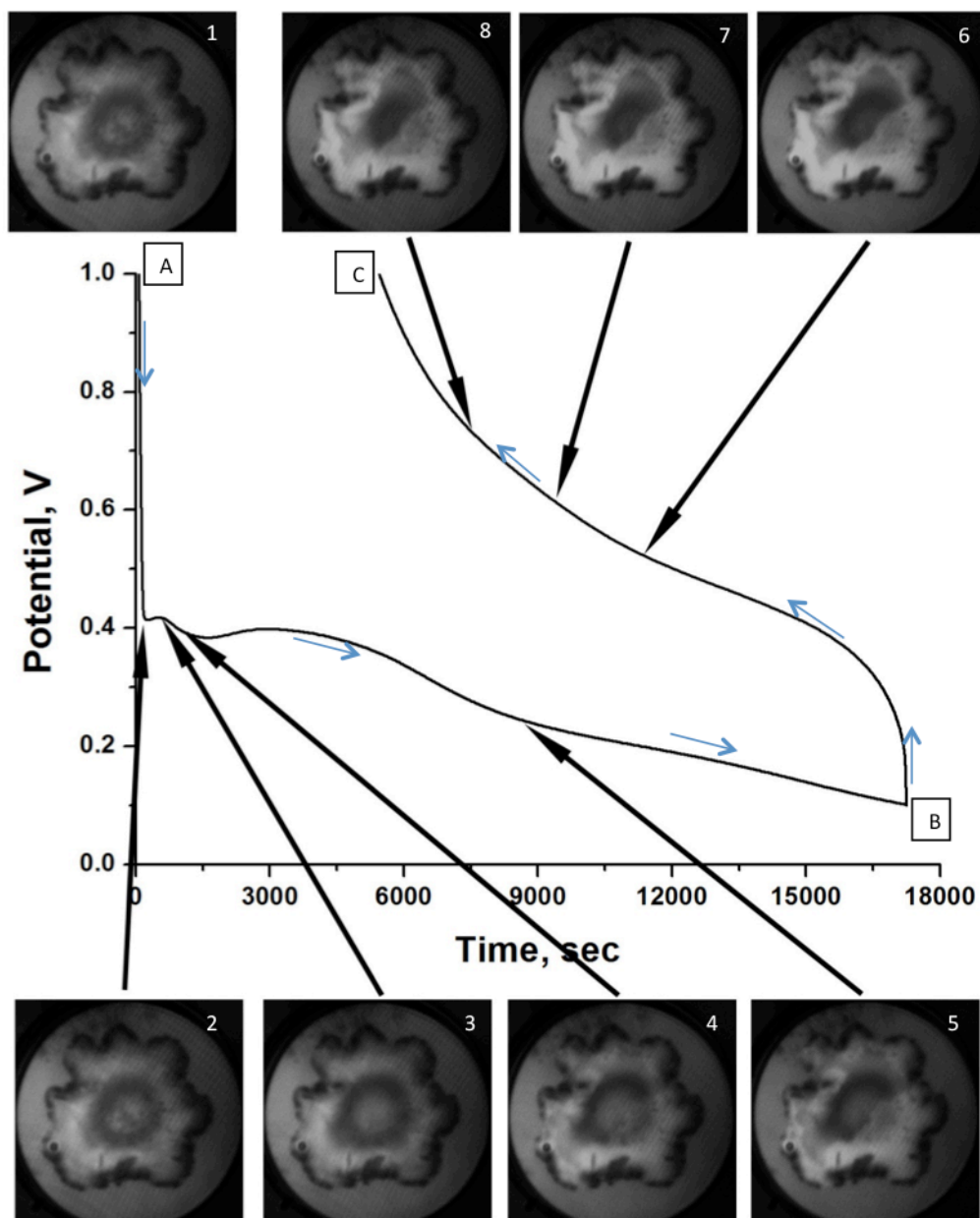


Figure 4.12: First discharge/charge cycle of the first experiment battery made using a 200µm diameter membrane MEMS chip. A to B is discharge, B to C is charge.

Closely correlated images of fringe changes with voltage were obtained during all the cycles of this experiment, no other parameter was changed during it, giving a firm idea

that the MEMS chip sensing device worked as designed. Having confirmed a successful operation of the MEMS chip, the electrochemical package, the setup and the testing parameters; two more experiments were done to validate the platform.

For more detailed viewing of the Fabry-Perot fringe images please see Appendix D.

#### **4.3.2.3.- Second experiment.**

Reiteration of the experiment was fundamental to confirm the operation of the platform and to obtain further data. A new experience was done, maintaining the same parameters and conditions as the first experiment a new battery was assembled using a 150 $\mu$ m diameter membrane MEMS chip, again selected on availability and membrane quality. The testing was also performed without any modification on the variables, resulting again in a reversible Fabry-Perot fringe pattern change correlated with the discharge and charge of the battery.

This experiment had again an electrochemical response extremely similar to what it is seen in figure 4.7. For the graph presented on figure 4.13, the third cycle of the battery was chosen; from the second cycle on, the discharge/charge times are symmetrical showing good coulombic efficiency and good graphical representation of the reversible fringe change in the Fabry-Perot device.



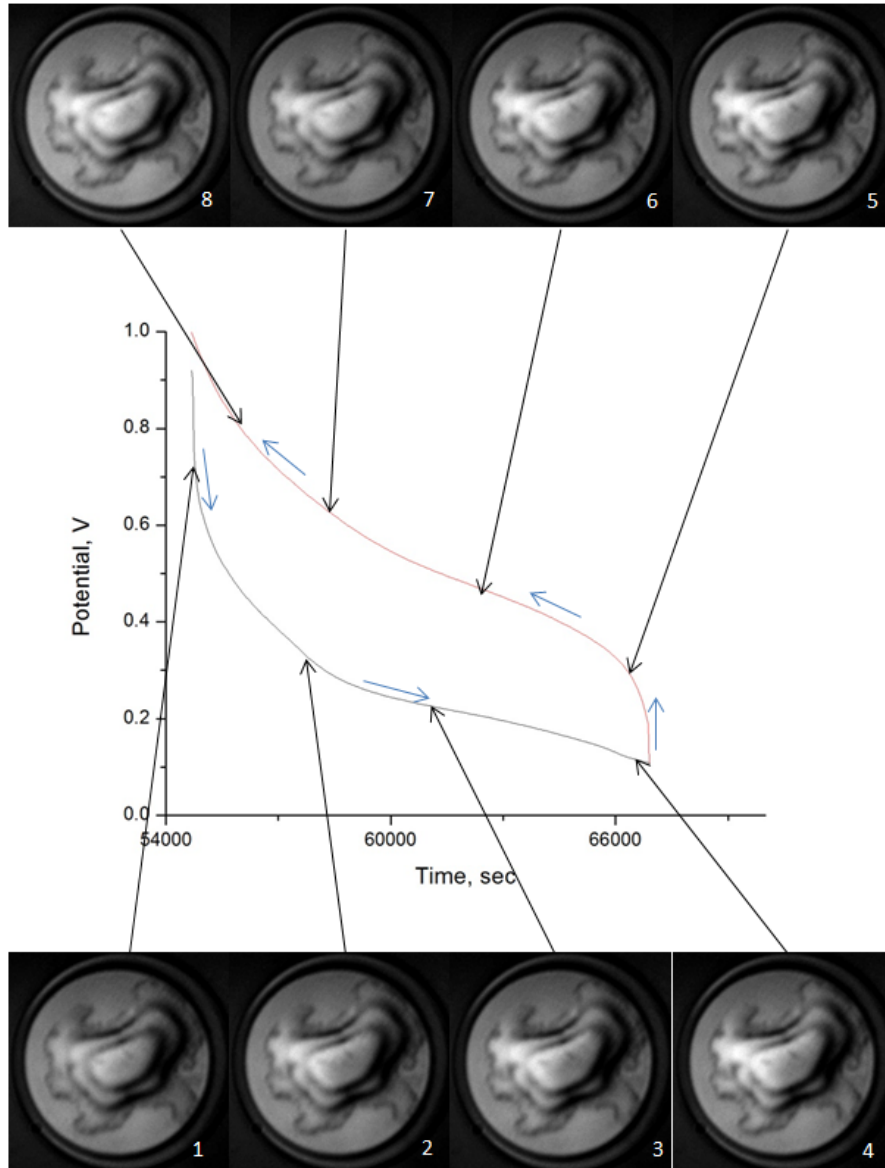


Figure 4.13: Third discharge/charge cycle of the second battery made using a 150 $\mu$ m diameter membrane MEMS chip. Grey is discharge, red is charge.

This device has a non-circular membrane due to a DRIE under etch on the step (j) of the fabrication process. Despite this defect, in the next chapter, a demonstration of how to obtain valid Fabry-Perot fringe change data from this device is presented. The Fabry-Perot fringe changes in this experiment can be better visualized in the video (see Appendix C).

#### 4.3.2.4.- Third experiment.

After confirming the correct operation of the platform with the two first experiments, on the third one electrochemical parameters were changed to see if the platform response followed what was expected from what is expected and described in the literature. In this final experiment, a MEMS chip containing a Fabry-Perot device with membranes of  $150\mu\text{m}$  of diameter was used. All parameters on the MEMS chip, experimental package and setup were maintained as in the previous experiments. Two different electrochemical discharge/charge tests were run on the same battery, the first one using the “safe” voltage range of 0.1V to 1V at  $40\mu\text{A}$  for 15 cycles, and a second one using a full lithium insertion [41] and extraction voltage range of 0.01V to 1.5V [60], also at  $40\mu\text{A}$  for 6 cycles. Using the larger voltage range a bigger expansion and contraction of the silicon thin film was expected [4] and hence a more pronounced Fabry-Perot fringe change should occur. Figure 4.14 shows a cycle on the 0.1V to 1V range. In figure 4.15 a Fabry-Perot fringe photograph of the larger voltage range test is depicted, showing a more pronounced change and an extra fringe. Chapter 5 contains detailed analysis on these tests. A video corresponding to 22 cycles of this experiment can be seen at a link found in Appendix C.

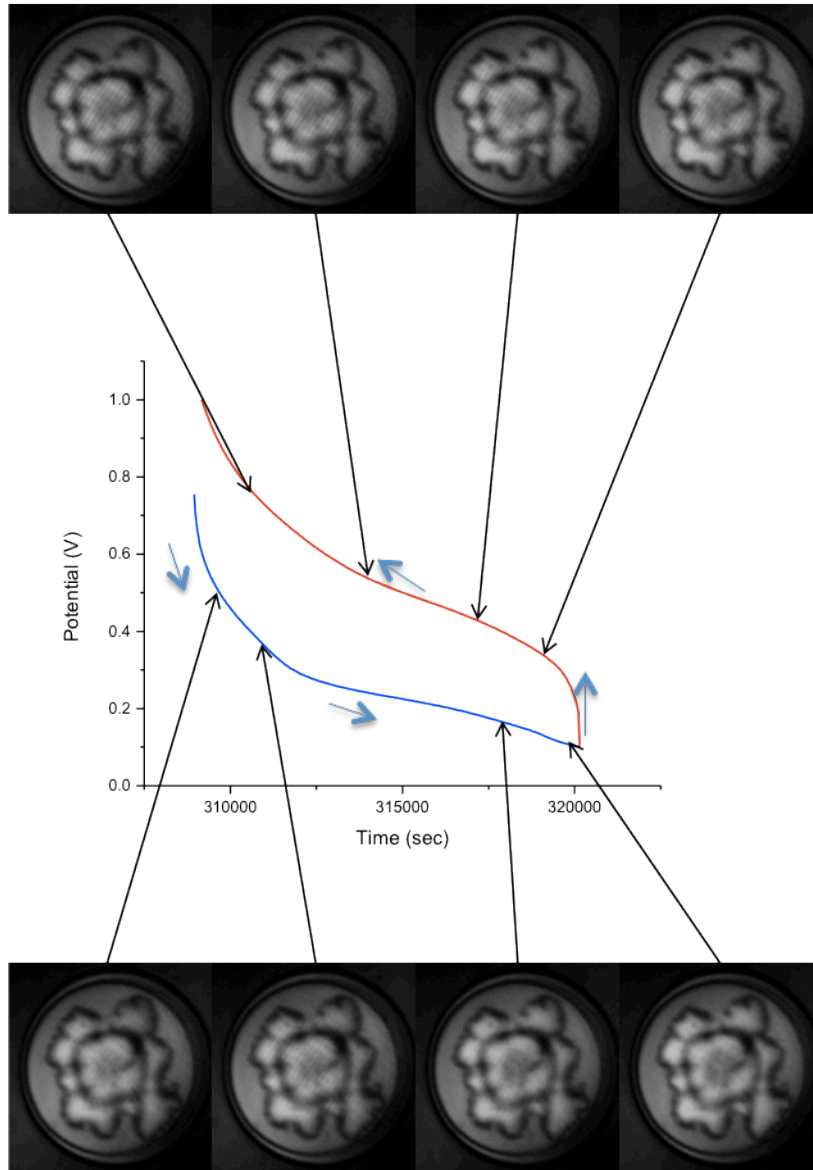


Figure 4.14: Fourteenth discharge/charge cycle of the third battery made using a 150 $\mu$ m diameter membrane MEMS chip. Voltage range: 0.1V to 1V. Blue is discharge, red is charge.

All cycles in both tests of this experiment showed reversible Fabry-Perot fringe changes correlated with the discharge/charge data, but the cycle chosen for figure 4.14 is

the most representative of the difference in Fabry-Perot fringe change between the smaller and larger voltage range tests.



Figure 4.15: Fabry-Perot fringe photograph of third battery made using a 150 $\mu$ m diameter membrane MEMS chip.

## **5.- Data analysis and discussion.**

### **5.1.- Analysis of the electrochemical data.**

Since the objective of this work is to correlate the mechanical stress of silicon when lithium is inserted and extracted using the MEMS chip, it is very important to analyze the different phases in the electrochemical behavior of a Li-ion half-cell with silicon as anode. To do this analysis the electrochemical data of section 4.2.4 is used.

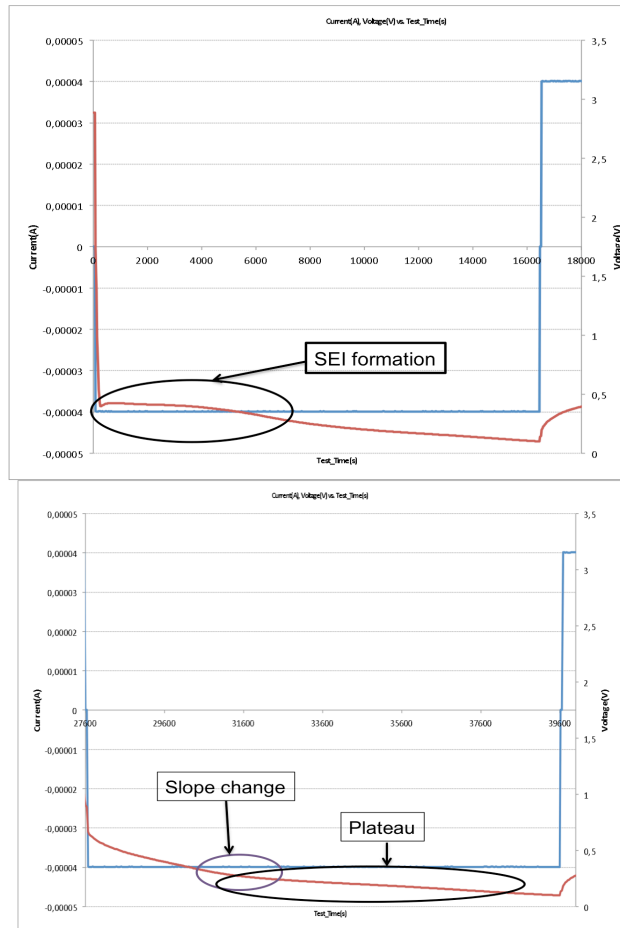


Figure 5.1: SEI formation zone during first discharge cycle (top), plateau at around 0.2V (bottom).

In figure 5.1 we can see two very important phases of the electrochemical process: (a) the SEI formation during the first discharge and (b) the plateau at around 0.2V when lithium is being inserted into silicon. The SEI formation in the first cycle is well described by Lee [61] and the plateau due to lithium insertion into silicon by Kulova [56]. The results presented above are in concordance to the ones in the literature and the data obtained in the first, second and third experiments, which were run with exactly the same parameters that are presented in section 4.3.2.1, exhibit similar characteristics.

## 5.2.- Secondary effects considerations.

To affirm that the correlated fringe pattern change was a consequence of the volume expansion/contraction of the active electrode material while lithium was inserted and extracted, secondary processes had to be analyzed to see if they were interfering in the measurement process.

To rule out power and thermal related actuation on the MEMS chip membranes, it is necessary to consider that the maximum fringe change occurs at voltages from 0.1V to 0.4V. At these voltages and since the current used for the main experiments is of  $40\mu\text{A}$ , the power ranges from  $4\mu\text{W}$  to  $16\mu\text{W}$ ; which are small values considering the size of the battery to produce any heating that may change its temperature with respect of the controlled ambient temperature. Furthermore highly reversible fringe changes have been observed, ruling out a power-related thermal actuation. Power is the same when charging and discharging and fringes shift in opposite directions.

Two electrochemical processes need also to be dismissed. First SEI formation is a complex electrochemical process where a layer that allows ion diffusion but blocks current conduction is formed on the surface of the electrode. The SEI formation occurs only on the first discharge cycle, so the effects on the fringe pattern change can be discarded on posterior cycles. Finally electrolytes based on  $\text{LiPF}_6$  and organic solvents are known to decompose when cycled at voltages above 2.5V [62], producing gas emissions. In this work the batteries were cycled at most at 1.5V, well below the decomposition voltage, eliminating this possibility.

### **5.3.- Analysis of correlated Fabry-Perot fringe changes and electrochemical data.**

The main objective of this work was fulfilled by the three experiments of section 4.3.2 where a correlated Fabry-Perot fringe change was repeatedly observed as the batteries containing the MEMS chip were discharged and charged during tens of cycles.

Furthermore some details of these experiments are worthwhile of being analyzed in the following sections.

#### **5.3.1.- Computer analysis of Fabry-Perot fringe data.**

As seen in section 4.3.2, it is very difficult to analyze the fringe changes just by looking at the images. Since this work will eventually become a precise tool to study the mechanical stress on active materials of Li-ion batteries, a computer-based method to analyze and obtain useful data from the Fabry-Perot fringe images is needed. A method of tracing the Fabry-Perot interference image changes by detecting the movement in the contrast produced by the fringes was proposed. In the work by O'Hora [63], where a complete automated Fabry-Perot fringe measuring method is developed, the use of a Cartesian to polar coordinates conversion is used as a first step. Dr. M. Gnerlich helped to develop a MATLAB code (see appendix E) to do this conversion.

Figure 5.2 exposes the process of this analysis, the main concept is to measure the intensity of the pixel elements along a radius of the Fabry-Perot fringe picture, the leftmost image of figure 5.2 shows the Cartesian representation and such a radius (in blue). Then the image is transformed into polar coordinates by scanning circularly the original picture, this can be seen on the center image, and finally on the left the plot of the intensities along a radius can be seen. In figure 5.3 a superimposed graph of several curves taken from the

images of the second experiment show a net displacement of the dark (low intensity) peaks, marked as region of interest. Trace numbers correspond to picture numbers in figure 4.13.

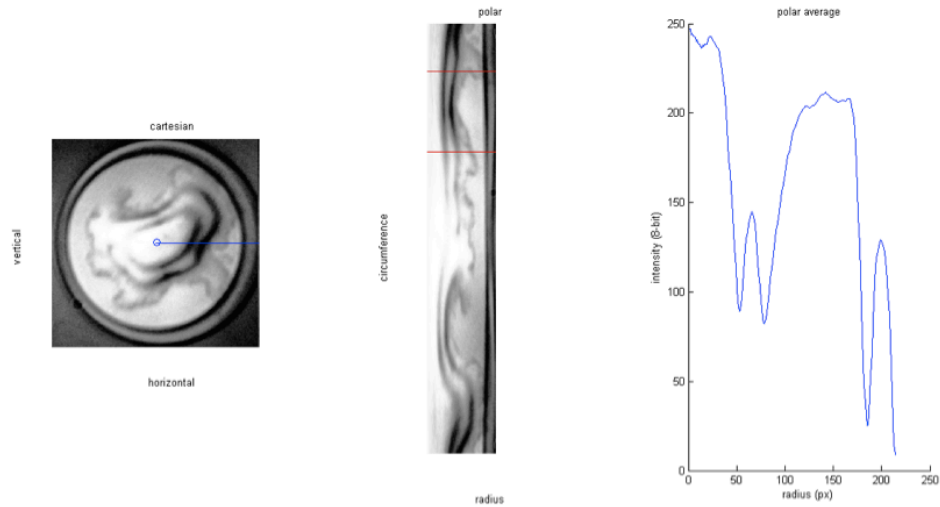


Figure 5.2: Cartesian to polar transform of Fabry-Perot fringe images. Cartesian representation (left), polar form (center), intensity plot along a radius (right).

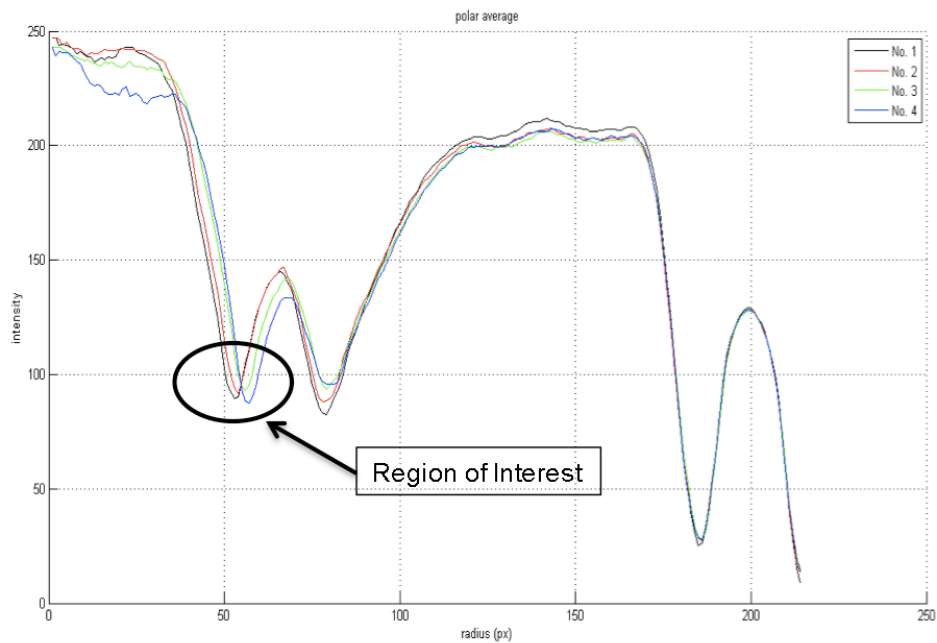


Figure 5.3: Intensity trace plot of 4 Fabry-Perot fringe images. Trace numbers correspond to Fabry-Perot fringe images of figure 4.12.



This type of analysis is useful to extract quantitative data from the Fabry-Perot fringe images. As seen on figure 5.3 it is easy to track the fringe displacement from the intensity plots, the “region of interest” shows a correlation between the graph peak displacement for the different plotted curves and the change of the Fabry-Perot fringe diameter. The displacement of this peak is used as basis for a future automated measurement of the platform results.

Having solved the problem of automatically interpreting the Fabry-Perot images, quantitative data of the volume expansion/contraction can be derived due to the correlation of the fringe patterns and the silicon nitride membrane flexing.

### **5.3.2.- Correspondence of electrochemical data.**

As mentioned in 4.2.4 and 4.3.2 once the custom electrochemical package and thin-film stack was definitively chosen, the numerous experiments using these elements gave electrochemical results that were very similar in all characteristics. Furthermore, a precise correspondence between the electrochemical results of a dummy chips using a standard coin cell packaging (section 4.2.4) and a MEMS chip using the custom-modified (third generation package) coin cell, was demonstrated. This correspondence is key to corroborate that the MEMS chip experiments produce results that are driven by the electrochemical process going on inside the battery. Figure 5.4 shows such a correspondence.

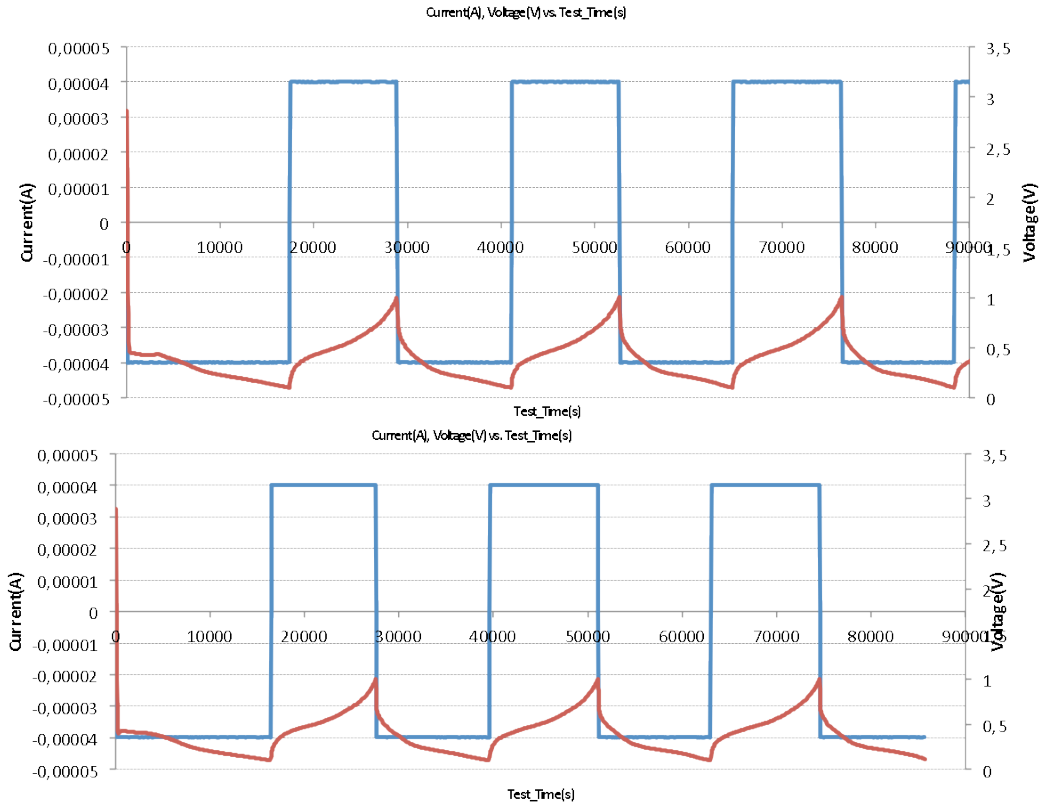


Figure 5.4: Electrochemical data of: MEMS chip on custom package (above), dummy chip on standard coin cell (below). Blue is current, red is voltage.

### 5.3.3.-Mechanical stress relaxation during discharge.

A particular behavior of the mechanical stress on the thin-film silicon while being inserted with lithium (discharge cycle) has been reported by Sethuraman [41]: after an initial peak of stress at around 0.4V, the film relaxes even though the voltage continues to drop and the lithium continues to be inserted in the silicon thin-film. Figure 5.5 show Sethuraman's results.

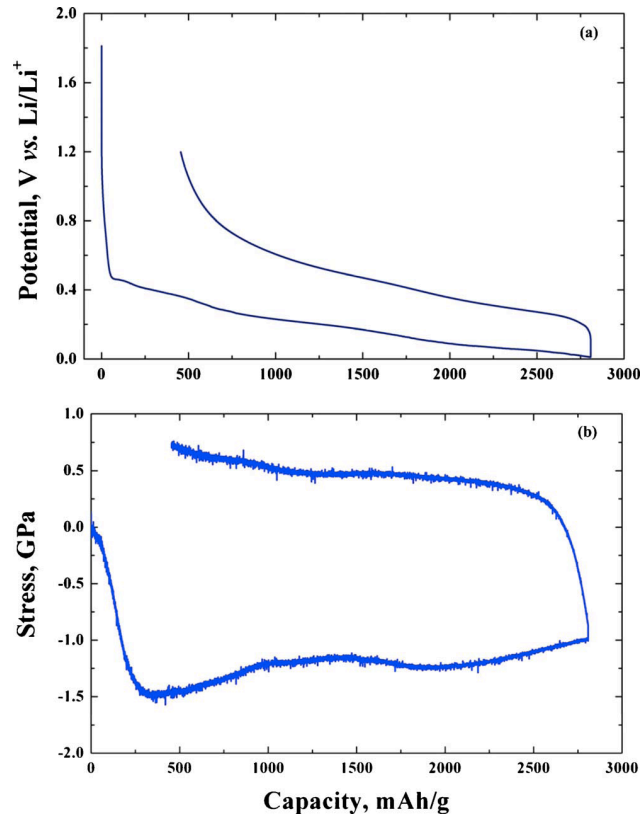


Figure 5.5: Discharge/charge curve (up), mechanical stress curve (down) on silicon thin-film. Notice the relaxation after the initial peak of stress. [41]

In the first experiment (section 4.3.2.2) a similar stress relaxation was observed, as the Fabry-Perot fringes notoriously expanded when reaching the 0.4V and after that the Fabry-Perot fringe diameters not only did not increase but also decreased in diameter. Since the Fabry-Perot fringe sizes are directly correlated with the mechanical stress on the thin-film silicon, a similar effect, i.e. stress relaxation, can be attributed to the experimental results observed. Fabry-Perot fringe images corresponding to the discharge cycle from figure 4.12 are shown in figure 5.6, illustrating the stress relaxation when in microphotograph 5 the voltage reached 0.245V and the Fabry-Perot fringe is smaller than on microphotograph 3 where the voltage is higher. This comparison of the obtained results

of this work and the ones in Sethuraman's paper [41], serve to show how the platform developed was able to capture fine nuances of the phenomenon observed, but explaining the origins of this mechanical stress relaxation exceeds the scope of this thesis. For a better understanding see the video of the first experiment using the link found in Appendix C.



Figure 5.6: Fabry-Perot fringe images from the discharge cycle of the first experiment.

White dotted lines inserted for better interpretation.

#### 5.3.4.-Mechanical stress accumulation from cycle to cycle.

The third experiment presented in section 4.3.2.4, was run for 22 discharge/charge cycles during a period of 11 days. During that period, a particular effect was observed: as cycles passed by, the Fabry-Perot fringe changes became more pronounced. At the beginning of the 0.1V to 1V cycling experiment barely any change could be appreciated in the Fabry-Perot fringes, but as seen on figure 4.13 on the 14<sup>th</sup> cycle electrochemically correlated Fabry-Perot fringe changes are observed, due to a more pronounced change in the Fabry-Perot fringe diameters. This effect was more evident when changing into the 0.01V to 1.5V test scheme, where in only 6 cycles the appearance of new Fabry-Perot fringe orders was observed, which means an increased stress in the silicon thin-film, and finally a membrane destruction. All this is clearly visible on the video of the third experiment (see Appendix C).

The closest explanation of this mechanical stress accumulation on the silicon thin-film that was observed during this experiment is found in [58] where the authors perform cycling experiments on silicon thin-films and forensic disassembling of the batteries, finding accumulative stress as the electrodes are cycled. In [64] a similar effect is described in silicon microparticles. The works cited above simply describe the occurrence but not the origin of the stress accumulation. Although not conclusive, the observed effect on the third experiment is very likely due to accumulative mechanical stress in the silicon thin-film.

#### **5.4.- Discussion**

The platform developed in this work consists of several components that have been designed, fabricated and assembled. The following paragraphs contain a discussion on each one of them. Afterwards there is brief discussion of the experimental results.

##### The MEMS chip

This monitoring platform relies on a MEMS chip as the transducing element that converts the battery active material volume change into an optical signal. The primary advantage of this MEMS chip is that it is very compact and has been fitted inside a modified coin cell. Through the development of this work, several configurations of thin-film materials have been tested, giving the idea that the MEMS chip can be applied with a very broad palette of materials, making it a very flexible Li-ion mechanical properties monitoring platform for various nanostructured lithium-ion battery electrodes, including thin films, nanocomposites and nanoparticles containing ink-casted electrodes. Although the micro fabrication process is simple in concept, some steps are very challenging and gave mixed results.

Specifically optimization on the DRIE process is needed to obtain smoother lateral wall surfaces, better membrane circular definition and to allow the posterior thin-film deposition to be more conformal (see figures 3.5, 3.6, 3.7, 4.10). The MEMS chip design can be modified to just include devices of a single diameter per wafer (either 150 $\mu\text{m}$ , 200 $\mu\text{m}$ , 250 $\mu\text{m}$  or 300 $\mu\text{m}$ ). Since DRIE etching rates are proportional to the aspect ratio of the etched feature [54], just using a single diameter device would eliminate the iterative DRIE process needed in step (j), which adds complexity to the device fabrication without adding much benefits.

Sputtering technique was used for the thin-film electrochemical stack deposition. This technique does not provide the most conformal coverage [50] but it was the only one available that provided all the needed materials. Experimental results also proved that the used technique was appropriate. But other techniques like ALD [49] provide better conformal coating and more precise control on the thickness of the film deposited. Using ALD would allow applying thinner thin films enabling different experiments using this platform. In order to do this specially tailored ALD processes are needed to apply the current collector and active material films.

#### The electrochemical package

After three design iterations, the package based on a custom-modified coin cell proved to be very effective. Coin cells are widely use in battery science, and their components are inexpensive and widely available. The equipment and trained personnel to assemble these cells is at disposal at the University of Maryland and many other institutions. The solution developed for this work gave excellent electrochemical results and Fabry-Perot fringe correlated results (see chapter 4). This package and the MEMS chip

present a clear advantage in practicality and cost when compared to other works as the ones presented in section 1.5.

#### The testing setup

The testing setup was assembled using mainly commercial components that were modified for this particular use. The Leica microscope used is a normal stereo microscope that was adapted for inverted use. The use of an inverted microscope would have been beneficial by having a more compact and lower gravity centered instrument, measurement would be less prone to be affected by vibrations coming from external sources in the laboratory. The de-speckled light source was custom built using a laser diode and a rotating disc. Although it was possible to obtain images with this light source, a more powerful and stable one would be desirable. Having more light power available would result in shorter exposure times on the microscope camera, again avoiding image artifacts coming from vibrations. Regarding the battery testing machine, the Arbin Instruments machine used fulfilled perfectly its purposes. Although complex, this setup is simpler than the one used by [41], and proved to be stable during test that lasted several days.

#### Experimental results

The results presented in chapter 4 and analyzed in chapter 5 were consistent enough to prove the feasibility of this platform and the use of MEMS technology for the purpose that was intended. Correlation between Fabry-Perot fringe changes and active material volume change / stress inside the Li-ion battery was demonstrated. All this lead to the conclusion that the platform developed can monitor volume change / stress on active materials in Li-ion batteries, but further development is needed to convert this into a measurement platform.

Particularly, during the development of this work several iterations of the package design ended in a very stable, repeatable and reliable electrochemical platform. The use of a custom-modified coin cell (third generation package) provided results that were extremely consistent and showing electrochemical signature of lithium insertion into silicon [36, 56, 58, 65] during the all the experiments. The importance of using 2032 coin cells lies in that they are the standard in lithium-ion battery research: not only they are inexpensive and reliable, but also most of the electrochemical scientific community is trained in using them. This provides a solid foundation on which the rest of the platform, and in particular the MEMS chip, can be refined to obtain quantitative measurement data.

Although very promising experimental results were obtained, further optimization on the MEMS chip is needed to enable a quantitative measuring platform, as proposed above in this section.

Finally this work introduces the capability of *in situ* direct measurement of mechanical expansion/contraction in a de-coupled way from the electrochemical process, integrating a MEMS transducing element into a custom-modified standard coin cell, leveraging established electrochemical experience with the innovative use of MEMS.

## **6.- Conclusions and future work.**

### **6.1.- Summary of results reported.**

This thesis presents the development of a platform for *in situ* monitoring of electrochemical reaction-induced stress in lithium-ion battery electrodes.

First a MEMS chip containing electrochemical micro-cavities and a sensing device based on a thin membrane and a Fabry-Perot interferometer was designed, fabricated and



tested. This MEMS chip is capable of receiving different active materials and current collectors in order to perform experiments. Using silicon as an active Li-ion battery material, a robust thin-film stack including a metal current collector and active silicon was developed. This thin-film stack proved to give very consistent results both on MEMS chips and on contrast experiments.

A complete measuring setup, including an optical microscope, camera, laser light source, image-capturing software and a battery-testing machine was assembled. This setup demonstrated to be flexible and reliable throughout many experiments performed.

Finally, the experiments performed show repeatable results when correlating the Fabry-Perot fringe change with the electrochemical data of the battery in a reversible fashion. The experimental results also show silicon thin-film behaviors than have been reported in the literature [41] [58].

## **6.2.- Future work.**

### **6.2.1.- Enhancement of the finesse of the Fabry-Perot interferometer.**

As seen in section 1.3, finesse is very important when resolving the position and size of the Fabry-Perot fringes. The computer-based analysis method proposed in section 5.2.1 would benefit from sharper images produced by enhanced finesse. The fabricated membranes proved to be very flat (see 3.3) and the Pyrex wafers used to complete the interferometer are optically flat ( $<1.5\text{nm RMS}$ ). Then, to enhance the finesse of the Fabry-Perot interferometer, a better reflectivity of the surfaces obtained by some surface treatment is needed. The logical path to increase the reflectivity would be to coat the Fabry-Perot interferometer surfaces with chrome or gold, in a layer of tens of nanometers [66]. The

coating itself would not be difficult to implement, but the fabrication process flow must be changed to accommodate such a coating.

### **6.2.2.- Testing of different active materials, anodes and cathodes.**

While silicon is a very attractive anode material for Li-ion batteries (see section 1.4.3), the platform presented in this work might be able to perform measurements on different anode and cathode materials. ALD deposited materials are a possibility, and vanadium oxide ( $V_2O_5$ ) is readily available and demonstrated as a good cathode material, as demonstrated by the work of Dr. E. Pomerantseva of MSAL [67]. Materials like titanium oxide, cobalt oxide, nickel oxide and others [68] that can be deposited via physical or chemical processes can be studied too. The architecture of the MEMS chip, with its electrochemical cavities, may lend itself to slurry formulations of materials that could also be tested using this platform [40]. While thin film electrodes at this point in time are practical for microbatteries, slurry-based electrodes are used for macro applications of lithium-ion batteries including portable electronics and automobile industry. This makes the platform developed in this work a versatile tool for studying various electrodes and battery chemistries.

### **6.2.3.- Designing a microscope-less testing setup.**

Microscale Fabry-Perot interferometers described in the literature [69, 70] use the intensity of the central fringe (fringe order 1) to do cavity length measurements. In the case of this work, the measurement of the Fabry-Perot fringe diameters was chosen as the parameter to be taken into account.

Modifying the MEMS chip design in order to accommodate a fiber optic coupling centered with the Fabry-Perot interferometer, would provide the capability of measuring the

cavity length without using a microscope, but using a laser, fiber optic and an intensity meter setup as seen in [69].

#### **6.2.4.- Measurement of volume change / stress on active materials in Li-ion batteries.**

Using the elements designed, tested and fabricated in this work, and applying refinements like the automated computer analysis of fringe images and increasing finesse in the Fabry-Perot interferometer, it may be possible to extend the capabilities of this platform from monitoring to measuring the volume change / stress on active materials in Li-ion batteries; and to obtain quantitative data of the measurements. A natural extension to this work is following the path from the achieved results of validating the feasibility of this platform, to turn it into a measurement instrument.

#### **6.3.- Conclusion.**

This work has demonstrated the design, fabrication and testing of a platform towards *in situ* stress/strain measurement in lithium ion battery electrodes. This platform is capable of monitoring the mechanical stress in the active materials in a de-coupled measurement from the electrochemical process.

The innovative use of a MEMS chip permits the core components to fit inside the size of a 2032 coin cell, allowing the assembly and testing of the experiments just using standard battery components and testing tools. Iterative work done on the experimental package design and thin-film electrochemical stack resulted into a combination of knowledge that enabled a very stable battery configuration for experimentation. Experiments using silicon as an active anode material were repeatedly performed on dummy chips and on the complete MEMS chip platform obtaining correlated

electrochemical and Fabry-Perot fringe results that validate the concept proposed at the beginning of this work.

Finally, some first steps towards the analysis of the obtained experimental results and measuring method were done, enabling the future evolution of this monitoring platform into a complete measurement platform capable of precisely obtaining values of the mechanical stress of an electrode material of a Li-ion battery while in operation.

## Appendix A: Photolithography masks.

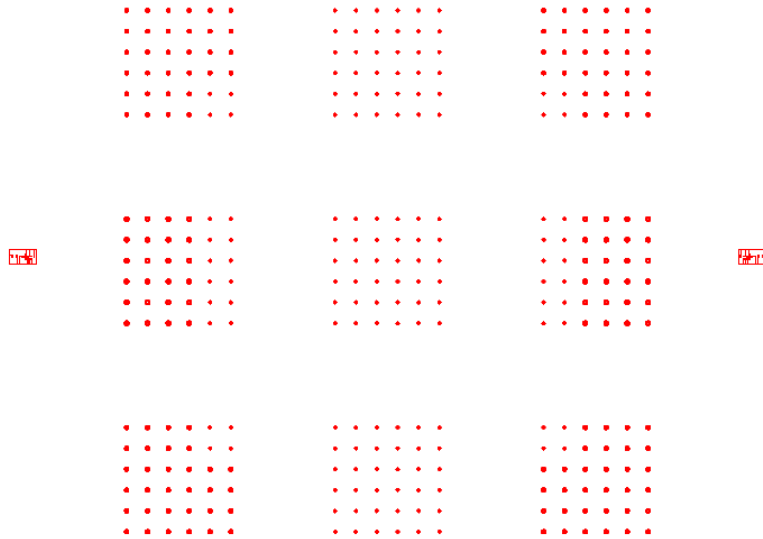


Image of second mask

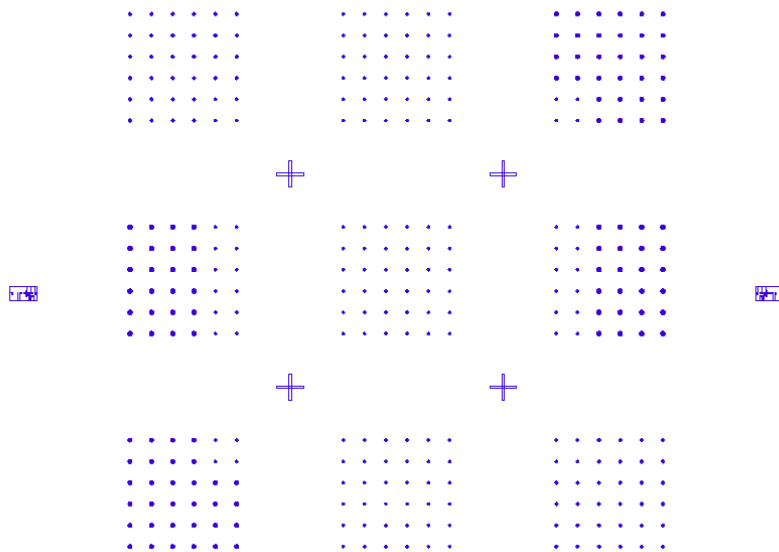


Image of third mask

## Appendix B: Fabrication process details.

Deep Reaction Ion Etching (DRIE) Bob3dss recipe details.

Step	Time	C <sub>4</sub> F <sub>8</sub>	SF <sub>6</sub>	O <sub>2</sub>	Ar	Pressure	RF power
Etch	11s	0 sccm	130 sccm	13 sccm	0 sccm	25mTorr	600w
Passivate	8s	85 sccm	0 sccm	0 sccm	0 sccm	25mTorr	600w

Reactive Ion Etching (RIE) SergioSiN recipe details.

CHF <sub>3</sub>	SF <sub>6</sub>	RF	ICP	Pressure
90 sccm	10 sccm	50w	2000w	10mTorr

Anodic Bonding recipe details.

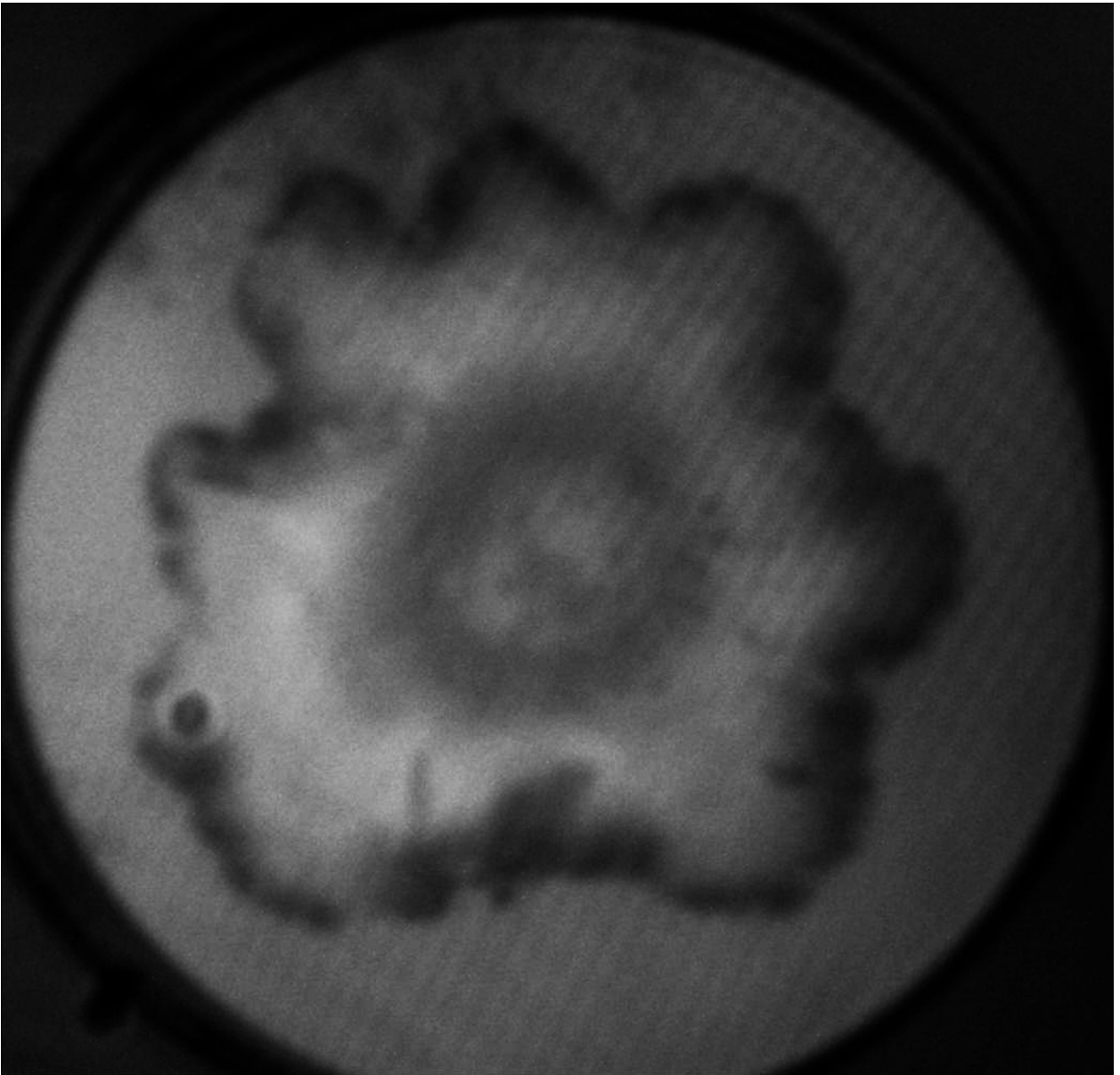
Chuck Temp. (up)	Chuck Temp. (down)	Pressure	Voltage	Time
350°C	350°C	1mTorr	-1000v	5min

## Appendix C: Experiment videos.

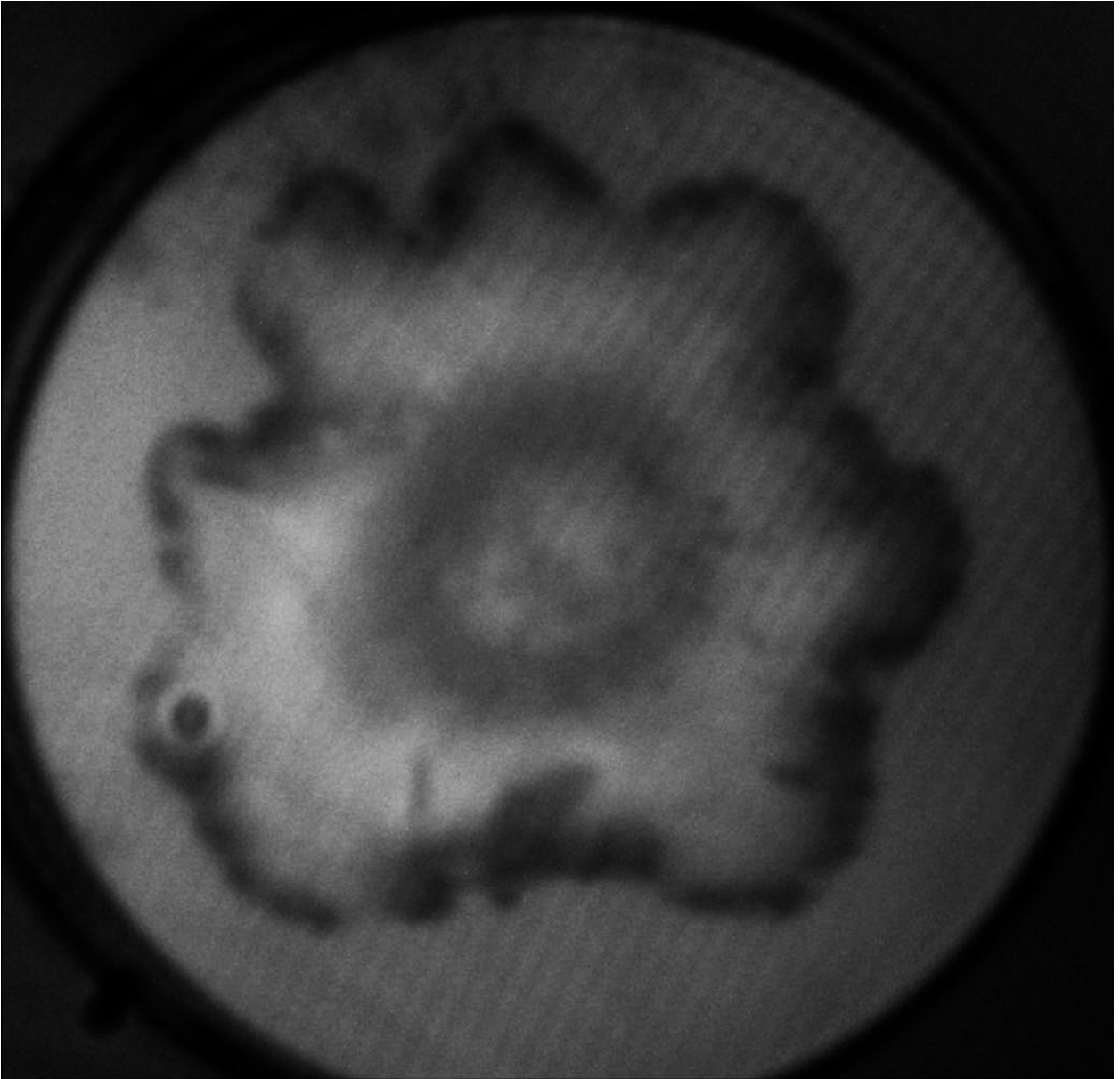
- Video for the first experiment can be found at: [http://youtu.be/u\\_vuW3uJ2ZE](http://youtu.be/u_vuW3uJ2ZE)
- Video for the second experiment can be found at: [http://youtu.be/ylikO4Mzz\\_M](http://youtu.be/ylikO4Mzz_M)
- Video for the third experiment can be found at: <http://youtu.be/18oOpZFWJSM>

## Appendix D: FP fringe images.

Images of FP fringes corresponding to the first experiment. Image numbers match the numbers on figure 4.11.

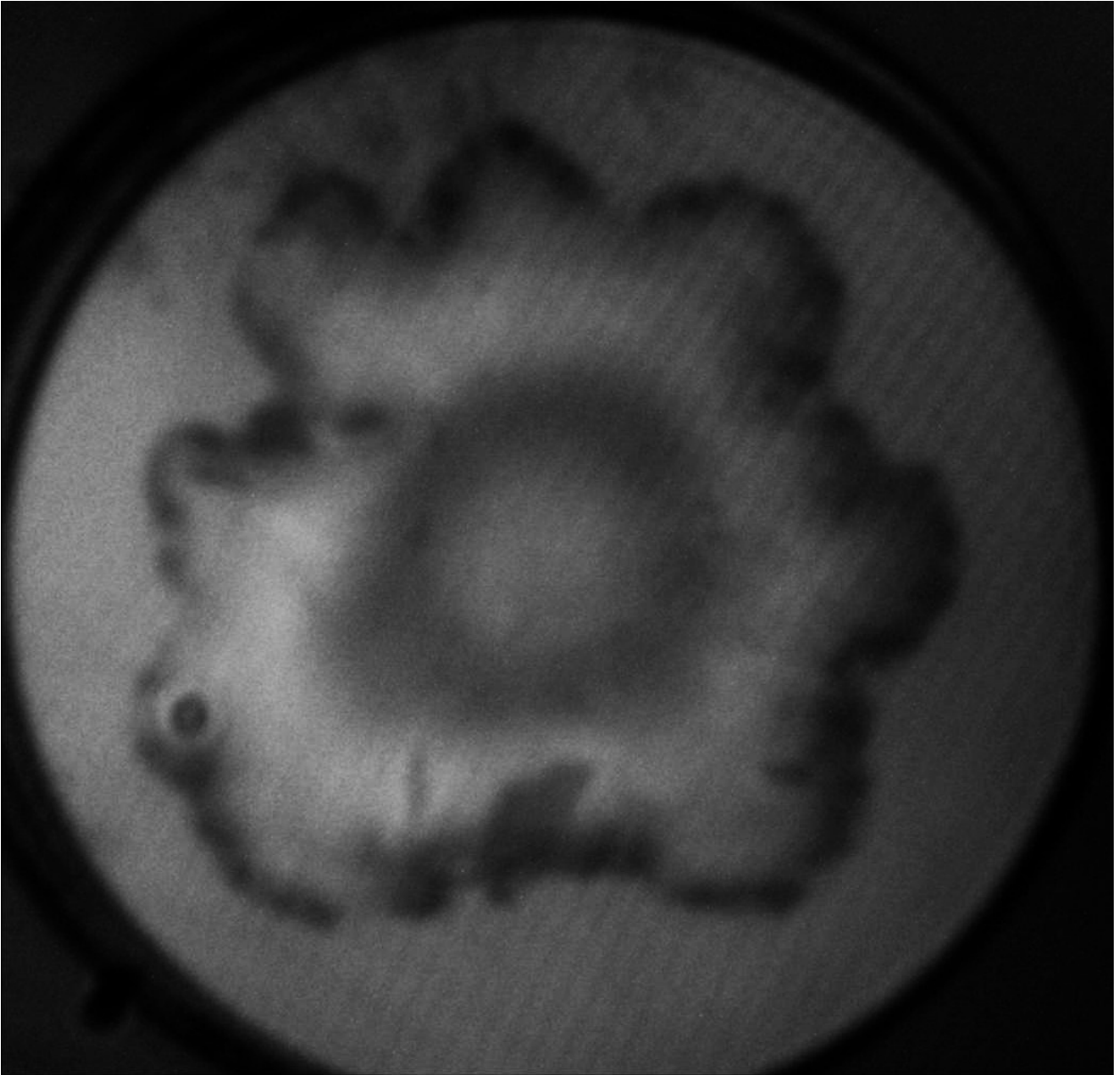


FP fringe image 1

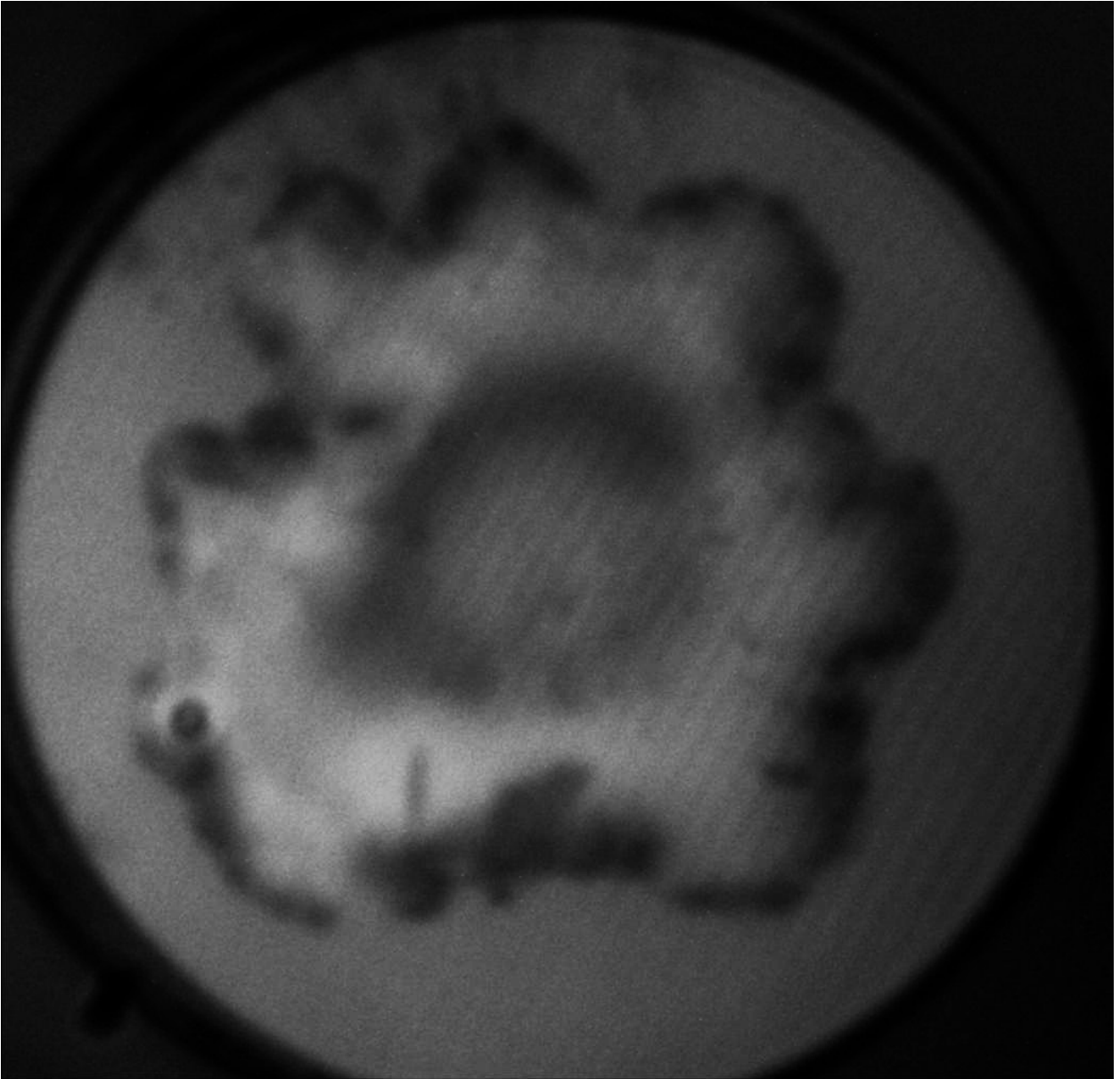


FP fringe image 2

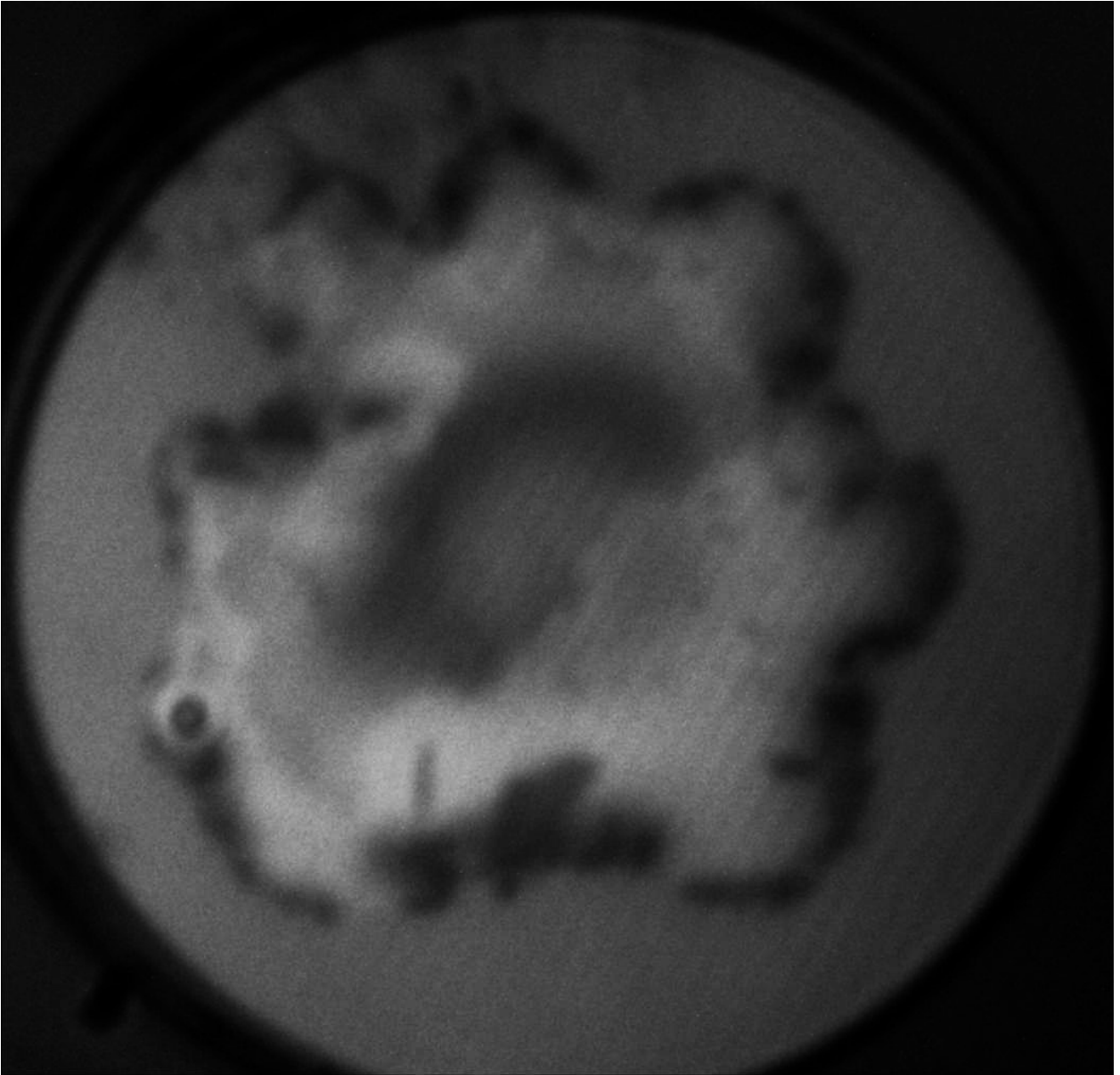




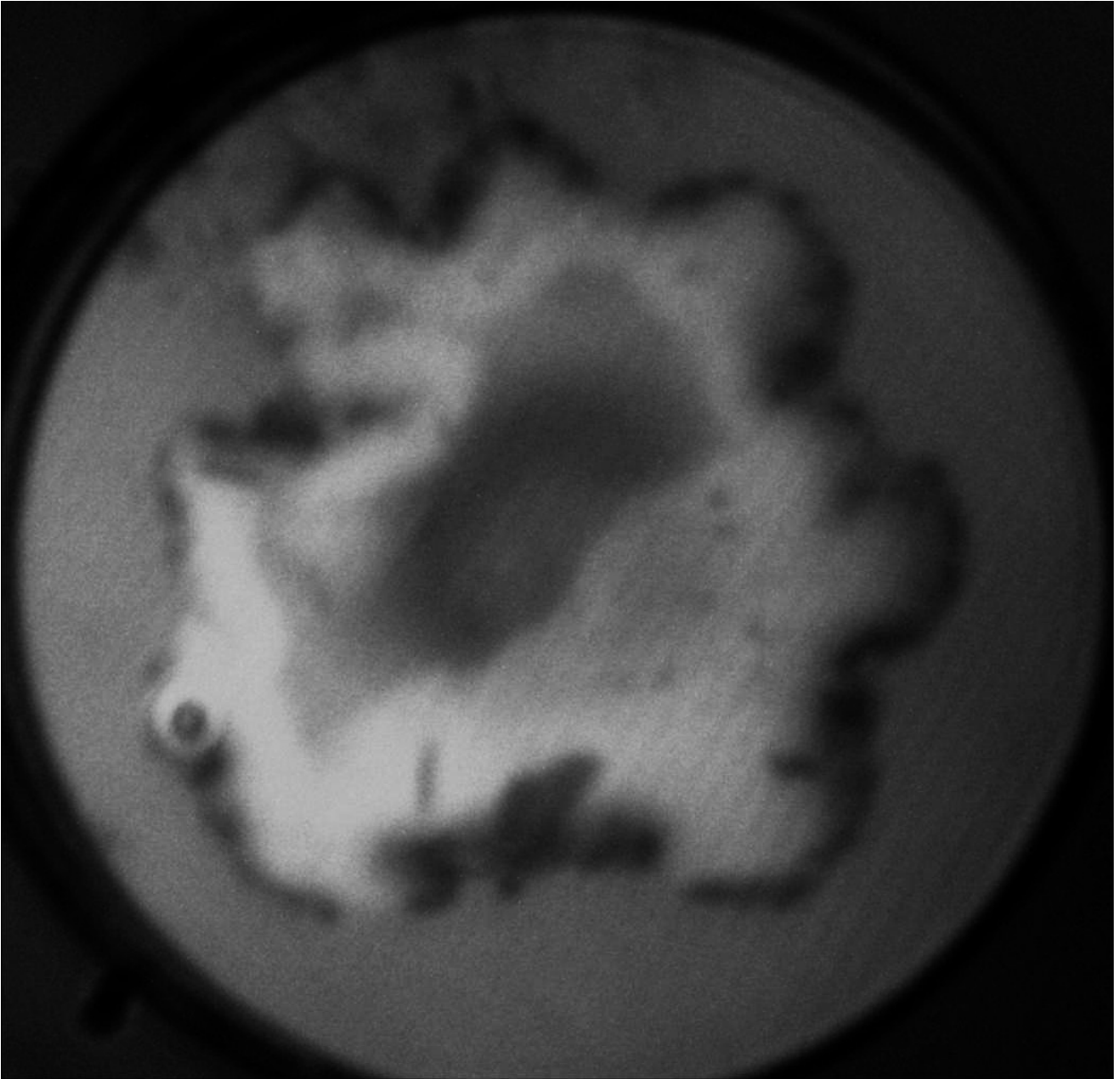
FP fringe image 3



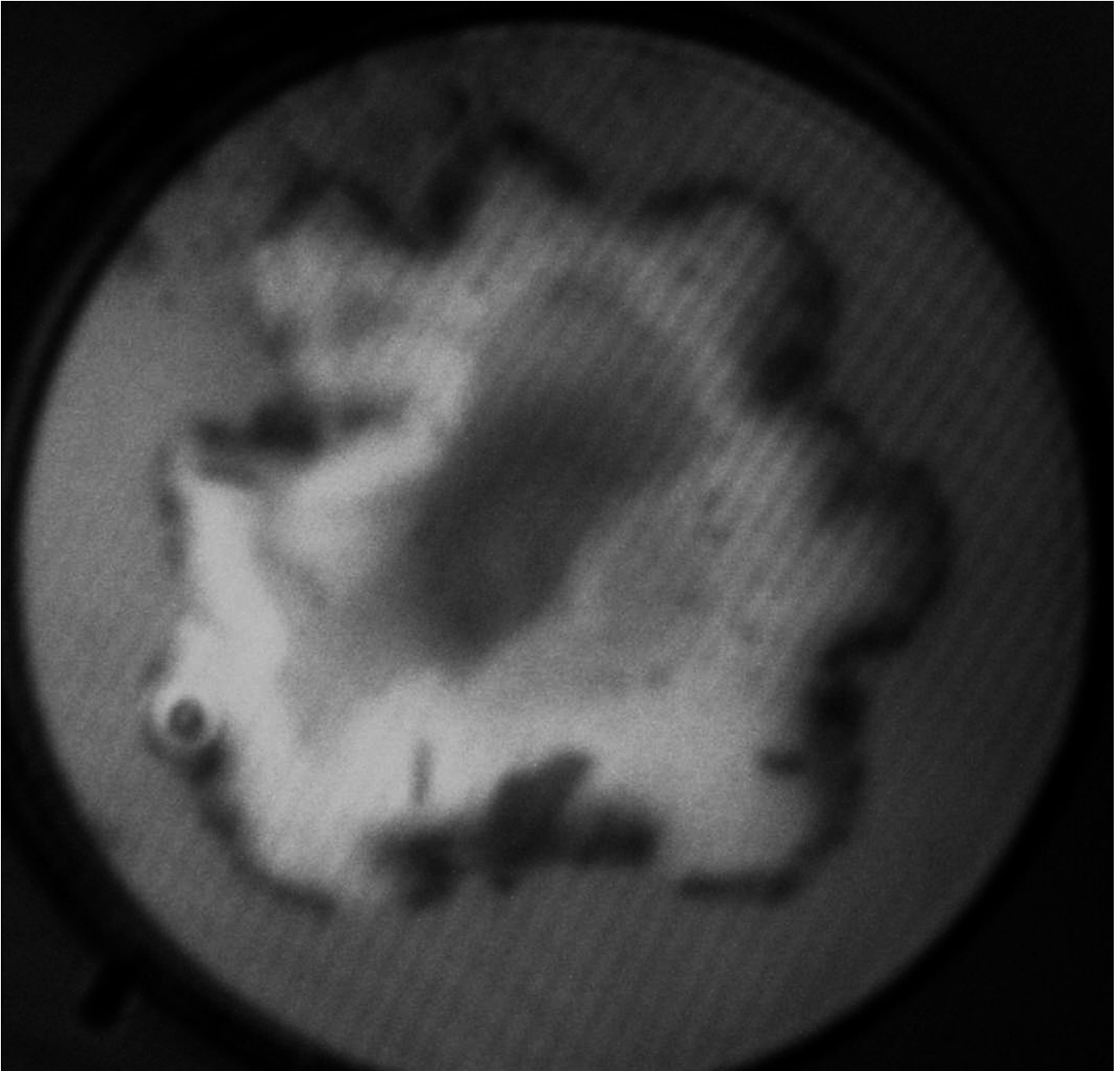
FP fringe image 4



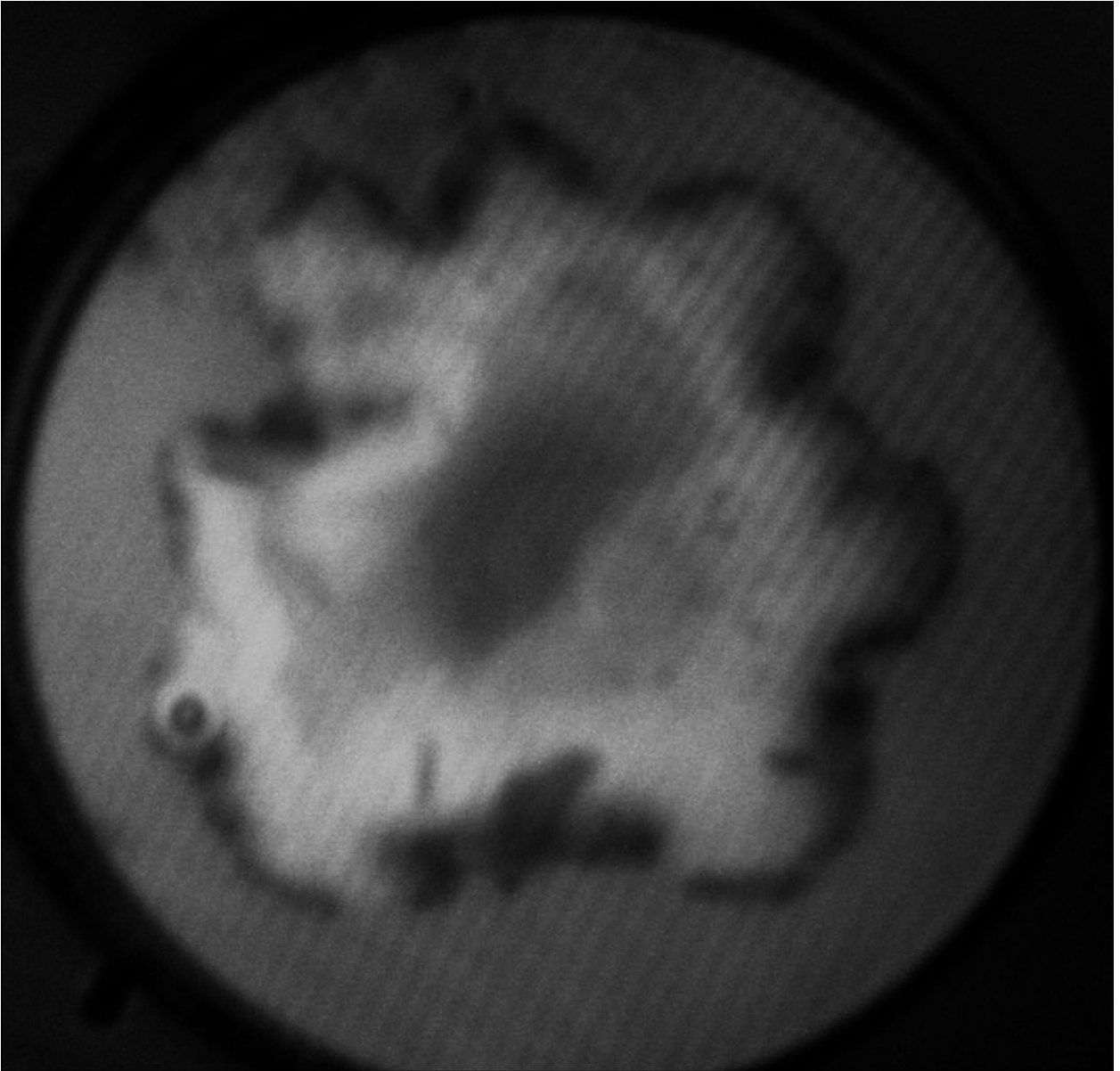
FP fringe image 5



FP fringe image 6



FP fringe image 7



FP fringe image 8

## Appendix E: Image analysis MatLab code.

### Matlab code for plotting graphs (M. Gnerlich).

```
function [ output_args ] = fpbtest2_figure( imagel, image2, cx, cy, roi_top,
roi_bot, trace )

%FPBTEST2_FIGURE make the (original, unwrapped, 1-D trace) figure

cart_width = size(imagel,2);
cart_height = size(imagel,1);
cut_x = [ceil(cart_width/2):cart_width];
cut_y = ones(size(cut_x)).*ceil(cart_height/2);

pol_width = size(image2,2);
roi_x = [1:pol_width];
roi_yt = ones(size(roi_x)).*roi_top;
roi_yb = ones(size(roi_x)).*roi_bot;
figure(); hold on;
subplot(1,3,1); hold on; imshow(imagel); plot(cx,cy,'bo'); plot(cut_x,cut_y,'b-');
title('cartesian'); xlabel('horizontal'); ylabel('vertical');
subplot(1,3,2); hold on; imshow(image2); plot(roi_x,roi_yt,'r'); plot(roi_x,roi_yb,'r');
title('polar'); xlabel('radius'); ylabel('circumference');
subplot(1,3,3); hold on; plot(trace); title('polar average'); xlabel('radius (px)');
ylabel('intensity (8-bit)');
hold off;

end
```

### Main Matlab code (M. Gnerlich).

```
% polar center of image
cx = 217;
cy = 214;
```

```

% region of interest to include in trace...

% narrow fringes towards the top (in polar)
roi_top = 150;
roi_bot = 400;

% narrow fringes towards the bottom (in polar)
% roi_top = 850;
% roi_bot = 1050;

% wide fringes towards the bottom (in polar)
% roi_top = 1150;
% roi_bot = 1250;

% read the images into memory and equalize grayscale histogram
for image_index = 1:8
    % path to the image
    path{image_index} = sprintf('./fpbtest2/150afptestdata-%d.jpg',image_index);
    label{image_index} = sprintf('No. %d',image_index);

%   gray = imread(path{image_index});
    gray{image_index}    = rgb2gray(imread(path{image_index}));
    gray_eq{image_index} = histeq(gray{image_index});

    % use cart2pol to make a polar version of the cartesian image data
    % (but cart2pol requires double array instead of uint8 so convert)
    gray_eq_pol{image_index} =
uint8(cart2pol(double(gray_eq{image_index})./255,cx,cy).*255);
    gray_eq_pol_roi{image_index} = gray_eq_pol{image_index}(roi_top:roi_bot,:);

    % make a 1-dimensional trace of intensity from the polar image data
    trace{image_index} = mean(gray_eq_pol_roi{image_index},1);

```



```

end

% show the original image, polar image, trace
fpbtest2_figure(gray_eq{1},gray_eq_pol{1}, cx, cy, roi_top, roi_bot, trace{1});

% make a plot of first 4
figure(); hold on;
plot(trace{1},'k-');
plot(trace{2},'r-');
plot(trace{3},'g-');
plot(trace{4},'b-');
legend(label{1:4});
title('polar average'); xlabel('radius (px)'); ylabel('intensity'); grid on;
hold off;

% make a plot of second 4
figure(); hold on;
plot(trace{5},'k-');
plot(trace{6},'r-');
plot(trace{7},'g-');
plot(trace{8},'b-');
legend(label{5:8});
title('polar average'); xlabel('radius (px)'); ylabel('intensity'); grid on;
hold off;

```

### MatLab code for Cartesian to polar conversion.

```

function array_pol = cart2pol (array_cart, center_x, center_y, radius_nmin,
radius_nmax, polar_radius, polar_circumference)

% CART2POL converts an array of double from cartesian to polar layout
%
% array_cart          image as 2D array of double
% center_x           center of image (horizontal)

```

```

% center_y          center of image (vertical)
% radius_nmin       normalized radius to include (0 ... 1)
% radius_nmax       normalized radius to include (0 ... 1)
% polar_radius      output radius
% polar_circumference output circumference

% get size of rectangular image
[array_cart_size1 array_cart_size2] = size(array_cart);

% default parameters
if nargin<2, center_x = (array_cart_size1+1)/2; end
if nargin<3, center_y = (array_cart_size2+1)/2; end
if nargin<4, radius_nmin=0; end
if nargin<5, radius_nmax=1; end
if nargin<6, polar_radius = floor(min(array_cart_size1,array_cart_size2)/2); end
if nargin<7, polar_circumference = floor(2*pi*polar_radius); end

% validate input
radius_nmin = min(max(radius_nmin,0),1);
radius_nmax = min(max(radius_nmax,0),1);
center_x = floor(center_x);
center_y = floor(center_y);

% scale factors
sx = (array_cart_size1-1)/2;
sy = (array_cart_size2-1)/2;

% set everything up
dr = (radius_nmax - radius_nmin)/(polar_radius-1);
dth = 2*pi/(polar_circumference-1);

r = radius_nmin:dr:radius_nmax;
th = (0:dth:2*pi)';

```

```

% make the polar version

[r_mesh,th_mesh] = meshgrid(r,th);

x_pol = (r_mesh.*cos(th_mesh)).*sx + center_x;
y_pol = (r_mesh.*sin(th_mesh)).*sy + center_y;

% make a rectangular array from the polar grid
array_pol = interp2(array_cart, x_pol, y_pol);

```

## Bibliography

1. McDowall, J. *Conventional battery technologies-present and future*. in *Power Engineering Society Summer Meeting, 2000. IEEE*. 2000.
2. Broussely, M., P. Biensan, and B. Simon, *Lithium insertion into host materials: the key to success for Li ion batteries*. *Electrochimica Acta*, 1999. **45**(1–2): p. 3-22.
3. Armand, M. and J.M. Tarascon, *Building better batteries*. *Nature*, 2008. **451**(7179): p. 652-657.
4. Rhodes, K., et al., *Understanding the Degradation of Silicon Electrodes for Lithium-Ion Batteries Using Acoustic Emission*. *Journal of the Electrochemical Society*, 2010. **157**(12): p. A1354.
5. Iwakura, C., et al., *Electrochemical characterization of various metal foils as a current collector of positive electrode for rechargeable lithium batteries*. *Journal of Power Sources*, 1997. **68**(2): p. 301-303.
6. Wakihara, M., *Recent developments in lithium ion batteries*. *Materials Science and Engineering: R: Reports*, 2001. **33**(4): p. 109-134.

7. Aurbach, D., et al., *A short review of failure mechanisms of lithium metal and lithiated graphite anodes in liquid electrolyte solutions*. Solid State Ionics, 2002. **148**(3–4): p. 405-416.
8. Judy, J.W., *Microelectromechanical systems (MEMS): fabrication, design and applications*. Smart materials and Structures, 2001. **10**: p. 1115.
9. Bogue, R., *MEMS sensors: past, present and future*. Sensor Review, 2007. **27**(1): p. 7-13.
10. Senturia, S.D., *Microsystem design* 2001, Boston: Kluwer Academic Publishers. xxvi, 689 p.
11. Bell, D., et al., *MEMS actuators and sensors: observations on their performance and selection for purpose*. Journal of Micromechanics and Microengineering, 2005. **15**: p. S153.
12. Lu, W. and C.M. Lieber, *Nanoelectronics from the bottom up*. Nature materials, 2007. **6**(11): p. 841-850.
13. Whitesides, G.M., J.P. Mathias, and C.T. Seto, *Molecular self-assembly and nanochemistry: a chemical strategy for the synthesis of nanostructures*. Science, 1991. **254**(5036): p. 1312-1319.
14. Sneh, O., et al., *Thin film atomic layer deposition equipment for semiconductor processing*. Thin Solid Films, 2002. **402**(1): p. 248-261.
15. Neukermans, A. and R. Ramaswami, *MEMS technology for optical networking applications*. Communications Magazine, IEEE, 2001. **39**(1): p. 62-69.
16. Kim, S.G., G. Barbastathis, and H. Tuller, *MEMS for Optical Functionality Electroceramic-Based MEMS*. 2005. **9**: p. 157-174.
17. Fujita, H. and H. Toshiyoshi, *Optical MEMS*. Ieice Transactions on Electronics, 2000. **E83c**(9): p. 1427-1434.
18. Wu, M.C., et al. *Optical MEMS: Huge possibilities for Lilliputian-sized devices*. 1998. Optical Society of America.

19. Ollier, E., *Optical MEMS devices based on moving waveguides*. Selected Topics in Quantum Electronics, IEEE Journal of, 2002. **8**(1): p. 155-162.
20. Bishop, D.J., C.R. Giles, and G.P. Austin, *The Lucent LambdaRouter: MEMS technology of the future here today*. Communications Magazine, IEEE, 2002. **40**(3): p. 75-79.
21. Hornbeck, L.J. *Digital Light Processing and MEMS: an overview*. in *Advanced Applications of Lasers in Materials Processing/Broadband Optical Networks/Smart Pixels/Optical MEMs and Their Applications. IEEE/LEOS 1996 Summer Topical Meetings*:. 1996.
22. Hornbeck, L.J. *Current status of the digital micromirror device (DMD) for projection television applications*. 1993. IEEE.
23. Chen, R.T., H. Nguyen, and M.C. Wu, *A high-speed low-voltage stress-induced micromachined 2 x 2 optical switch*. Ieee Photonics Technology Letters, 1999. **11**(11): p. 1396-1398.
24. T. Thundat, P.I.O. and R.J. Warmack, *MICROCANTILEVER SENSORS*. Microscale Thermophysical Engineering, 1997. **1**(3): p. 185-199.
25. Hansen, K.M., et al., *Cantilever-based optical deflection assay for discrimination of DNA single-nucleotide mismatches*. Analytical Chemistry, 2001. **73**(7): p. 1567-1571.
26. Noro, M., et al. *CO<sub>2</sub>/H<sub>2</sub>O gas sensor using a tunable Fabry-Perot filter with wide wavelength range*. 2003. IEEE.
27. Pattnaik, P.K., et al. *Optical MEMS pressure sensor using ring resonator on a circular diaphragm*. 2005. IEEE.
28. Miller, M.F., *Fabry-Perot Pressure Sensor Arrays for Imaging Surface Pressure Distributions*. Transducers, 1997.
29. Harasaki, A. and J.C. Wyant, *Fringe modulation skewing effect in white-light vertical scanning interferometry*. Applied Optics, 2000. **39**(13): p. 2101-2106.

30. Deck, L. and P. de Groot, *High-speed noncontact profiler based on scanning white-light interferometry*. Applied Optics, 1994. **33**(31): p. 7334-7338.
31. In Wikipedia, T.F.E. *Fabry–Pérot interferometer*. (2012, May 15); Available from: [http://en.wikipedia.org/w/index.php?title=Fabry%E2%80%93P%C3%A9rot\\_interferometer&oldid=492712998](http://en.wikipedia.org/w/index.php?title=Fabry%E2%80%93P%C3%A9rot_interferometer&oldid=492712998).
32. Schalkwijk, W. and B. Scrosati, *Advances in Lithium Ion Batteries Introduction Advances in Lithium-Ion Batteries*. 2002: p. 1-5.
33. Valoen, L.O. and J.N. Reimers, *Transport properties of LiPF<sub>6</sub>-based Li-ion battery electrolytes*. Journal of the Electrochemical Society, 2005. **152**(5): p. A882-A891.
34. Tarascon, J. and M. Armand, *Issues and challenges facing rechargeable lithium batteries*. 2001.
35. Li, J., et al., *Crack Pattern Formation in Thin Film Lithium-Ion Battery Electrodes*. Journal of the Electrochemical Society, 2011. **158**: p. A689.
36. Bourderau, S., T. Brousse, and D.M. Schleich, *Amorphous silicon as a possible anode material for Li-ion batteries*. Journal of Power Sources, 1999. **81–82**(0): p. 233-236.
37. Kasavajjula, U., C. Wang, and A.J. Appleby, *Nano- and bulk-silicon-based insertion anodes for lithium-ion secondary cells*. Journal of Power Sources, 2007. **163**(2): p. 1003-1039.
38. Golmon, S., et al., *Stress generation in silicon particles during lithium insertion*. Applied Physics Letters, 2010. **97**(3): p. 033111.
39. Obrovac, M.N. and L. Christensen, *Structural Changes in Silicon Anodes during Lithium Insertion/Extraction*. Electrochemical and Solid-State Letters, 2004. **7**(5): p. A93.
40. Kim, K.M., et al., *Effect of mixing sequences on the electrode characteristics of lithium-ion rechargeable batteries*. Journal of Power Sources, 1999. **83**(1–2): p. 108-113.

41. Sethuraman, V.A., et al., *In Situ Measurements of Stress-Potential Coupling in Lithiated Silicon*. Journal of the Electrochemical Society, 2010. **157**(11): p. A1253-A1261.
42. Koev, S.T. and S. Koev, *Design, Fabrication, and Testing of a Microsystem for Monitoring Bacterial Quorum Sensing*, 2009, University of Maryland.
43. Heavens, O.S., *The Fabry-Perot-Interferometer - History, Theory, Practice and Applications - Vaughan, Jm*. Nature, 1989. **341**(6239): p. 194-194.
44. Balakrishnan, P.G., R. Ramesh, and T. Prem Kumar, *Safety mechanisms in lithium-ion batteries*. Journal of Power Sources, 2006. **155**(2): p. 401-414.
45. Hong, S., et al., *Measuring stiffnesses and residual stresses of silicon nitride thin films*. Journal of Electronic Materials, 1990. **19**(9): p. 903-909.
46. Moshtev, R. and B. Johnson, *State of the art of commercial Li ion batteries*. Journal of Power Sources, 2000. **91**(2): p. 86-91.
47. In Wikipedia, T.F.E. *Button cell*. (2012, May 20); Available from: [http://en.wikipedia.org/w/index.php?title=Button\\_cell&oldid=493517462](http://en.wikipedia.org/w/index.php?title=Button_cell&oldid=493517462).
48. Gabor, D., *Laser speckle and its elimination*. IBM Journal of Research and Development, 1970. **14**(5): p. 509-514.
49. Leskelä, M. and M. Ritala, *Atomic layer deposition (ALD): from precursors to thin film structures*. Thin Solid Films, 2002. **409**(1): p. 138-146.
50. Vossen, J., *Control of film properties by rf-sputtering techniques*. Journal of Vacuum Science and Technology, 1971. **8**(5): p. S12-S30.
51. Reddy, A.S., S. Uthanna, and P.S. Reddy, *Properties of dc magnetron sputtered Cu<sub>2</sub>O films prepared at different sputtering pressures*. Applied surface science, 2007. **253**(12): p. 5287-5292.
52. Johnson, B.A. and R.E. White, *Characterization of commercially available lithium-ion batteries*. Journal of Power Sources, 1998. **70**(1): p. 48-54.

53. Xiang, Y., et al. *The effects of passivation layer and film thickness on the mechanical behavior of freestanding electroplated Cu thin films with constant microstructure*. 2003. Cambridge Univ Press.
54. Yeom, J., Y. Wu, and M.A. Shannon. *Critical aspect ratio dependence in deep reactive ion etching of silicon*. 2003. IEEE.
55. Geoffroy, I., et al., *Electrolytic characteristics of ethylene carbonate-diglyme-based electrolytes for lithium batteries*. *Electrochimica Acta*, 2000. **45**(13): p. 2019-2027.
56. Kulova, T.L., et al., *Lithium insertion into amorphous silicon thin-film electrodes*. *Journal of Electroanalytical Chemistry*, 2007. **600**(1): p. 217-225.
57. Sawyer, D.T. and J.L.J.R. Roberts, *Electrochemistry for chemists second edition*. JOHN WILEY SONS INC, 1994.
58. Maranchi, J.P., A.F. Hepp, and P.N. Kumta, *High Capacity, Reversible Silicon Thin-Film Anodes for Lithium-Ion Batteries*. *Electrochemical and Solid-State Letters*, 2003. **6**(9): p. A198.
59. Kong, F., et al., *In situ studies of SEI formation*. *Journal of Power Sources*, 2001. **97**: p. 58-66.
60. Kasavajjula, U., C. Wang, and A.J. Appleby, *Nano-and bulk-silicon-based insertion anodes for lithium-ion secondary cells*. *Journal of Power Sources*, 2007. **163**(2): p. 1003-1039.
61. Lee, Y.M., et al., *SEI Layer Formation on Amorphous Si Thin Electrode during Precycling*. *Journal of the Electrochemical Society*, 2007. **154**(6): p. A515.
62. Kumai, K., et al., *Gas generation mechanism due to electrolyte decomposition in commercial lithium-ion cell*. *Journal of Power Sources*, 1999. **81–82**(0): p. 715-719.
63. O’Hora, M., B. Bowe, and V. Toal, *Least squares algorithm for rapid analysis of Fabry–Perot fringe patterns*. *Journal of Optics A: Pure and Applied Optics*, 2005. **7**(6): p. S364-S367.



64. Kalnaus, S., K. Rhodes, and C. Daniel, *A study of lithium ion intercalation induced fracture of silicon particles used as anode material in Li-ion battery*. Journal of Power Sources, 2011.
65. Chen, X.L., et al., *High rate performance of virus enabled 3D n-type Si anodes for lithium-ion batteries*. Electrochimica Acta, 2011. **56**(14): p. 5210-5213.
66. Agarwal, R., et al., *Fabrication of integrated vertical mirror surfaces and transparent window for packaging MEMS devices*. Microelectromechanical Systems, Journal of, 2007. **16**(1): p. 122-129.
67. Pomerantseva, E., et al., *Electrochemical performance of the nanostructured biotemplated V2 O5 cathode for lithium-ion batteries*. Journal of Power Sources, 2012.
68. Aricò, A.S., et al., *Nanostructured materials for advanced energy conversion and storage devices*. Nature materials, 2005. **4**(5): p. 366-377.
69. Li, M., M. Wang, and H. Li, *Optical MEMS pressure sensor based on Fabry-Perot interferometry*. Optics Express, 2006. **14**(4): p. 1497-1504.
70. Gander, M.J., et al., *Embedded micromachined fiber-optic Fabry-Perot pressure sensors in aerodynamics applications*. Sensors Journal, IEEE, 2003. **3**(1): p. 102-107.